REPORT DOCUMENTATION PAGE

Form Approved
OMB NO. 0704-0188

Public Reporting burden for this collection of information is estimated to average 1 hour per response, including the time for reviewing instructions, searching existing data sources, gathering and maintaining the data needed, and completing and reviewing the collection of information. Send comment regarding this burden estimates or any other aspect of this collection of information, including suggestions for reducing this burden, to Washington Headquarters Services, Directorate for information Operations and Reports, 1215 Jefferson Davis Highway, Suite 1204, Arlington, VA 22202-4302, and to the Office of Management and Budget, Paperwork Reduction Project (0704-0188,) Washington, DC 20503.

1. AGENCY USE ONLY (Leave Blank)	2. REPORT DATE	3. REPORT TYPE AND DATES COVERED
	August 31, 2004	Final Technical: 9/1/98 - 5/31/04

4. TITLE AND SUBTITLE
Model and Subcomponent Development for a Pulse Combustor Driven Microgenerator

5. FUNDING NUMBERS
Contract DAAG55-98-1-0284

6. AUTHOR(S)
Ben T. Zinn, Ari Glezer, and Mark G. Allen

7. PERFORMING ORGANIZATION NAME(S) AND ADDRESS(ES)
Georgia Institute of Technology
Atlanta, GA 30332

8. PERFORMING ORGANIZATION REPORT NUMBER
E-25-Y77

9. SPONSORING / MONITORING AGENCY NAME(S) AND ADDRESS(ES)
U. S. Army Research Office
P.O. Box 12211
Research Triangle Park, NC 27709-2211

10. SPONSORING / MONITORING AGENCY REPORT NUMBER
38564.1-EG-MUR

11. SUPPLEMENTARY NOTES
The views, opinions and/or findings contained in this report are those of the author(s) and should not be construed as an official Department of the Army position, policy or decision, unless so designated by other documentation.

12 a. DISTRIBUTION / AVAILABILITY STATEMENT
Approved for public release; distribution unlimited.

12 b. DISTRIBUTION CODE

13. ABSTRACT (Maximum 200 words)

The project focused on an investigation of the feasibility of pulse-combustion-based micro heat engines for electrical power generation. The micro heat engines to be studied are based on a reciprocating free piston that is driven by a periodic pulse combustion process, resulting in high levels of integration of the mechanical and electrical functionality of the engine (i.e., the same piston performs both the fuel-to-mechanical energy conversion as well as the mechanical-to-electrical energy conversion). Other than the reciprocating piston, the only other moving parts in the engine are optional fuel control and passive flapper mixing valves.

For the first three years of the program, the major emphasis was on performing modeling, and numerical simulations of the pulse combustors and free piston generator and the development of magnetic generator topology. The issues that are addressed include small-scale pulse combustion phenomena and modeling of combustion in high surface-to-volume ratio environments; design of ultracompact permanent-magnet-based and non-permanent-magnet-based, variable reluctance generators; and selection of appropriate materials and fabrication sequences for the realization of the various subcomponents of the generator using micromachining technology as appropriate. In the final two years of the program the emphasis switched to fabrication and testing of critical subcomponents, in order to assess the advantages and limitations of the application of micromachining technology to the fabrication of microgenerator subcomponents.

14. SUBJECT TERMS	15. NUMBER OF PAGES
Microgenerator, Pulse Combustor, Reciprocating, Piston	75
	16. PRICE CODE

17. SECURITY CLASSIFICATION OR REPORT	18. SECURITY CLASSIFICATION ON THIS PAGE	19. SECURITY CLASSIFICATION OF ABSTRACT	20. LIMITATION OF ABSTRACT
UNCLASSIFIED	UNCLASSIFIED	UNCLASSIFIED	UL

MODEL AND SUBCOMPONENT DEVELOPMENT FOR A PULSE-COMBUSTION-DRIVEN MICROGENERATOR

Principal Investigators

Professors Ben T. Zinn, Ari Glezer, and Mark G. Allen

Georgia Institute of Technology, Atlanta, GA

PROJECT OVERVIEW

The project focused on an investigation of the feasibility of pulse-combustion-based micro heat engines for electrical power generation. The micro heat engines studied were based on a reciprocating free piston that is driven by a periodic pulse combustion process, resulting in high levels of integration of the mechanical and electrical functionality of the engine (i.e., the same piston performs both the fuel-to-mechanical energy conversion as well as the mechanical-to-electrical energy conversion). Other than the reciprocating piston, the only other moving parts in the engine are optional fuel control and passive flapper mixing valves.

The basic idea of the engine is very simple. A prismatic piston is free to move in a complementary surrounding channel. The piston is placed between two pulse combustors, with means for introducing fuel and air and igniting combustible mixtures. When the piston is at one extreme of its motion, the combustible mixture inside the smaller volume combustor is ignited, and the ensuing combustion process and increase of pressure propel the piston towards the other end of the chamber. Just as the piston reaches the other end of the chamber, the combustible mixture that has formed during the piston's motion in the opposite combustor is ignited, sending the piston back. By appropriate timing of the combustion, the piston is forced to reciprocate back and forth between the two pulse combustors. By controlling the combustion timing, the frequency of oscillation can be adjusted.

The motion of the piston is utilized to generate electrical energy. Either a permanent magnet generator or a variable reluctance generator can be used, since these schemes do not require mechanical or electrical connections to the piston. The magnetic circuits were arranged such that the permanent magnets are not on or an integral part of the piston, but instead are embedded in the external walls of the generator, and can be, thus, insulated from the high temperature regions of the generator. In addition, the use of pulse combustion resulted in lower combustion process and wall temperatures due to cooling of the combustion products and wall by mixing and contact with cool air, respectively.

For the first three years of the MURI program, the major emphasis was on performing modeling, and numerical simulations of the pulse combustors and free piston generator and the development of magnetic generator topology. Critical experiments for model validation were carried out under separate funding from DARPA. The issues that were addressed included small-scale pulse combustion phenomena and modeling of combustion in high surface-to-volume ratio environments; design of ultracompact permanent-magnet-based and non-permanent-magnet-based, variable reluctance generators; and selection of appropriate materials and fabrication sequences for the realization of the various subcomponents of the generator using

micromachining technology as appropriate. In the final two years of the program the emphasis switched to fabrication and testing of critical subcomponents, in order to assess the advantages and limitations of the application of micromachining technology to the fabrication of microgenerator subcomponents. During the last phase of the project (under a no-cost extension) some limited simulations of close-loop control of the engine performance were conducted.

1. Model Development for Reciprocating Free-piston Pulse Combustor

Professor Ben T. Zinn

This section describes work toward the development of a reduced order model of the micro-power generator. This model consists of coupled non-linear ordinary differential equations that describe the temporal dynamics of the generator power output, chamber pressure, temperature, and piston location. The model describes the dependence of these quantities upon such parameters as fuel type, inlet and exhaust port location, piston mass, and magnet configuration. This model can be run very quickly on a desktop PC and generally requires around 10 seconds to compute the time history per engine cycle.

This reduced order model uses state of the art "multi-zone" modeling approaches developed in other internal combustion engine applications. It includes several sub-models to describe such processes as scavenging and exhaust, flame propagation, heat loss, flow leakage between chambers, and interactions between electrical and mechanical systems. Using the zonal modeling approach, each combustion chamber is assumed to consist of one or several interacting zones/regions. It is important to note that the number of zones within each chamber changes during the cycle. *Figure 1-1* pictorially describes the evolution of the modeled zones.

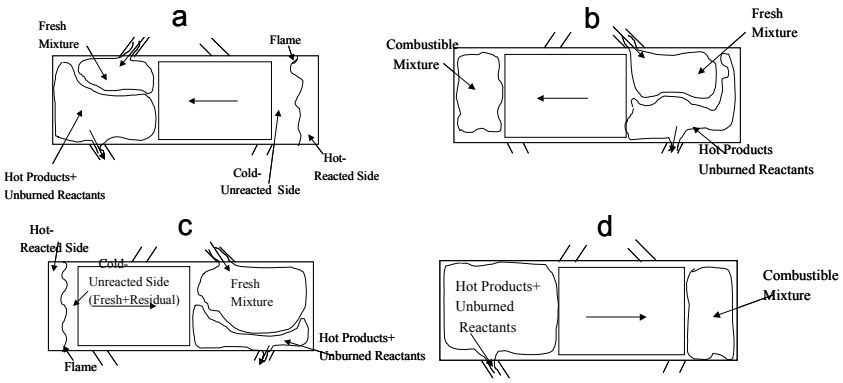

Figure 1-1. *Evolution of the modeled zones generator throughout one cycle of the microgenerator.*

Before proceeding, we will briefly review this modeling approach. Consider first the right combustor in *Fig. 1-1.a* at an instant when the reactants are being consumed by the flame. The temperature rise and expansion that accompany the consumption of reactants increase the combustor's pressure and force the piston leftward. As shown in *Fig. 1-1.a*, the right combustor is divided into two zones; i.e., the "hot" combustion products on the right and the "cold" gases on the left. The latter consists of a mixture of cold reactants and cold combustion products left from previous cycles. These regions are separated by the flame front. Independent mass and energy conservation equations are used to model each of these regions. Momentum conservation is invoked by assuming uniform pressure throughout the chamber. Sub-models describing flame propagation and heat losses are also incorporated to describe the interactions of these zones with each other and the environment. The flame propagation sub-model describes the rate of conversion of cold reactants into hot products and the heat loss sub-model describes the rate of energy transfer from each zone to the combustor walls and piston face.

As the piston moves to the left, it compresses the contents of the left combustor, which is assumed to consist of two main zones; i.e., the fresh reactants supplied through the inlet port and the hot products and unburned reactants that leave the combustor through the exhaust port. Separate models are used to describe the flow rates of reactants and hot gases into and out of the combustor. The gases in the hot products and unburned reactants zone are further divided into: 1) hot combustion products, 2) cold combustible gases, and 3) cold combustion products left from prior cycles (i.e., exhaust residual). Consequently, a total of four mass and energy conservation equations describe the behavior of the gases in the left combustor. Additional sub-models describe the mass and energy exchange between the zones and heat losses.

Figure 1-1.b illustrates the modeled zones at a later time in the cycle. At this instant, the inlet and exhaust ports of the left combustor are covered by the piston and the gases in the left combustor are compressed by the leftward moving piston. The fluid in the left combustor in *Fig. 1-1.b* consists of a mixture of combustible and residual gases. *Figure 1-1.b* also shows that at this instant, reactants are flowing into the right combustor while hot products and unburned reactants are exiting the combustor. The behavior of the gases in the right combustor in *Fig. 1-1.b* can be described by the zones used to describe the behavior of the gases in the left combustor in *Fig. 1-1.a.*

Figure 1-1.c illustrates the combustor zones at an instant after the mixture in the left combustor was ignited. At this state, the left combustor is assumed to consist of two zones separated by a flame, which are similar to the zones used to describe the right combustor in *Fig. 1-1.a*. At the same time, flow in the right combustor is assumed to consist of a "fresh mixture" and "hot products/unburned reactants" regions, which are similar to those in the left combustor in *Fig. 1-1.a*. The behavior of the flow in the right combustor is described by these zones until the instant when the intake and exhaust ports are covered by the rightward moving piston. The final "state" of the cycle, when the gases leave the left combustor and the piston compresses the gases in the right combustor, is shown in *Fig. 1-1.d*. At the "end" of the state shown in *Fig. 1-1.d*, the cycle repeats itself.

These temporal dynamics are illustrated in a typical result, see *Fig. 1-2*, that illustrates the dependence of combustor pressure upon time. The figure shows the initial smooth rise in pressure due to compression. The sharp jump in pressure indicates the occurrence of combustion, which is followed by a smooth pressure drop during the expansion phase of the

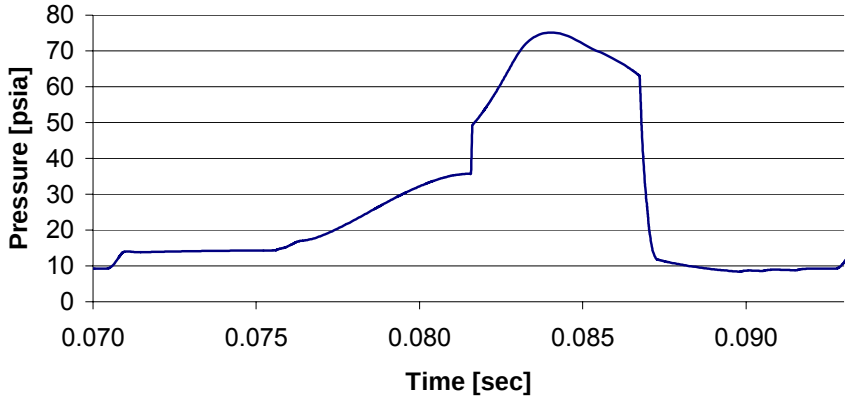

Figure 1-2. *Typical predicted time dependence of pressure in a single combustion chamber*

cycle. Since the outflow of gases from the combustor continues when the combustor's pressure equals the outside pressure due to inertial effects, a slight vacuum occurs in the combustor.

Recent work has concentrated on refining sub-models that describe phenomenon that critically effect generator performance. We have refined our heat loss model by incorporating an empirical correlation developed by Woschni [1] for other internal combustion engines. This correlation assumes that heat loss can be represented as $h \times Area \times (T_{gas} - T_{wall})$. The Woschni model describes the dependence of the heat loss coefficient (h) upon engine size, speed, and instantaneous chamber pressure and temperature. We have also developed a time dependent, finite difference scheme to calculate the instantaneous wall temperature (T_{wall}) that is needed in this correlation. This finite difference scheme describes the unsteady, heat conduction in the generator walls. It is a *Crank Nicholson* scheme, which is stable for any grid size. Model results predict a steady state inner wall temperature of about 600K (~350°C).

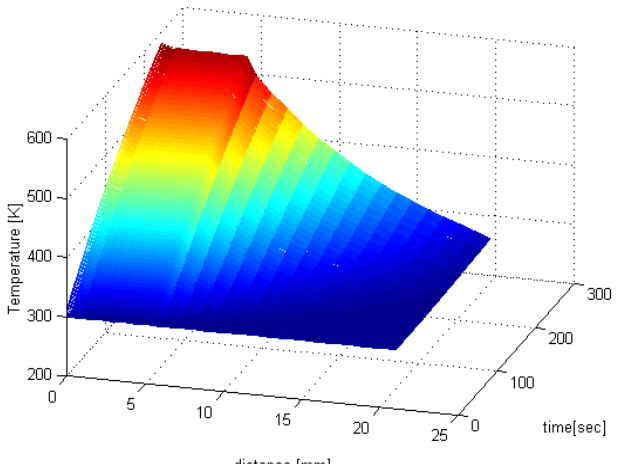

Figure 1-3. *Typical calculated dependence of transient wall temperature distribution after startup of generator*

Using this refined heat transfer model, we have examined several methods for reducing the outer surface temperature that do not require external cooling. Results indicate that 1 cm of insulating material, such as a ceramic, will prevent the steady state, outer wall temperature from rising more than 10°C over its ambient value. *Figure 1-3* shows the wall temperature dependence upon time and depth into the wall material. An apparent change in the slope of temperature curve can be seen on the interface between the chamber's steel wall and the insulating material.

Work was also performed to improve the piston friction loss model. The current model determines friction losses by calculating the wall shear stress that is obtained by assuming a laminar Couette flow velocity distribution in the piston-wall gap. It is also assumed that the lubricating fluid is at the wall temperature. Simulations suggest, however, that modeling these friction forces is not critical because they appear to introduce losses that are minor relative to those contributed by other processes; e.g., heat loss and gas leakages between chambers. *Figure 1-4* compares the calculated force due to chamber overpressure and wall-friction forces.

Figure 1-4 shows that the viscous forces are quite small relative to those exerted by the gases on the piston. This result implies that a high fidelity friction loss model is not critical in describing the generator's dynamics.

Model results obtained thus far have been compared with available experimental data in order to validate it and suggest areas in need of refinement. *Figure 1-5* compares the pressure-volume (P-V) relationship that was measured and predicted by the developed model.

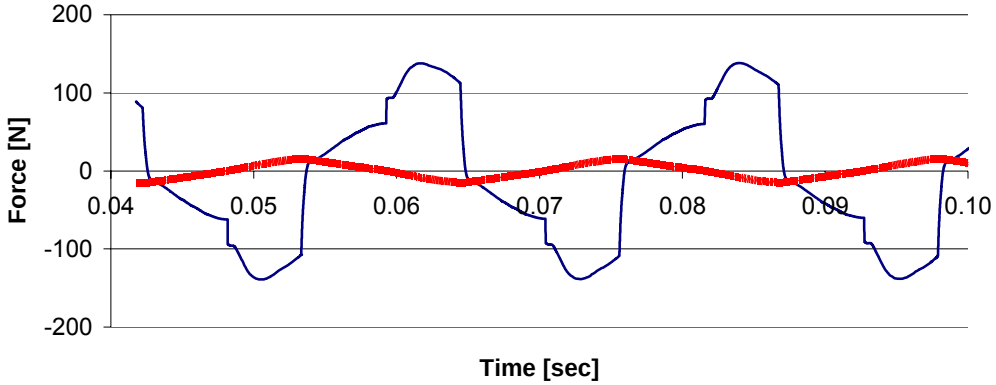

Figure 1-4. *Predicted time dependence of pressure and viscous forces acting on piston. The smaller, dashed curve is that of the friction force.*

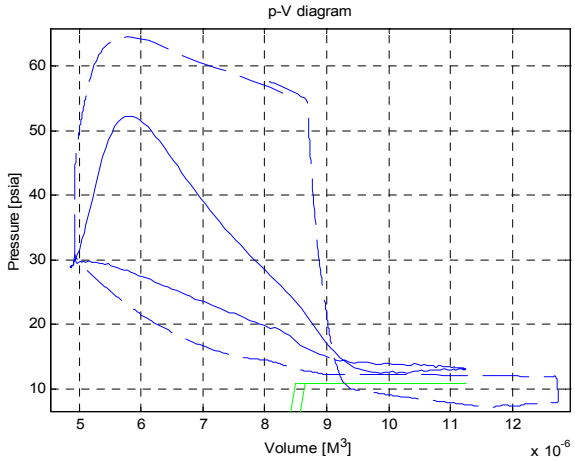

Figure 1-5*. Measured and predicted combustor p-v diagrams. The larger, dashed p-v curve is obtained from computer model, while the smaller, solid curve is obtained from an experiment*

As can be seen from the figure, the model does a reasonable job of describing the pressure-volume relationships in the chamber. It can also be seen that there are quantitative differences, indicating the need for further refinement of the model. Specifically, it can be seen that the area enclosed in the modeled p-v diagram (which is proportional to generator power output) is larger than that measured. This result suggests that actual generator losses are somewhat larger than those incorporated in the model.

We also have performed extensive parametric studies of the effect of inlet and exhaust port location. It has been found that, in general, locating the outlet valves closer to the centerline of the microgenerator results in maximum generator power output. If placed too far from the centerline, the gas exchange process becomes "expensive", as it potentially exhausts mixtures still burning in the chamber, and thus reduces available overpressure generated by combustion. On the other hand, the valves may not open at all, or not have sufficient time to allow intake of fresh gases and exhausting of product gases, if they are located too close to the centerline. This result is presented in *Figure 1-6*.

Additional studies have been performed to analyze the optimum method of extracting power from the piston by magnetic forces. Since the energy extracted by the magnets is related

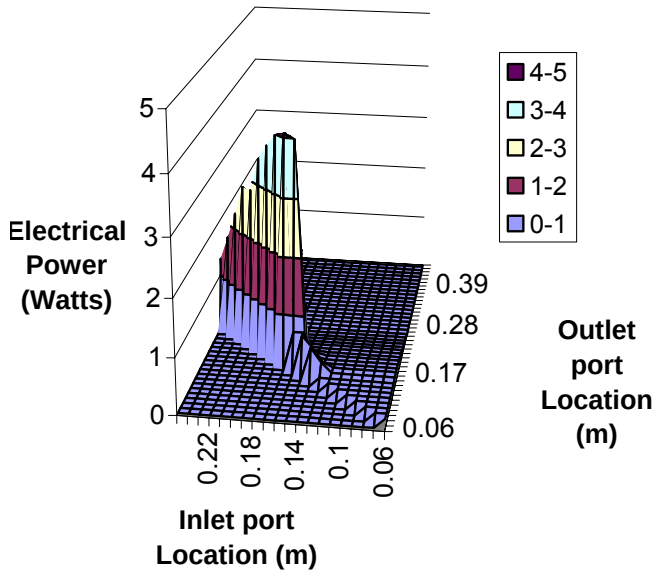

Figure 1-6*. Generator power output as a function of intake and exhaust port location, measured from the centerline of microgenerator*

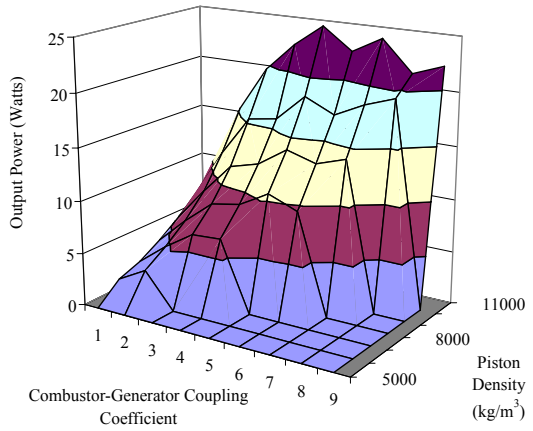

Figure 1-7*. Predicted dependence of generator power output upon piston density and magnetic resistive force*

to the product of the piston velocity and magnetic force, two distinct options are possible: 1) Allow for high piston velocity by utilizing magnets that exert small forces on the piston, 2) utilize magnets exerting large forces on the piston that will result in lower piston velocities. Because of this tradeoff between piston velocity and magnetic resistive force, we performed parametric studies to determine the optimum magnetic force that resulted in maximum electrical power generation. *Figure 1-7* below presents the predicted dependence of the micro-generator's power output upon the piston's density and the "coupling coefficient", which is related to the force exerted by the generator's magnets upon the oscillating piston, for a fixed micro-generator configuration. This result indicates that maximum power is generated with the largest magnetic resistive force possible that does not cause the engine to "stall". The figure also suggests that power output is maximized with high density pistons (that have lower velocities).

In summary, the developed model has shown to be a useful, flexible tool for predicting combustor performance with results that show reasonable agreement with current available data.

Additional efforts under this task employed the above-described, reduced order micro-power-generator model to determine the dependence of the micro-power-generator performance upon various design and operating parameters. This was done in an effort to check the validity of the model and to guide design of improved micro-power-generators, which were being developed under other tasks of this program. First, in order to gain insight into important parameters affecting the system's performance, we investigated the effect of wall heat losses upon the combustor efficiency. Using an unsteady thermal boundary layer analysis to simulate wall losses, we addressed the following questions: 1) How does the temperature gradient (and, thus, the heat losses) at the wall change with frequency and generator dimensions? and 2) Assuming that the combustion process will be quenched or substantially inhibited in the thermal boundary layer next to the combustor walls, what fraction of the combustion chamber volume will be available for "uninhibited" chemical reactions?

Since past analyses have shown that the temperature of the combustor walls does not substantially change over a cycle, we examined the solution to a model problem where the wall temperature is fixed at T_w, and the temperature inside a duct of width, h, varies harmonically with time due to an unsteady heat source. The equation describing the temperature profile and its solution are:

$$\frac{\partial T}{\partial t} = \alpha \frac{\partial^2 T}{\partial y^2} + Qe^{2\pi ift} \Rightarrow \frac{T(y,t) - T_w}{T(y,t) - T_w} = \frac{\cosh\left(\sqrt{\frac{2\pi ifh^2}{\alpha}}\right) - \cosh\left(\sqrt{\frac{2\pi ifh^2}{\alpha}}\frac{y}{h}\right)}{\cosh\left(\sqrt{\frac{2\pi ifh^2}{\alpha}}\right) - \sinh\left(\sqrt{\frac{2\pi ifh^2}{\alpha}}\frac{y}{h}\right)/\sqrt{\frac{2\pi ifh^2}{\alpha}}} e^{2\pi ift} \qquad (1)$$

where

α = thermal conductivity coefficient, at T=500 C, ~1.14 cm^2/s
h = thickness of generator wall, value in proposal is 2 mm
y = distance normal to the wall

Plots of the normalized temperature profiles for several different generator widths, h, are plotted in Figure 1-8 below when the generator oscillated at a frequency f=40 Hz. and the thermal diffusivity α was assumed to equal 1.14 cm^2/s.

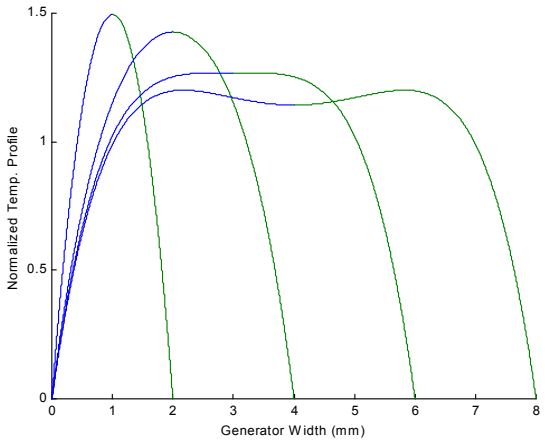

Figure 1-8. *Dependence of normalized temperature profile upon generator width.*

For small values of the generator width, h, the conduction time scales are much faster than the period of the oscillations and the temperature assumes a quasi-steady profile. As h increases, the effect of the opposite wall exerts less and less influence on the temperature profile, and it begins to approach a Stokes profile. An examination of Figure 1-8 shows that: 1) The temperature gradient (which affects the heat losses) at the wall decreases monotonically as the generator width increases and it attains a constant value for all generator widths larger than a certain threshold value, and 2) The thermal boundary layer (where presumably the combustion process will be quenched) occupies a monotonically smaller fraction of the combustor as the combustor's width increases. The first observation suggests that *heat losses will not be significantly reduced by increasing the generator's width* h *once the generator width is above a certain value*.

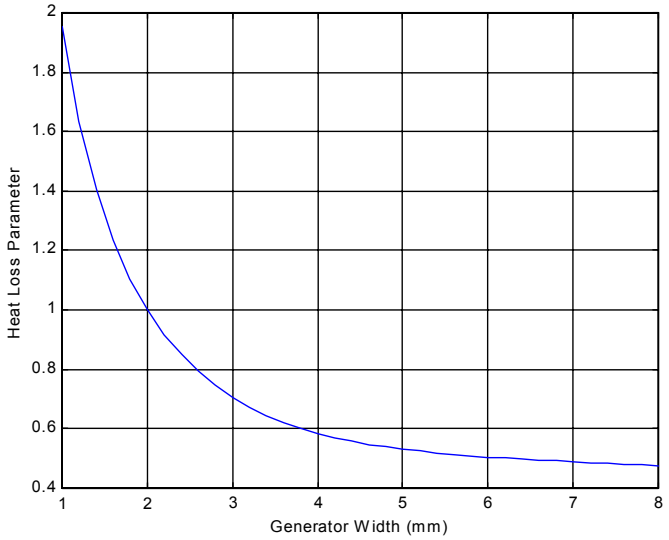

Figure 1-9. *Dependence of the generator's wall temperature gradient, which is proportional to the wall heat loss, upon generator's width.*

This observation is quantified below in Figure 1-9 where the dependence of the wall temperature gradient (normalized by its value at h= 2mm) upon the generator's width h is described.

The data presented in Figure 1-9 suggests that heat losses can be reduced by 40% by increasing the generator width from 2 to 4 mm. It also suggests that further reductions of heat losses with increasing width will be relatively minor.

Figure 1-10 shows the dependence of the "Reaction Zone Width", normalized by its value at h=2 mm, upon the generator width. The reaction zone width is defined as the portion of the generator where the temperature exceeds 90% of its center line value.

The plot in Figure 1-10 suggests that the reaction zone width, which could be considered to be a measure of the combustion efficiency, can be increased 150% by doubling the generator width from h=2 mm, and over 800% by quadrupling it.

We also performed a theoretical analysis of the factors affecting the frequency of the generator oscillations in order to assist us in the interpretation of measured data. Essentially, the compressed air acts as a spring and the piston as a mass. Using a simple linearized analysis that assumes isentropic compression and expansion, the following expression for the natural frequency of operation of the generator was derived:

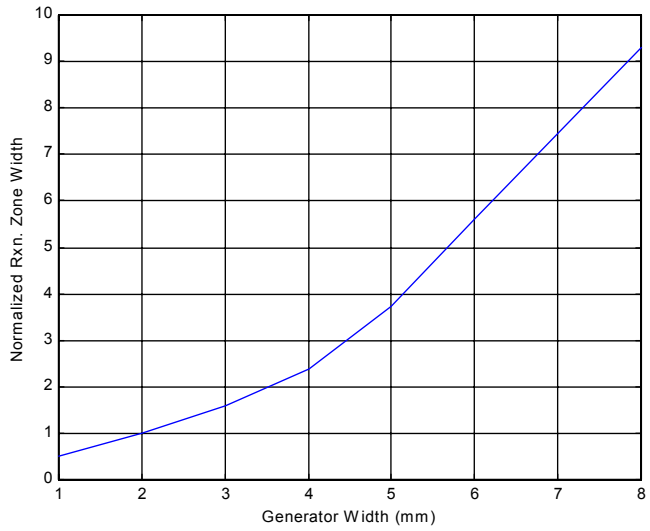

Figure 1-10. *Dependence of normalized reaction zone width upon generator width.*

$$f = \frac{c}{\pi L}\frac{1}{\sqrt{(\rho_p/\rho)(L_p/L)(1-L_p/L)}} \qquad (2)$$

where:

c=ambient speed of sound
L = Total length of generator
ρ_p=Piston density

It is of interest to consider the effect of the piston length relative to the total chamber length on this frequency because, from an electrical conversion point of view, it is preferable to have a longer piston. Equation (6) shows that the minimum frequency occurs at Lp/L =0.5, and that the frequency increases when the ratio Lp/L is above or below this value. The dependence of the ratio of the nondimensional frequency (normalized by its value at Lp/L=0.5) upon Lp/L is plotted in Figure 1-11 below:

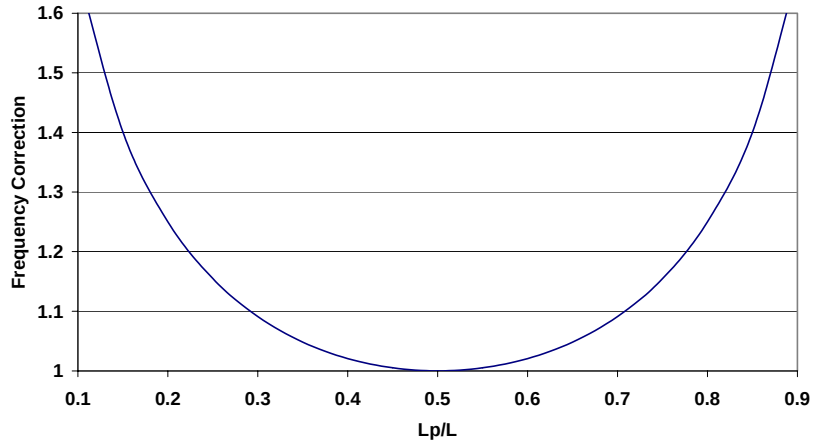

Figure 1-11. *Dependence of generator frequency upon piston volume fraction.*

Figure 1-11 shows that changing the piston length from the value of Lp/L=0.5 will have a very small effect on the oscillation frequency. It should be noted, however, that increasing the piston length from this value will decrease the volume available for combustion, see Eq. (1), thus causing a decrease in power density.

Equation (2) was derived from a linear analysis, which assumed very small piston displacements. For larger displacements, the gas in the chambers act as "stiffening springs" and the frequency increases with increasing displacement. The following differential equation can be shown to describe the piston oscillations when the amplitudes of the piston oscillations are not negligible:

$$\frac{d^2\tilde{V}}{d\tilde{t}^2}+\frac{1}{2\gamma}\left(\frac{1}{(1-\tilde{V})^{\gamma}}-\frac{1}{(1+\tilde{V})^{\gamma}}\right)=0 \qquad (3)$$

In Eq. (3), the volume and time have been normalized by the maximum volume of the chamber and the linear natural frequency of oscillation, respectively. The compression ratio that the generator is operating at is a convenient measure of the departure from linearity. Figure 1-12 below shows the dependence of the frequency correction upon the compression ratio:

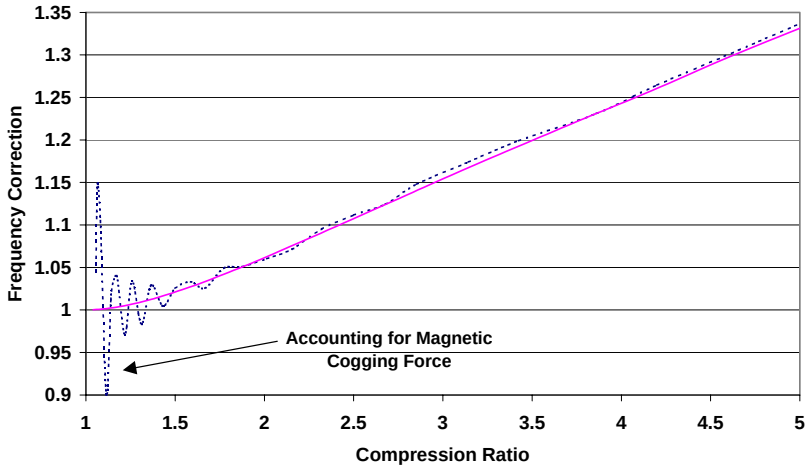

Figure 1-12. *Effect of compression ratio upon the departure of the generator frequency from its linear value.*

Figure 1-12 shows that the generator will operate at higher frequencies with increasing compression ratio.

The analysis above did not consider the affects of the generator forces upon frequency. We also performed an analysis of the affect of these forces. The resistive forces that extract power from the combustion section primarily cause damping and do not substantially alter its frequency characteristics. However, the conservative cogging forces exerted by the generator's magnets can have an important effect at low compression ratios. Their affect is also plotted in Figure 1-12. The Figure 1-shows that the magnetic cogging forces have significant effects upon generator dynamics at compression ratios below about two. This result shows that the transient behavior of the generator near startup (where the compression ratio is initially low) will be strongly affected by the electrical components.

In summary, the developed model has proven to be a useful, flexible tool for predicting the dependence of the combustor's performance upon design variables and operating conditions. It noteworthy that the model's predictions are in reasonable agreement with available data.

2. Simulation of Combustion-Driven Micro Power Generator

Professor Suresh Menon

Introduction

A free piston engine is a device that employs combustion to establish into cyclic motion a piston that is then used to directly produce energy. In general, a free piston engine can be used to generate hydraulic, pneumatic or electrical energy and past designs have employed either a single piston or an opposed or dual piston setup depending on the position of the combustion chamber(s) and piston(s). The relevance of several design parameters, such as the fuel injection timing, energy conversion efficiency, sealing and losses have been discussed earlier [1] in the context of past designs. Some of these issues will be re-addressed in the present study. In another recent study [2] the application of free piston configuration with opposed combustors was discussed as a device for generating electrical energy. They presented results for a ``Benchtop Model'' where the emphasis was on obtaining the experimental pressure versus volume diagram since this type of information can give simple order of magnitude estimate of the efficiency of power conversion.

The various free-piston engines discussed in the above noted papers were of dimensions that were small but not necessarily considered an extreme limit. Recently, with the advent of MEMS technology application to practical systems, there has been considerable interest in investigating systems that are either very small (i.e.,micron-scale) or devices that require MEMS fabrication technology in order to build the device. Micro-engines that employ both these approaches are being investigated. An example of a MEMS-scale engine is the micro-turbine being developed at MIT [3], whereas a device that is small enough to require MEMS fabrication technology is currently being developed at Georgia Tech [4].

A key feature of all these designs is the need to demonstrate a very small device capable of producing appreciable energy (e.g., 10-30 Watts of electrical power) in order to be useful for practical application. Of special interest in the present study is a device that employs fluidic power, i.e., combustion, to drive the generator to obtain electric power. Compared to conventional power sources, MEMS manufactured generators will have a high power density and a relatively long life. As a result, such a device may find many applications both in military and civilian fields. For example, an application of key interest to the US Army is the ability to provide portable power for the systems a soldier must carry. Thus, a system independent ``soldier'' power pack could have many applications. A device under development at Georgia Tech incorporates a free piston located between two opposed combustors. This piston is set into motion due to out-of-phase combustion in the two opposed combustors. To generate electric power from this device, the entire assembly is confined inside a magnet array. The interaction of the magnetic field with the piston motion generates the required electric energy. A schematic of this device is shown in Fig.2. Note that, the actual scale of the entire device (including the magnetic array) is no larger than a pack of playing cards.

Although the above device is conceptually sound, the aforementioned problems regarding achieving cyclically consistent and accurate injection, mixing, ignition and combustion within a very small combustor (in order to generate sustained steady-state electric power) requires significant optimization of the design of the device. Key parameters include the location of the inflow and outflow ports, the timing of the opening and closing of these ports, and control of leakage and heat transfer loss from the system. The various problems associated with optimizing these parameters has led the experimental effort to a more simplified configuration in which the engine consists of a single combustor with the other combustor replaced by a spring that

provides a pre-defined force to mimic the ``phantom'' combustor. A similar device is numerically simulated in the present paper using LES. In the following sections we describe the problems addressed in this research and the results obtained. It is to be noted that to the authors' knowledge this is the first attempt to simulate a free piston combustion system using LES. Furthermore, the results of the present LES effort is being used to provide guidelines for the hardware construction. Therefore, this effort provides an unique demonstration of the ability and the use of LES results for practical design of complex systems.

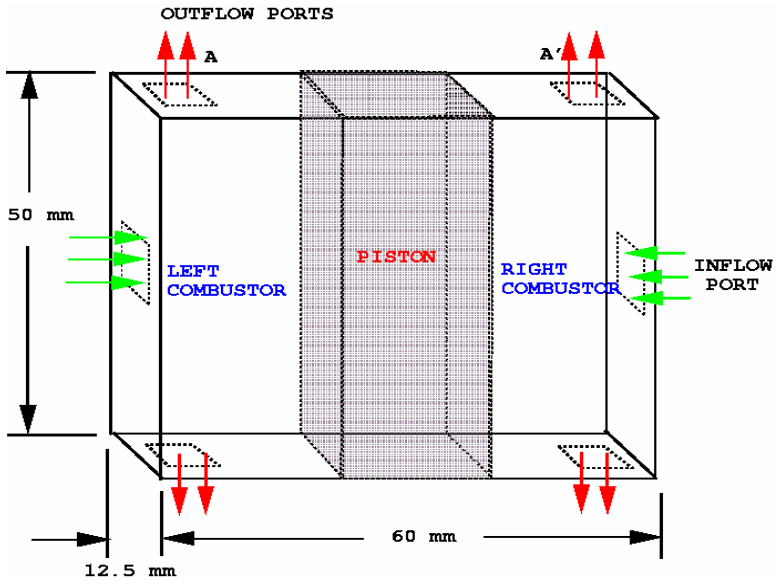

***Figure 2.1-1**: Schematic of the micro power generator*

2.1 APPLICATION OF LES MODEL TO DESIGN LEVEL STUDIES FOR IDENTIFICATION OF DESIGN PARAMETERS

Simulation Model

Numerical simulations are carried out by solving the full, unsteady, compressible Navier-Stokes equations using a finite-volume scheme that is second-order accurate in time and fourth-order in space. This scheme has been used extensively in the past [6,7] for both DNS and large eddy simulations (LES). Computational details has been presented elsewhere[8] and therefore will only be briefly presented here. No-slip boundary conditions are applied on all walls for the velocity field. Since unsteady heat transfer to the wall has been identified as an important factor in the experimental studies, a time-dependent heat flux boundary condition is employed during some stages of the combustion process as described later in the reference[8]. For simplicity, mass loss from the domain in-between the piston and the wall is neglected. The retarding force due to the magnetic coils is also not considered. These issues will be addressed in a future study. Thus, the present form of the simulated problem is a pure combustion problem with moving boundaries. Notice that the spanwise dimension is much smaller than the other two directions and thus, this device has a very high aspect ratio. Inflow conditions are specified using characteristic inflow conditions. Randomly generated turbulent fluctuations are added to the inflow velocity and subgrid kinetic energy is also specified at the inflow. Typical values used here are taken from Tabaczynski[5]. The exit pressure is specified at the outflow and all other variables are extrapolated from the interior.

Results and Discussion

Since the combustion process in the device is mainly confined in nature, the behavior of combustion in a small constant volume is investigated, first. Combustion with moving piston is then studied.

Constant volume combustion: Issues of particular interest include the characteristics and limits of laminar flame propagation in a small volume, the effect of high aspect ratio combustor volume, heat losses to chamber walls, location(s) of ignition source and ignition energy. A combustion chamber 50 *mm* long x 13 *mm* wide x 6.5 *mm* thick is simulated. In the actual experiments premixed flames propagate into an initially stagnant fluid from three ignition (spark) sources located against one of the 50 *mm* x 13 *mm* walls. The simulations are carried out using both 2D and 3D versions of the code. A 3D grid (uniform in all directions) of 60 x 100 x 10 is employed (for 2D, a 60 x 100 grid was used). Since, the actual plasma volume and conditions generated by the spark system used in the experiments is very difficult to reproduce, the fuel-air mixture is ignited using hot spots (with initial temperature of 1800 *K*) in the simulations.

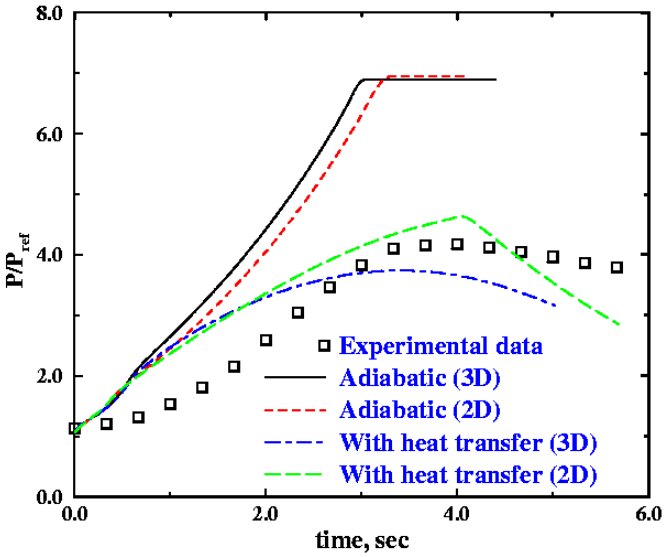

Figure 2.1-2: *Prediction of pressure rise in a constant volume micro combustor for both adiabatic and heat transfer cases. Some experimental data is also shown.*

Figure 2.1-2 shows the simulated results and some available data. Initial studies using adiabatic no-slip walls showed that the pressure rise in the chamber is very high, of the order of 7 atm. However, experimental data consistently showed a much lower pressure rise of around 4 atm, which was attributed to heat loss from the combustor walls. A wall heat transfer model to include this heat loss has been developed to approximately match the data. Different values of heat loss coefficient, C_f are investigated. Figure 2.1-2 shows the case for which qualitative agreement with experimental data was obtained in both 2D and 3D simulations.

Combustion-driven piston oscillation: Using a multi-domain version of the parallel codes, the two combustors were assigned to two separate domains each with an identical number of processors. The (opposite) end wall in each combustor is the piston head and the only communication between the two domains is the average pressure on the piston head. As the

piston oscillates, the combustor length varies within a range that is determined by the amplitude of piston motion. In order to achieve a steady-state piston oscillations it is very important that the initial concentrations (which must be close to stoichiometric mixture otherwise ignition will not occurred) and volume of the reactants in each chamber must be identical. Otherwise a symmetric oscillation can not be obtained and after a few stroke oscillations will be terminated. Keeping these in mind, several designs were simulated in-terms of position, size and locations of the inflow and outflow. Some of these design concepts are outlined in Figure 2.1-3.

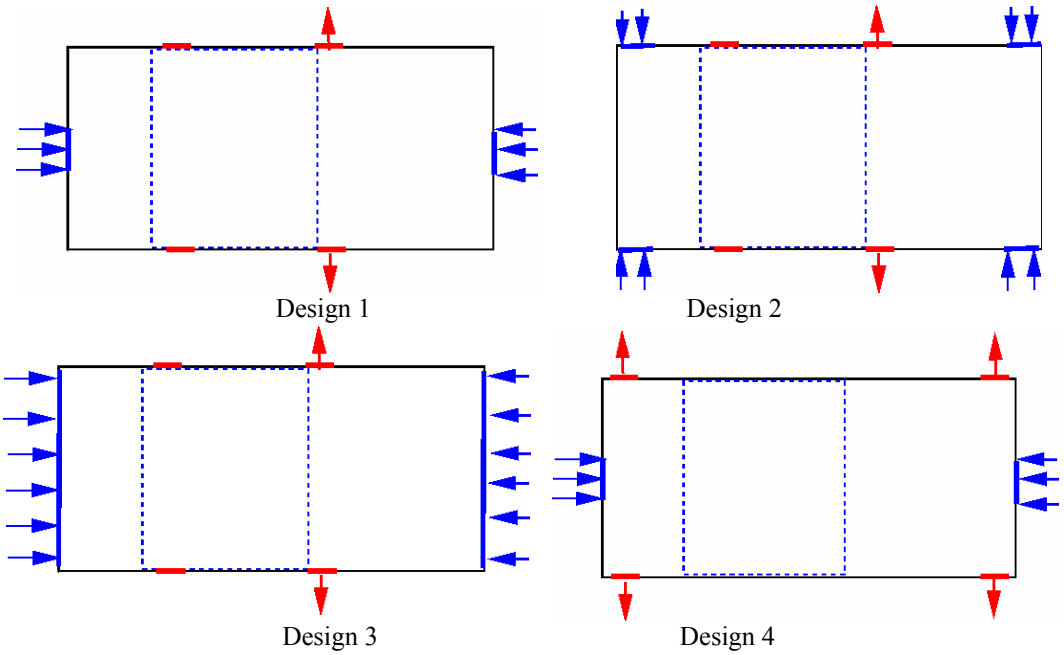

***Figure 2.1-3**: Different designs showing inflow and outflow ports positions.*

Out of the four designs shown in Figure 2.1-3, the designs 1 and 2 did not work as both of these designs failed to remove the burnt products (Figure 2.1-4) efficiently. Parametric studies are carried out using 2D code for all the designs. Design 4 is then tested using 3D code and compared with 2D results. Both 2D and 3D show similar behavior. Figure 2.1-5 shows a typical pressure signature (normalized by the ambient pressure) in design-1 for 3D (Figure 2.1-5a) and 2D (Figure 2.1-5b) simulations respectively. Pressure oscillations show a significant similarity that suggests that we can employ the strategy of using 2D simulations to evaluate various design parameters and then fine-tune the design using 3D simulations.

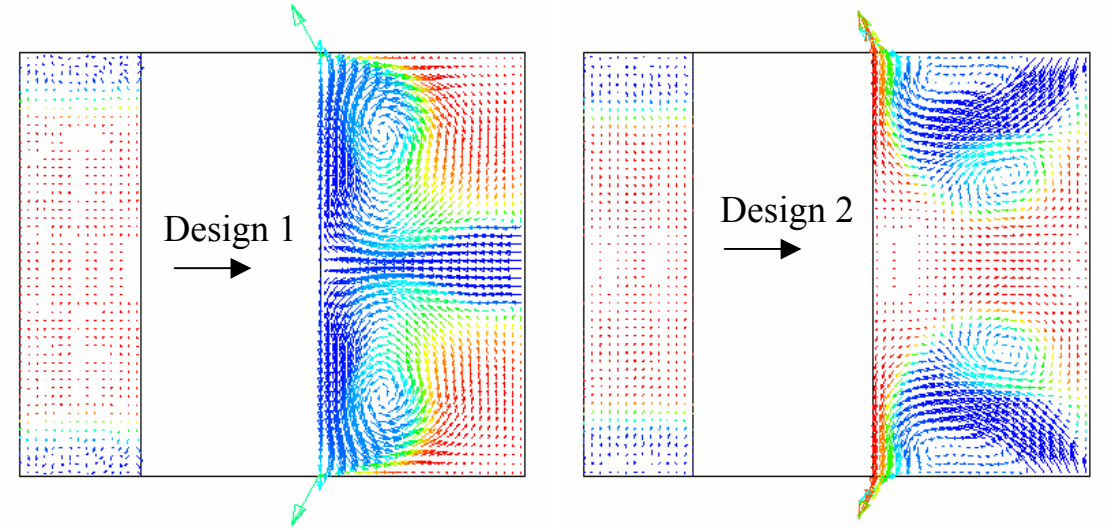

Figure 2.1-4: *Velocity vectors colored by concentrations of products (red) and reactants (blue). Both designs show trapped products in the second chamber.*

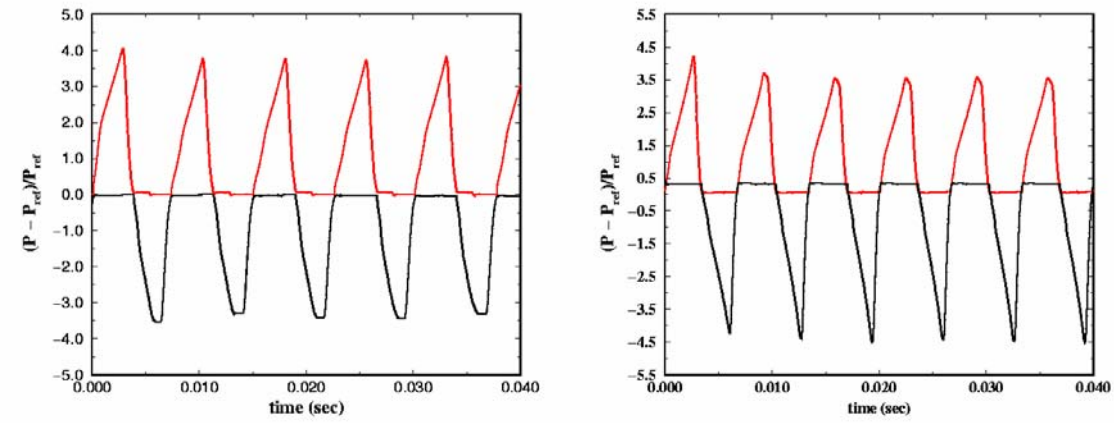

Figure 2.1-5*: Pressure Oscillations for 3D and 2D simulations with identical conditions.*

A 3D perspective of velocity vectors and concentrations of reactants (blue) and products (red) is shown in Figure 2.1-6. The instant shows correspond to a position where ignition started in the right chamber and inflow opened in the left chamber. Incoming reactants push the products out through the outflow ports. As the simulation results for both 2D and 3D are similar a typical cycle is described for the 3D simulation in Figure 2.1-7. In the figure three representative locations are presented. Upper panel shows the velocity vectors colored by temperature and lower panel shows the concentrations of reactants (blue) and products (red). Location (a) shows the ignition in right chamber, fresh reactants entering and burnt products escaping from the left chamber. Piston moves from right-to-left. Location (b) shows that the left chamber is filled with reactants and right chamber filled with products. At this location piston reached at the left-most position and this chamber is ready to ignite. Location (c) is opposite of location (a) i.e., ignition started in left chamber and fresh reactant is entering.

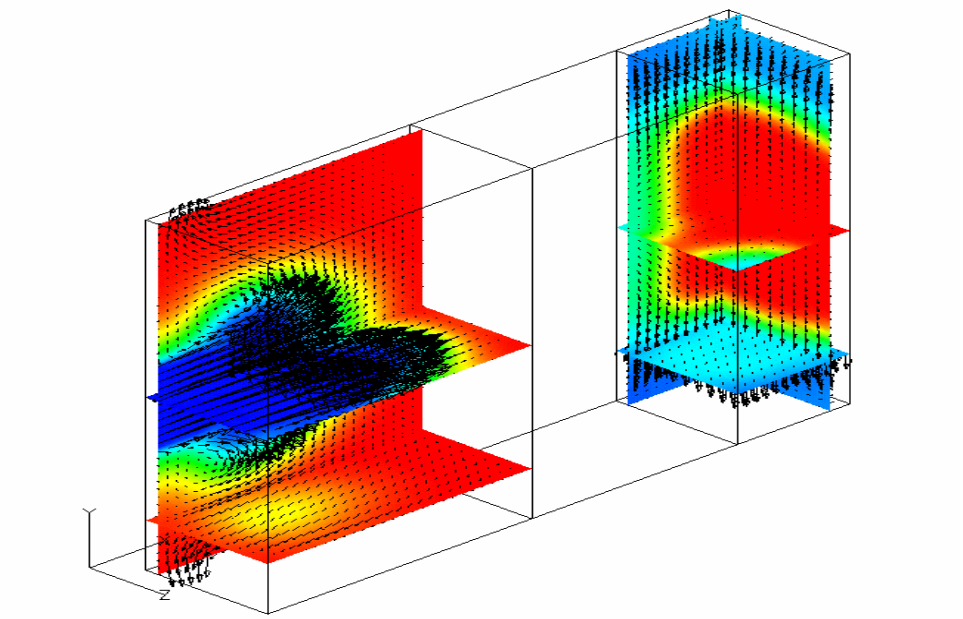

***Figure 2.1-6**: A 3-D perspective of velocity vectors and concentrations*

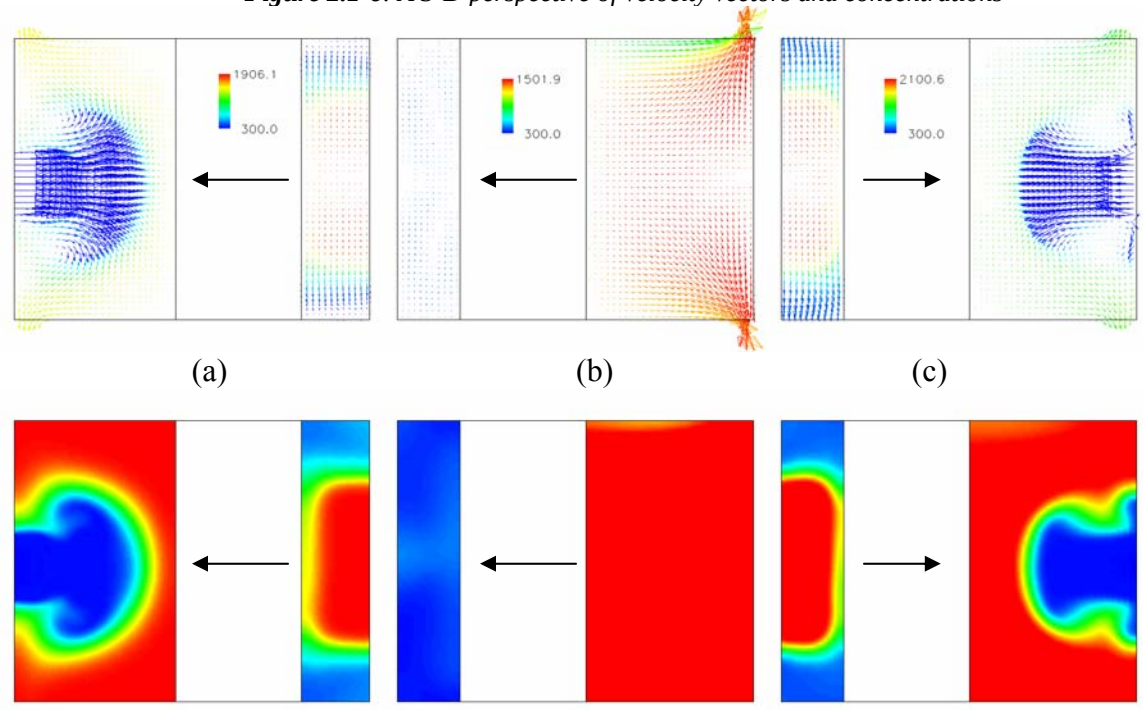

***Figure 2.1-7**: Velocity vectors colored by temperature [upper panel] and concentrations of reactants (blue) & products (red) [lower panel] for 3D simulations.*

The Spring Forced Combustor Model

The current research effort is focused on a simpler device and a planform view of the engine is given in Fig.8. This design was chosen for the experimental effort to address some problems related to achieving cyclic combustion in the dual system and to understand the dynamics of the process. Typical dimensions and parameters for this experimental device are summarized in Ref.-8. To properly resolve this domain, a computational grid of 191x101x13 is used and for this resolution the grid size is about 0.5mm in all directions.
The free piston engine has two scavenging ports one of which is also used for inflow of

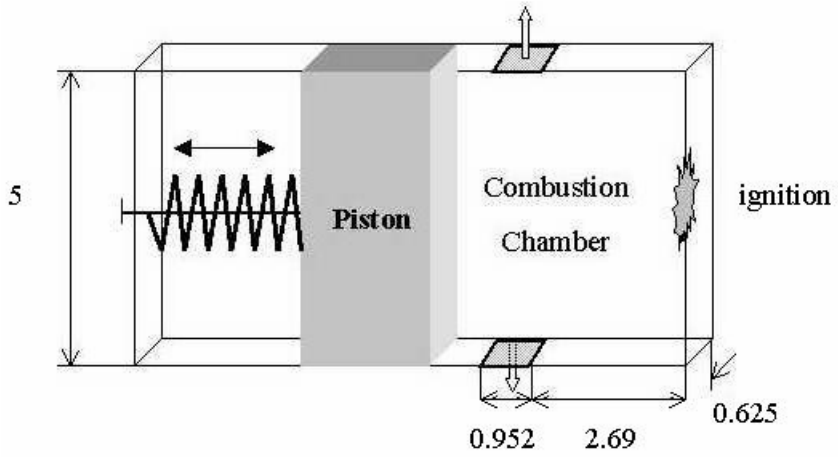

Figure 2.1-8. *Schematic of the spring forced combustor.*

premixed reactants. In a typical cycle of combustion, there are three phases: an intake phase, a combustion phase and an exhaust phase. In the experiments, the injection is at an angle from one of the ports to the wall where reactants will eventually be ignited.

The intake phase is a continuous one, in other words, if the pressure in the chamber is below a predetermined value then injection of the reactants will occur provided that the ports are open. During the intake phase, pre-compression occurs and before the piston reaches TDC (Top Dead Center), ignition occurs. The ignition time is of the order of 0.2msec. After ignition, flame propagation, volumetric expansion and pressure rise effects causes the piston to move back to Bottom Dead Center (BDC) which is the end of one cycle. Note that, there is no outside interference to control the opening and closing of the ports. Rather, the opening and closing of the ports is done automatically by the moving piston itself. Thus, piston, during its motion, acts as an actuating mechanism so that, depending on the position of the piston, the ports might be open or closed. This is an important design consideration for this engine because other means of controlling the state of the ports will require supplementary mechanism(s). Integration of such a control mechanism in a small device will increase the complexity and drive up the cost and therefore, is to be avoided. Since the piston motion controls the status of the ports (i.e., open/closed) it can effect a variety of things, such as the maximum pressure obtained, the concentration of the unburned reactants just before the exhaust ports opens, the amount of burnt products remaining, etc.,and through these effects directly impact the oscillatory state of the combustion process and the frequency of oscillation. The frequency of oscillation directly controls the power generated by this device and therefore, achieving a fixed frequency is critical

for the success of this design. Hence, for a given fuel mixture, the ports should be at a location (relative to ignition zone) such that combustion is completed before the exhaust phase. This point is closely linked to other phenomena such as the turbulence level in the combustor during combustion and quenching especially near the walls. The latter has particular importance in the present context since the combustor has very small spanwise dimension and the flame will reach the lateral walls before it reaches the other walls.

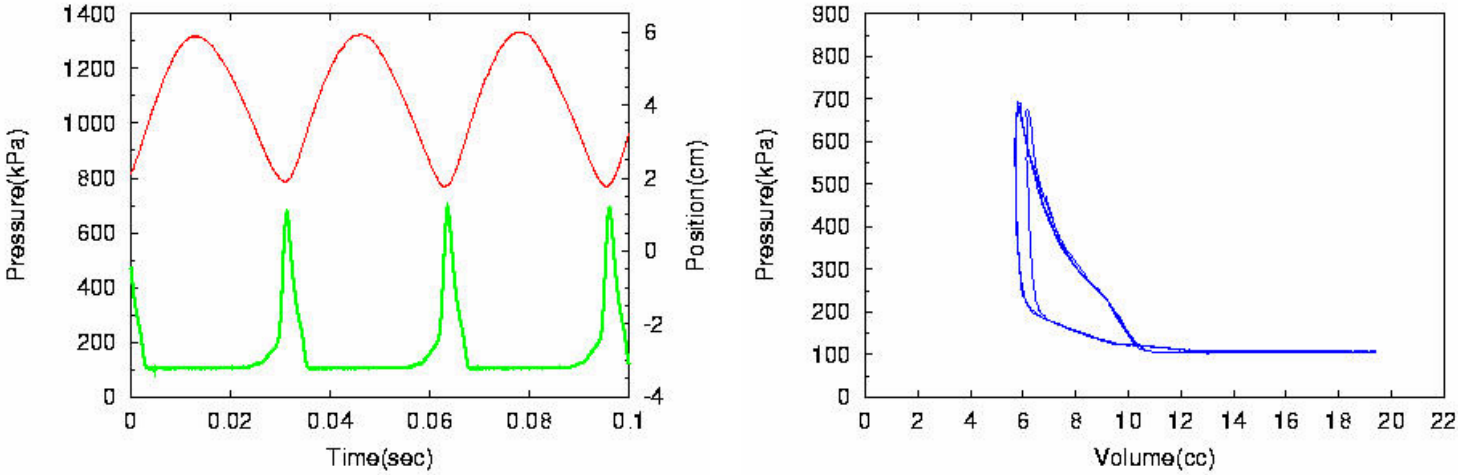

(a) (b)

Figure 2.1-9. *Experimental data. (a) Pressure and piston position; (b) P-V diagram*

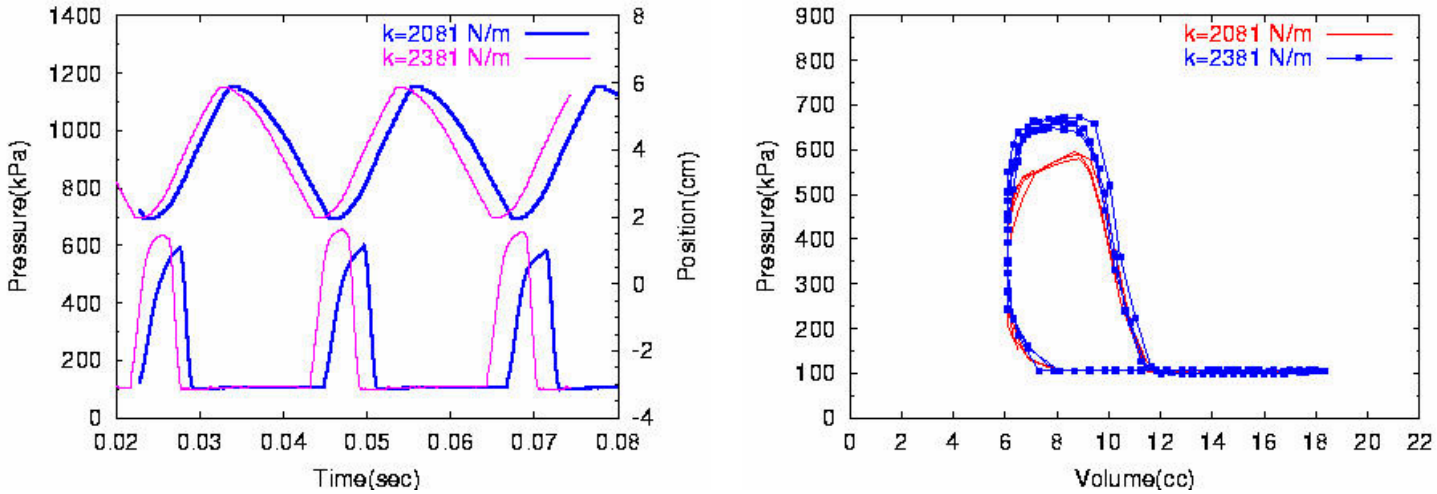

(a) (b)

Figure 2.1-10. *Numerical data. (a) Pressure and piston position; (b) P-V diagram*

Recently some experimental results has been reported (Zinn et. all), mainly for pressure history and position of the piston. So far, three combustors of different size have been experimentally studied [4] but only one with chamber thickness of 6.25 mm is simulated here.

Experimentally, this combustor achieved sustained oscillation as described below. Experimental pressure and position history are given in Fig.9. Corresponding numerical solution is also shown in Fig.10. General trends are captured well in the numerical solution. There are, however, some differences as well. The ignition in the numerical solution is somewhat slower which in turn impact the combustion process. As noted earlier, the ignition process used in experiments (multiple spark plugs) is very difficult to mimic in the numerical approach and therefore, some discrepancy in the initial period is expected. In the real configuration, as can be seen in Fig.9, combustion is almost finished at TDC, which explains the relatively higher peak pressure obtained

On the other hand, in the numerical simulation (Fig.10) combustion continues even after TDC. There could be various reasons for this difference. For example, it may be a consequence of the limitation of the EBU (Eddy Break-Up) reaction rate closure model that is employed here which will impact the chemical conversion rate. Additionally, the magnitude of inflow turbulence (which in turn can effect the mixing time scale) could impact this result. At present, there are no measurements in the combustor to determine some of these quantities and therefore, additional simulations with different conditions may be necessary to determine the difference

Another observation is that the experimental pressure begins to decrease long before the ports are open and as a result, the P-V experimental diagram is both qualitatively and quantitatively different than the computed P-V diagram. These figures are shown in Figure 2.1-9-b and Figure 2.1-10-b, respectively. This difference can be attributed to heat and mass losses observed in the experiments (and which are not currently included in the model) and the model for the spring constant for the simulation. At present, there is no quantified information available from the experiments for these parameters and other parameters such as retarding force due to the generator, etc., and one has to resort to guessing their values. For example, the experimental value of the spring constant k=1183.3 N/m was not sufficient in the simulation since phenomena such as the losses and retarding force were unaccounted. We resorted to including their effect by increasing the spring constant in an ad hoc manner. To determine the sensitivity of the simulations to the choice of the spring constant, two simulations were carried out using different values of the spring constants: k=2081 N/m and k=2381 N/m (as shown above). Increasing the spring constant slightly increases the peak pressure and the stroke length of the piston but the frequency is almost unchanged. Higher spring constant give more time near TDC and this explains the slight pressure increase. On the other hand, it also accelerates the return to TDC from BDC, thus tending to compensate for frequency. These results suggest that more information from the experimental device is needed to fully model all the features in this device. It should be noted that although the spring constant was increased above the experimental value to model for the missing effects, it still gives a linear response in space. However, the neglected factors may all contribute to nonlinearity to a certain degree and therefore, without further quantified information from the experiments (which is likely to be nearly impossible), it will be very difficult to exactly match the data. Nevertheless, the present simulations have been able to reproduce nearly all the dynamical features observed in the experiments and also provided a new capability that can be utilized (at least in an idealized manner) to study such devices. Such a capability can be very useful for optimizing the final design of the micro-engine. Figures 2.1-11 through 2.1-14 show the subgrid kinetic energy and temperature at ignition and injection phases respectively. It can be seen that in both phases there is a significant amount of subgrid kinetic energy in the domain. Especially during injection, significant fluctuations are occurring in the high shear region of the injected jet. Spanwise views show that there is also significant three-

dimensionality in the domain suggesting that for this configuration (which involves an angled, high-speed injection), full 3D simulations are necessary to understand the dynamics of the mixing and combustion process.

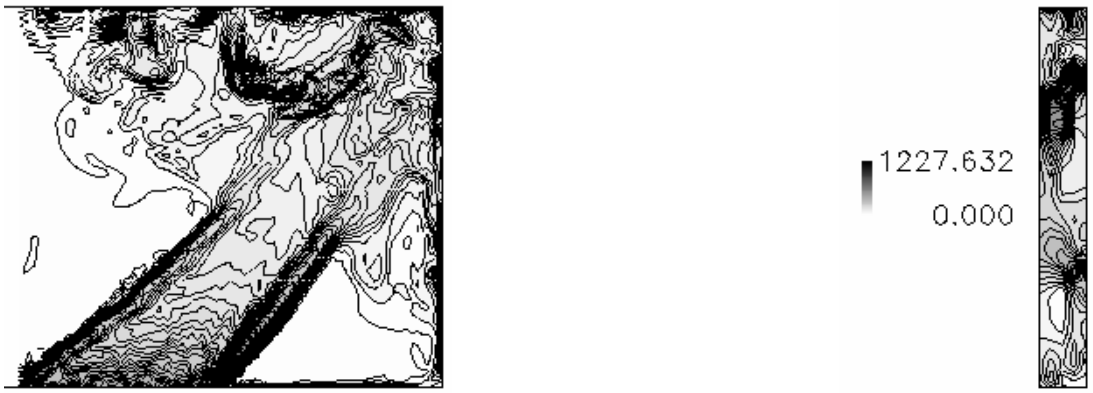

(a) (b)

Figure 2.1-11. *Kinetic energy during injection phase. (a) Planform; (b)Spanwise*

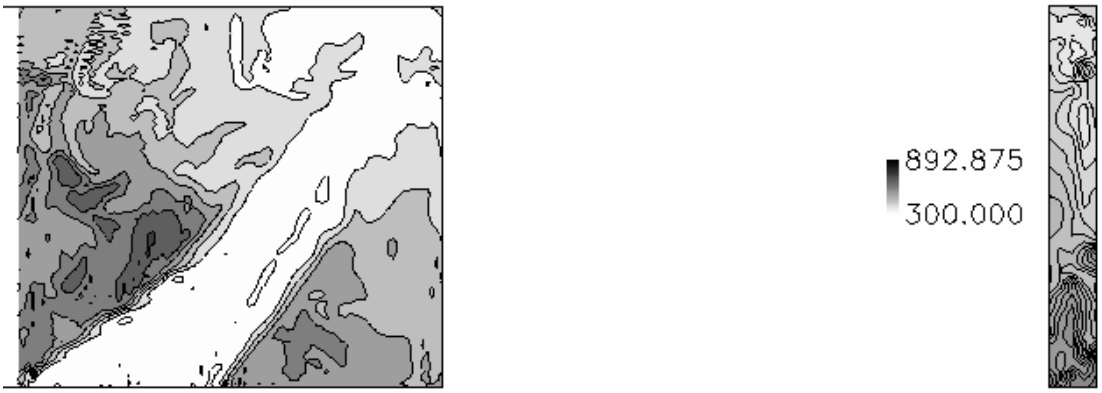

(a) (b)

Figure 2.1-12. *Temperature during injection phase. (a) Planform; (b)Spanwise*

(a) (b)

Figure 2.1-13. *Kinetic energy during ignition phase. (a) Planform; (b)Spanwise*

(a) (b)

Figure 2.1-14. *Temperature during ignition phase. (a) Planform; (b)Spanwise*

Finally, the experimental frequency is close to 32 Hertz while either of the numerical solutions is about 43 Hertz. According to Zinn et al.[4], a free piston device in the frequency range 25-50 Hertz will produce about 20 W electrical power. This is within the design goal of this project.

Conclusions

LES methodology has been developed to simulate combustion process in a free piston micro-engine. Simulations have been carried out for various design configurations in order to understand the dynamics of the combustion process in high aspect ratio combustors. The simulation results have been used to identify critical design issues and to provide guideline for the manufacture of this engine. These studies form the first such reported application of LES to hardware design and provide confidence on the ability of LES predictions. Comparison of the LES predictions with available data show reasonable agreement. In particular, the dynamics of

sustained oscillation has been captured well although there are some differences in the actual values. However, as noted above, there are many uncertainties in the experimental device that cannot be quantified and hence, cannot be modeled properly. Nevertheless, the LES model has shown its potential for addressing these flows in a more cost-effective manner and therefore, may become an important tool in the design of micro-engines in the near future.

Future studies of this micro-engine will address system parameters that are critical for optimizing the performance of the engine. Heat conduction through the wall will be included to model more accurately the heat transfer effect. The impact of injection strategy (orientation, location, port size, etc.) will also be addressed. Finally, further effort will be directed towards determining a model to include heat losses in a more accurate manner.

References:

1. Achten, A.J.P., "A review of free piston engine concepts", ASME paper 941776
2. Clark, N. N. and Famouri, P., "Modeling and development of a linear engine", ASME paper 98-ICE-95
3. Waitz, I. A., "Combustors for micro-gas turbine engines", Journal of Fluids Engineering, Vol. 120, No.1, 1998, pp. 109-117
4. Zinn, B. T., Glezer, A., and Allen, M. G., "Model and subcomponent development for a pulse-combustion-driven microgenerator", Tech.rep., Sept.1999, Report to DARPA/ARO
5. Tabaczynski, R. J., "Turbulence and turbulent combustion in spark-ignition engines", Prog. Energy Combust. Sci., Vol. 2, 1976, pp. 143-165
6. S. Menon and W. –H. Jou, "Combustion Science and Technology", volume-75, pp. 53-72, 1991.
7. T. M. Smith and S. Menon, "Combustion Science and Technology", volume-119(1-6), pp. 77-106, 1996.
8. Kirtas, M., and Menon, S., "Simulation of combustion driven micro-engine", AIAA 2001-0944
9. Paul, R. N., Kapoor, R., Kim, J.H., and Menon, S., "Simulation of Combustion-Driven Micro Power Generator", WIP poster accepted for the presentation at the 28th Symposium (International) on Combustion, will be held in August 2000.
10. Menon, S., and Paul, R. N., " Combustion Dynamics in a Compact Power Generator" Presented at the 8th Conference (International) on Numerical Combustion, Amelia Island, Florida, March 5-8, 2000.
11. S. Menon and W. –H. Jou, "Combustion Science and Technology", volume-75, pp. 53-72, 1991.T. M. Smith and S. Menon, "Combustion Science and Technology", volume-119(1-6), pp. 77-106, 1996.
12. Paul, R. N., Kapoor, R., Kim, J.H., and Menon, S., "Simulation of Combustion-Driven Micro Power Generator", WIP poster accepted for the presentation at the 28th Symposium (International) on Combustion, will be held in August 2000.
13. Menon, S., and Paul, R. N., " Combustion Dynamics in a Compact Power Generator" Presented at the 8th Conference (International) on Numerical Combustion, Amelia Island, Florida, March 5-8, 2000.

2.2. LES EFFORT FOR THE LABORATORY CONFIGURATION

Piston Motion Algorithm

The piston motion is determined by the acceleration as a result of the force acting on the piston. For the dual combustor case, the net force is the difference of the pressure in the chambers. For the spring forced motion case, spring force replaces one of the chambers. Hence

$$\ddot{x} = \frac{A}{m}(p_1 - p_2) \qquad (1)$$

where A is the piston cross sectional area, m is the piston mass and subscripts "1" and "2" refer to combustors. The computations usually start from rest at top dead center (TDC). For piston kinematics, position x is measured from the ignition wall.

In the present study, piston motion is handled by a Cartesian cut-cell approach. This method is particularly helpful for moving boundary problems on a fixed Cartesian grid system. The method, adapted for the present model, works as follows: at each time step, the displacement of the piston is determined based on the expression above and the vector of conserved variables (time dependent terms in LES equations) is computed according to the algorithm described in Yang et all.[16]. In this method, pressure on the moving wall is computed as a solution of Riemann problem. Consider Figure 2.2-1, where a cut cell (the first cell adjacent to the piston), piston surface and a ghost cell is shown. Subscript "s" is for surface values of the flow variables as determined by the piston motion. Depending on the actual piston (moving surface) velocity u_S, there can be two situations:

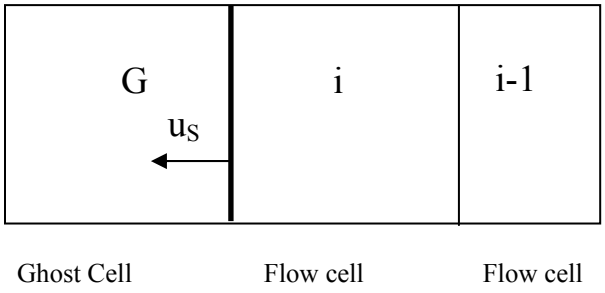

***Figure 2.2-1**. Computation of surface pressure*

If $u_s > u_f$, the pressure on the wall can be determined from the relation

$$\frac{p_s}{p_f} = \left(1 - \frac{\gamma - 1}{2}\frac{u_s - u_f}{c_f}\right)^{2\gamma/(\gamma-1)} \qquad (2)$$

In this case, both waves (left and right) from the surface are rarefaction waves. However, if $u_s \le u_f$, then the waves moving right and left are both shock waves. Thus normal shock relations are used to obtain the pressure on the surface

$$\frac{p_s}{p_f} = 1 + \frac{(u_f - u_s)^2}{2C_f^2} + \frac{(u_f - u_s)^2}{2C_f^2}\sqrt{\frac{8\gamma}{\gamma+1}\frac{C_f^2}{(u_f - u_s)^2} + 1} \qquad (3)$$

where $C_f = 2p_f/(\gamma+1)\rho_f$ and ρ_f is the extrapolated flow density near the surface. The subscript "f" is for the reconstructed cut cell face values at the solid boundary. The computation of these values depends on the information of gradients in the flow cells. To facilitate this process, we first apply boundary conditions on the surface by the ghost cell principle where ghost cell (G) values are computed by the reflection of the same variables in the flow cell(F) as:

$$\rho_G = \rho_i, \quad p_G = p_i, \quad u_G = 2u_S - u_i \qquad (4)$$

The cell face values of the flow variables are computed after gradients inside the cell are determined. The value of any variable U in the cell is

$$U(x) = U_i + \vec{r} \cdot \nabla U_i \qquad (5)$$

where $\vec{r}$ is the position vector measured from the cell center and U_i is the value at cell center. Hence, this formula find the value of any variable in the same cell depending on the distance from the center. The gradient vector ∇U_i has three components, U_x, U_y, U_z, but in the present study grid motion is in one space direction only(x direction) and gradients only in that direction are required. Hence,

$$U_x = \Gamma(U_G - U_i, U_i - U_{i-1}) \qquad (6)$$

where the Γ is the Van Leer limiter defined by

$$\Gamma(a,b) = \frac{a|b| + |a|b}{|a| + |b|} \qquad (7)$$

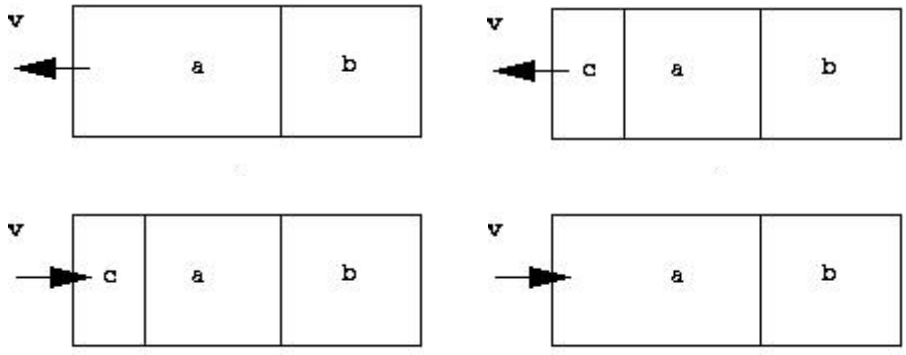

Figure 2.2--2 *Cell creation (top row) and merging (bottom row) diagram showing cells before (left) and after (right) the procedure. Arrows show the direction of piston motion, with v being the velocity of the surface.*

From these equations the flow velocity, density and pressure required in solid surface pressure computation can be determined. Knowing pressure and velocity on the moving boundary, we can then compute fluxes on the boundaries exactly. During piston motion the cell adjacent to the moving surface will change in volume (others do not change because they are treated on a fixed grid). Hence, to maintain accuracy and stability, maximum and minimum cell volumes are specified as $V_{min}=0.55V_{ref}$ and $V_{max}=1.55V_{ref}$ where V_{ref} is the volume of the original cell before the piston moves. As the volume increases (or decreases) with respect to the reference value, volume limitations are enforced through cell merging and cell creation. This is shown in Figure 2.2-2. A second order accurate interpolation scheme is used to compute properties in the newly created cells [16].

Results and Discussion

The ultimate concept of the power generator, shown schematically in Figure 2.2-3 consists of a free piston that is set into sustained oscillation by out-of-phase heat release in two opposed high AR combustors. This device is placed inside a permanent magnetic coil where the motion of the piston leads to electric power generation. The present research initially explored various designs experimentally and numerically. Since most of the combustion takes place in near constant volume, initial work concentrated on ignition and flame propagation in high AR chambers (with spanwise dimensions of 12 mm, 6.35 mm and 3.125 mm) with no moving parts. Heat transfer through and radical removal at the walls were identified both experimentally and numerically as a major cause for the limited pressure rise following combustion in the chamber [17].

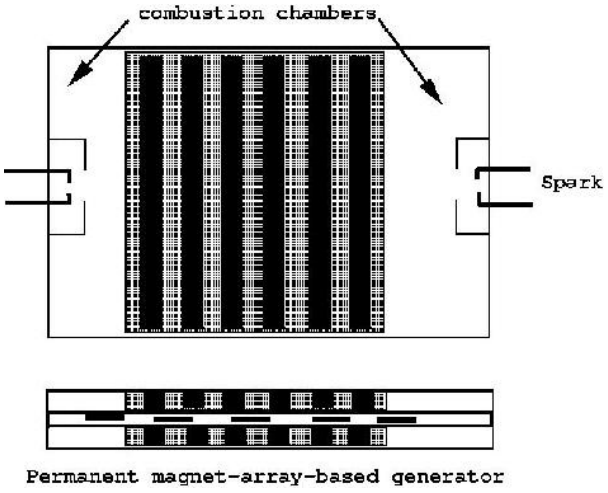

Figure 2.2-3*. The dual-combustor micro-engine with magnetic array*

To determine the impact of wall heat transfer, 2D and 3D simulations were carried out using adiabatic and unsteady heat flux at the wall using a constant volume combustor. In this case, the combustor volume was 4225 (50x13x6.5) mm^3 and a resolution of 100x60 and 100x60x10 were used for 2D and 3D respectively. Figure 2.2-4 summarizes the results of this study.

It can be seen that both 2D and 3D calculations reproduce the pressure rise with reasonable agreement. Furthermore, the effect of wall heat transfer is dramatic and results in a significant

drop in the peak pressure. This is an important issue for the design of this device since the pressure rise directly translates into the motion of the piston that in turn determines the power output from this device.

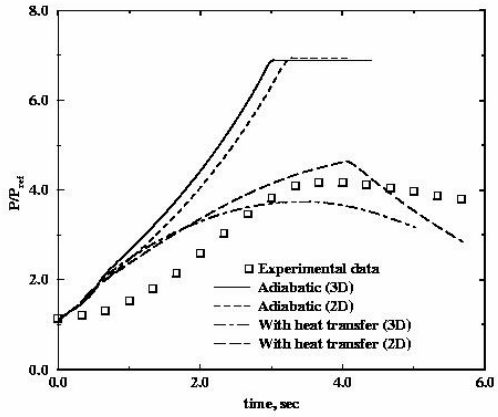

Figure 2.2-4*. Effect of heat transfer on the peak pressure in a constant volume combustor*

Thus, for an optimal design, reduction in wall heat transfer should lead in a more efficient design. However, practical manufacturing problems and the types of material available for MEMS fabrication may place an upper limit on the control of the amount of heat transfer through the walls. This implies that wall heat transfer must be included in all modeling studies. Ideally, for proper modeling, the heat conduction problem through the physical walls must be solved along with the LES flow problem in the combustor. Although comparison with data shows reasonable agreement for the heat transfer case, there are some discrepancies especially in the initial stages. This is related to the differences in the ignition process used in the experiment and in the model. In the experiments, multiple spark sources were employed whereas in the simulation a small volume in the domain was preheated. Thus, the initial flame kernel formation and its growth are quite different. Numerically, it is very difficult to mimic the spark ignition process. Furthermore, there could be other reasons that could result in the observed differences, for example, the use of global chemistry in the model, the effect of flame growth and quenching near the walls that is not modeled.

Dual Combustor Micro-Engine

Four different configurations were studied. Figure.5 shows one of the engine configurations used for LES simulations. Different versions of this device were also investigated for parametric studies [18]. Figure.6 shows these configurations. They differ primarily in the location of the inflow and outflow ports.

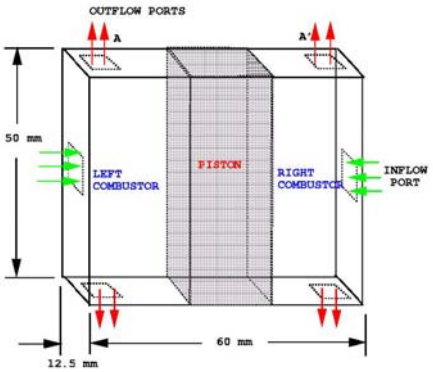

***Figure 2.2-5**. Schematic of a dual combustor model used for LES.*

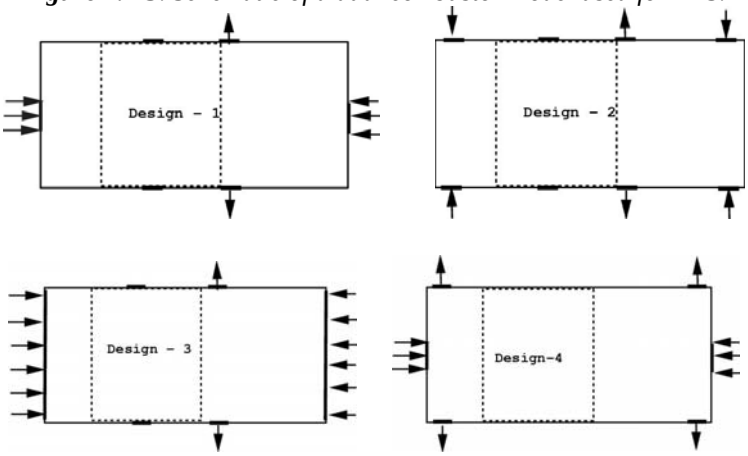

***Figure 2.2-6**. Schematics of various inlet (arrows in) and exhaust (arrows out) port configurations. Numbers (1-4) refer to design cases. Ports are valved by piston.*

The numerical simulation results showed that some of the designs had a fundamental flaw, namely that the reactant concentration in the chamber could not be increased to a level sufficient to sustain combustion. The concentration levels in each of these combustors are given in Figure 2.2-7 which shows the reactant concentration reached during the injection phase and before the outflow is opened. Ideally, the concentration should reach unity as quickly as possible. It can be seen that Designs 3 and 4 were effective in reaching this goal while Designs 1 and 2 failed to achieve high reactant concentration in the chamber before ignition. As a result, the Designs 1 and 2 does not show a sustained oscillation.

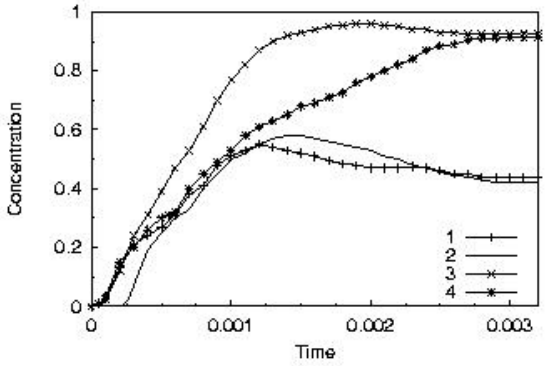

***Figure 2.2-7**. Predicted variations in maximum percentage fresh reactants in combustion chamber during each cycle with time over many cycles. Numbers (1-4) in the inset refer to port configurations in Figure 2.2-6.*

To contrast failing designs with successful ones, the flow field from each group was analyzed. Representative velocity vector fields for Design-1 and for Design-4 (which was successful) are shown in Figure 2.2-8. It was determined that in this case, some of the burnt products gets trapped in the combustor and affects the inflow of the reactants. In fact, due to this trapped products, some of the reactants escape through the outflow port before ignition. Note that, for the failed Design-1 case, burned products are trapped in the top and bottom corners (marked by symbol B) and some of the reactants (marked by a symbol R) actually escape through the outflow port before it is closed. In contrast, Design-4 due to the location of the outflow port allows all the burned products to exit while the injected reactant is still filling the chamber.

Simulations such as this are quite useful in obtaining quick answers to the modifications to the design since construction of this device would have taken a long time. Furthermore, the above studies were also conducted using both 2D and 3D (not shown here) codes to see if there is any similarity in the flow field. It was determined from the numerical studies that 2D and 3D simulations reproduce very similar process and the predicted pressure amplitude and frequency were very close. This is important since 2D simulations are computationally very inexpensive and therefore, a large number of parametric simulations can be carried out quickly in order to obtain some quick answers. On the other hand, for a more realistic combustion process, the effect of small-scale turbulence (which is 3D) needs to be included. Therefore, eventually, full 3D simulations are necessary to investigate the final design.

Results shows that inlet/outlet port locations, and thus injection and scavenging strategies all impact the performance of the device

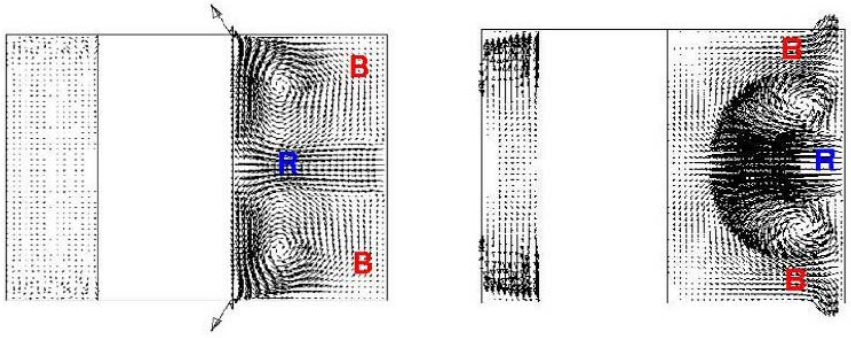

Figure 2.2-8. *Velocity vector field for designs 1(left) and 4(right). Trapped burnt products (marked by letter B) from the previous cycle in Design-1 limits the magnitude of the reactant (marked by letter R) concentration reached at the end of the injection period.*

Single Combustor Micro-Engine

The above represents one of the few examples where LES has played a direct role in engineering design by providing guidelines for design improvements. Because of the difficulty of carrying out detailed, in-situ measurements, LES may prove to be the only cost-effective means for design optimization before actual fabrication. The present effort is, therefore, directed towards developing and establishing such a design capability.

The earlier study established the numerical methodology and demonstrated its ability to capture some of the dynamics of the flow field. The dual-combustor studies also showed how a successful design could be achieved. However, designs such as Design-4 required additional mechanism to open and close the ports (since they were located further from the piston). From an experimental point of view, a simpler design is preferred and this resulted in the development of the single-combustor design, shown in Figure 2.2-9.

This device consists of a single combustor-spring configuration. A piston made of cast iron moves in a flat steel cylinder with optical access through Pyrex windows. The piston motion valves the inlet and exhaust ports and also triggers an ignition spark (generated by an automotive ignition circuit). To limit leaks, a dynamic wiper seal made of a double layer of Teflon-coated fiberglass is used along the longer sides.

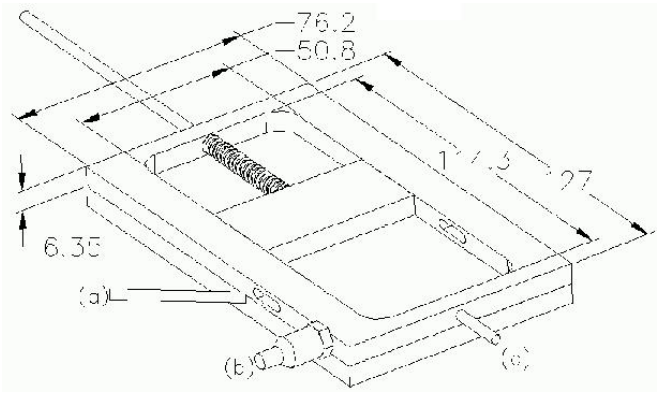

Figure 2.2-9. *Spring forced combustor schematic. All dimensions are in mm. Also shown are the injection tube (a), pressure transducer (b) and the spark plug (c).*

A split piston (whose two halves are pushed against the side walls by a spring) seals along the side walls while leaving a gap in its center, which is itself sealed by the dynamic frontal seal. Sealing is further improved using Diester synthetic oil.

To start the engine, the piston is pulled back against the spring using a handle. This action opens the inlet and exhaust ports, and allows the combustion chamber to fill with fresh propane-air mixture, which is injected at an angle. When the handle is released, the spring propels the piston forward. Once the ports close, the mixture is compressed and then ignited by the spark. The subsequent pressure increase decelerates and eventually reverses the piston's motion. Eventually, the ports re-open, the combustion products exhaust and fresh reactants enter the chamber. The spring is compressed until the piston motion is reversed and the cycle restarts.

Pressure is measured using an Endevco 8541-100 piezo-resistive transducer and piston position is recorded with a Micro-Epsilon non-contact optical displacement monitor. These two measurements (under load) are combined to determine the mechanical power generated by the device using a P-V diagram. Optimum operating conditions are determined by monitoring a real time plot of P-V (with LABView) while changing spark timing, mixture ratio, and injection direction to maximize mechanical power output. Electrical power output is determined by connecting a voice coil generator subwoofer without the cone, run as a generator to the piston and measuring the resultant voltage across a known resistance. Wall and exhaust flow

temperatures are measured with type K thermocouples. The flame is observed directly and by shadowgraphs using a Kodak Ektapro digital intensified camera at 3,000 fps. Shadowgraphy is used to visualize the flow by recording the motion of the density gradients.

While the thickness of the combustor could be varied, most results were obtained for a thickness of 6.35 mm. Since the inflow conditions were not precisely known, some assumptions had to be made. Based on the mass flow rate, the velocity of the incoming jet was estimated to be 80 m/sec. However, no information on the level of turbulence in the inflow is available, although flow visualization did suggest significant turbulence. We, therefore, assumed 10% turbulent fluctuations at the inlet (although most of it rapidly decays once injection is complete).
The computational domain consists of three sub-domains: the main combustor and the two scavenging ports (one of the ports is also used for reactant injection into the combustor). The combustor is resolved using an uniform grid in each spatial direction and consists of 95x91x13 cells at TDC where the domain size is maximum. The scavenging ports are attached to the main body and extend six times the width of the port at full opening in +y and -y directions. A computational grid of 18x40x13 is used for each of these sub-domains. Stretching and contraction are applied to the grid distribution close to the outflow boundaries.

Flow Visualization

Figure 2.2-11 shows the subgrid kinetic energy and the instantaneous velocity vector field just before (a) and just after (b) inlet port closing. The plots clearly show the asymmetry of the flow field caused by the single fuel/air intake. It also shows the turbulent nature of the injection and the rapid decay of turbulence once the inflow has stopped. Similar inflow patterns were observed in the high-speed shadowgraph images (not shown here) of the injection phase, although the high mixing levels, evident from the computational results, impeded the observation of shadows of the flow after the ports closed. Figure 2.2-12 compares the flame propagation obtained experimentally and numerically at different instances during the burn part of the cycle. Although flame positions are established using different criteria (flame radiation versus temperature plot), the similarity between the flame patterns is striking. Traces of large-scale motion, left over from the flow pattern generated by the injection, are visible in the large-scale propagation pattern of the flame. The presence of the large-scale motion, which is usually not seen in conventional engines, is attributed to the relatively low pre-compression of this design and the high AR geometry. Small-scale turbulence is also present and evident by the wrinkled edges of the flame

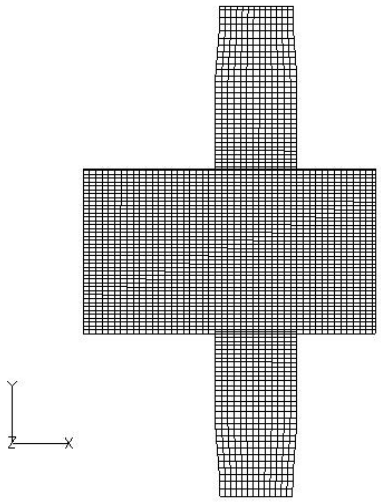

***Figure10**. Planform view of the computational grid used in the single combustor simulation. Every other grid point is shown. The grid is 95x91x13 for the middle domain. The scavenging ports have the same resolution except they have also contraction near the outflow boundaries. The basic structure shown above is simply translated in +z direction to obtain the actual 3D grid.*

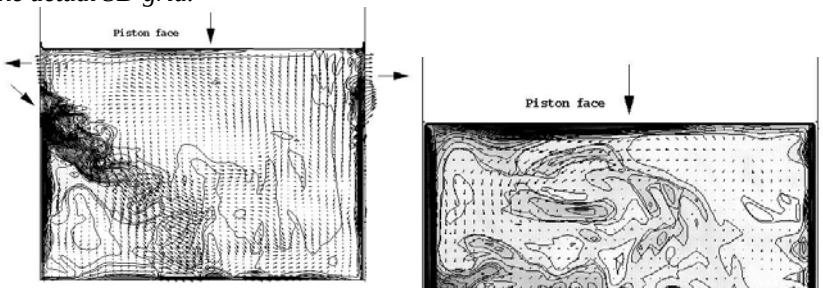

***Figure 2.2-11**. Contour plots of calculated subgrid kinetic energy superimposed on instantaneous velocity vector field just before (a) and just after (b) port closing. Outflow and inflow locations are shown by the arrows in the figures. Incoming jet has a velocity of 80 m/sec plus 7% subgrid turbulent kinetic energy fluctuations. Note the difference in gray scale legend*

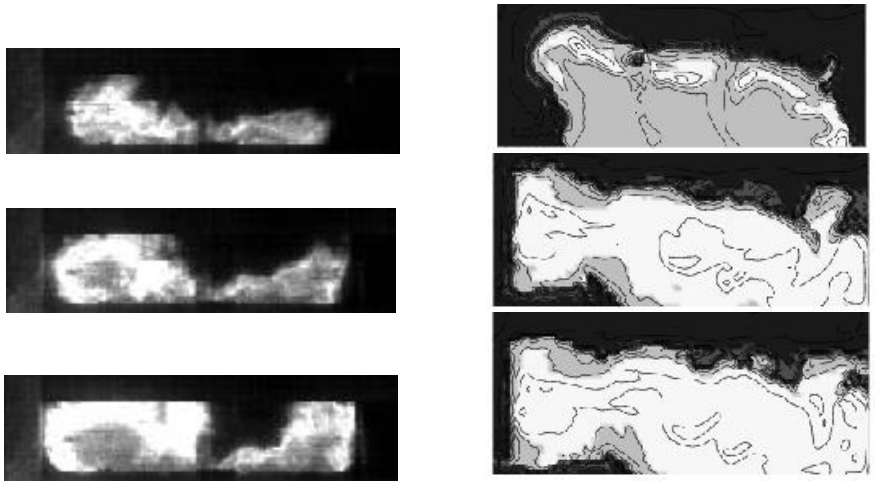

***Figure-12.** Comparison of flame propagation as indicated by radical radiation for experimental (left column) and temperature distribution for computational (right column) study. Images are 1/3 msec and 0.3 msec apart in left and right, respectively.*

Performance of the Micro-Engine

In the work presented here, the piston motion is determined by the algorithm described earlier. However, runs were carried out for selected conditions where measured displacement history of the piston was prescribed for the model. This was considered as a good test for the cartesian cut-cell method as applied in the present study. In Figure 2.2-13 the pressure signature in the chamber is shown for experimental results and both the LES. Although direct comparison is not possible or intended (due to differences in the ignition, kinetics model and leakage, as noted earlier), the general trends are in very good qualitative agreement. Both studies show that cyclic combustion with repeatable pressure peaks is achieved at a fixed frequency. However, the model over-predicts both frequency and amplitude by approximately 19% when the piston motion is calculated, pressure amplitude only when the piston motion is prescribed. Estimates of the mass losses around the piston suggest that about half of the reduction in pressure amplitude is due to mass losses with the remainder caused by neglecting wall quenching.

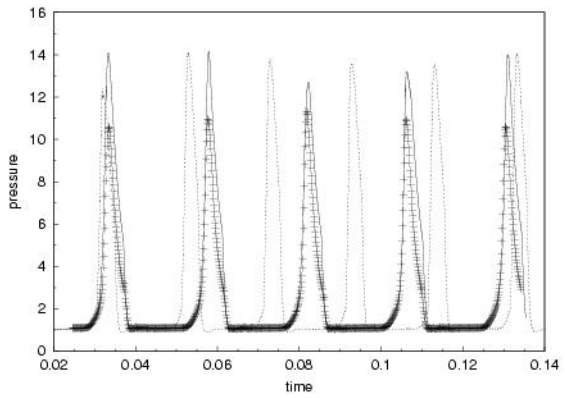

Figure 2.2-13. *Pressure-time histories for experiment and the present numerical simulation. Pressure is non-dimensionalized by ambient pressure. Time is in seconds.*

These discrepancies are understandable considering the approximations used in the model. To compensate for these assumptions a spring constant (2000 N/m), nearly twice that used in the experiments was used in the model. This was based on earlier findings [18] that suggest that adjusting the spring constant can, at least partially, compensate for neglecting mass loss, spark ignition, and kernel growth, and using simple kinetics, all of which impact frequency and amplitude. Future studies will include more detailed kinetics (needed to allow for local extinction/re-ignition and near-wall quenching in high AR combustors) using In-Situ Adaptive Tabulation [19] to relax some of these approximations.

Closer inspection of Figure 2.2-13 shows how the pressure develops through the ignition and scavenging phases. Since no mass loss is included, the predicted peak pressure is higher than that measured in spite of the adjusted spring constant (see above). Also, the initial pressure rises faster in the simulation. The pressure decay during the final stages of the exhaust stroke is also faster. In the experiments, pressure decreases almost linearly, showing the effects of both mass loss and blowout through the port where as, in LES, the pressure drops more rapidly once the port opens.

The performance of the engine can be quantified using a pressure-volume diagram, as shown in Figure 2.2-14, where integrating the area in the cycle indicates the mechanical work produced. Both, when the piston motion is determined by the model and when it is prescribed, the predicted work output is larger than that measured experimentally. This could be due not only to mass losses that are not modeled, but also to the filtered reaction rate and the simple EBU model that provided closure. Future studies will include a subgrid mixing and combustion model [11]. Furthermore, more detailed kinetics will allow prediction of extinction and near-wall quenching. Nevertheless, the current prediction do show that the qualitative behavior and trends of cyclic combustion are in good agreement with observations.

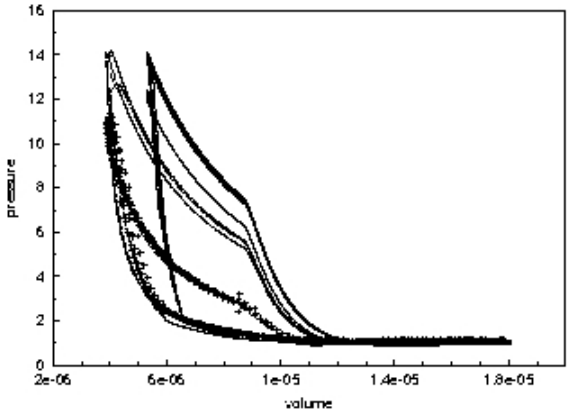

Figure-14. *P-V diagram showing measured (symbol) and predicted work generated per cycle. Work produced is over-predicted in both cases for both model determined (solid line) and prescribed piston motion (dashed line) since mass losses and wall quenching are neglected.*

Temperatures were measured on the glass side-walls of the combustor and in its exhaust. Because of the relatively high frequency of heat release and the large mass of the wall, the wall temperature reaches a steady state value. The exhaust temperatures were averaged over a number of cycles. Exterior wall temperatures were measured at the center of that part of the wall exposed to the combustion chamber when the piston has reached TDC. Additional temperatures were measured 2 cm in the +y and -y directions. The wall temperature at the center was measured to be 418 K while those off center were about 35 degrees lower. The predicted wall temperatures were approximately 65 degrees higher than those measured, with temperatures near the exhaust being about 15 degrees higher than those near the inlet. The predicted exhaust temperatures were closer to those measured, 433 K vs. 407 K, respectively. The predicted temperatures are probably too high because wall quenching is not accounted for in the present model. That also explains why this effect is more pronounced at the wall than in the exhaust.

Conclusions

A LES based design tool for predicting the performance of small, high aspect ratio combustors of rectangular cross-section was developed. Its predictions were then compared with experimental result obtained in a corresponding combustion chamber, which forms part of miniature power generator. The model predicted the periodic motion of the piston and the resulting pressure variations in the chamber, although the frequency and amplitude of the pressure fluctuations were over-predicted by about 20%. Half of this overestimate is caused by neglected mass losses past the piston while the other half is due to the fact that wall quenching is not included in the

model. The latter also causes the predicted temperature at the wall, and, to a lesser extent, in the exhaust, to be somewhat high. Neglecting mass losses, quenching and friction also caused the model to overestimate the power generated.

References

1. Waitz, I.A., Gauba, G., and Tzeng, Y-S., Journal of Fluids Engineering,120:109, (1998).
2. Achten, A.J.P., ASME Paper 941776, 1994
3. Goldsborough, S.S., and Blarigan, P.V., SAE Paper 1999-01-0619, 1999
4. Clark, N.N., and Famouri, P., ASME Paper 98-ICE-95, 1998
5. Kim, W.-W., Menon, S., and Mongia, H.C., Combustion Science and Technology, 143:25, 1999
6. Deardorf, J. W., Journal of Fluid Mechanics, Vol. 41, Part 2, pp. 453-480, 1970.
7. Ferziger, J. H., AIAA Journal, Vol.15, No. 9, pp. 24-37, 1977.
8. Piomelli, U., Cabot, W. H., Moin, P., and Lee, S., Physics of Fluids A, Vol. 3, No. 7, pp. 1766-1771, 1991.
9. Ghosal, S., and Moin, P. Journal of Computational Physics, Vol. 118, No. 1, pp. 24-37, 1995.
10. Erlebacher, G., Hussaini, M. Y., Speziale, C. G., and Zang, T. A., ICASE Report No. 87-20, 1990.
11. Menon, S., Int. J Engine Research, 1:209, 2000
12. Westbrook, C.K., and Dryer, F.L., Combustion Science and Technology, 27:31, 1981
13. Fureby, C., and Moller, S.I., AIAA Journal, 33:2339, 1995
14. MacCormack, R.W., AIAA Paper 69-354, 1969
15. Poinsot, T. and Lele, S., Journal of Computational Physics, 101:104, 1992
16. Yang, G., Causon, D.M., and Ingram, D.M., AIAA Journal, 37:905, 1999
17. Faulkner, J., Scarborough D., and Jagoda, J., AIAA Paper 2000-0591, 2000.
18. Kirtas, M., and Menon, S., AIAA Paper 2001-0944, 2001
19. Sankaran, V., and Menon, S., Proc. Comb. Inst., 28:203, 2000

3. Magnetic Generator Topology Development

Professor David Taylor

One possible configuration for a permanent-magnet type of microgenerator has been investigated using finite element analysis. The motivations for this investigation are: (i) to provide the data needed to develop an accurate analytical model of the microgenerator based on magnetic circuit analysis; (ii) to help quantify the relationships between the various design parameters and microgenerator performance; and (iii) to build the foundation for future work on optimization of the microgenerator design. The cross-sectional geometry of the present configuration is shown in Figure 3-1. Only one fundamental section of the microgenerator is displayed, due to symmetry with respect to the centerline of the piston and to the repetitions of the "magnet (N/S) – coil (CCW) – magnet (S/N) – coil (CW)" structure. The complete microgenerator includes an equal integer number of these fundamental sections both above and below the piston centerline. Computational efficiency has been enhanced by exploiting these properties of symmetry and periodicity.

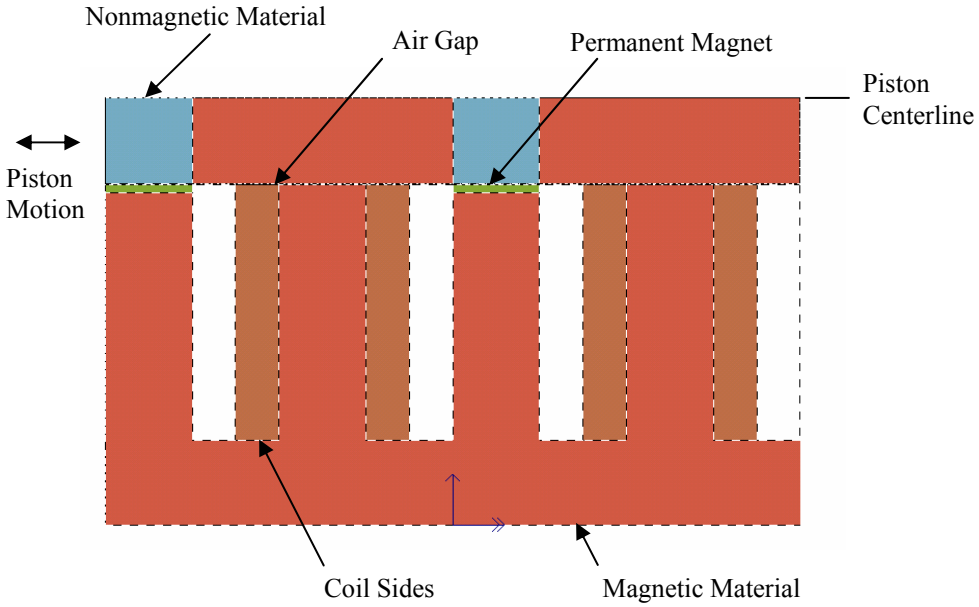

Figure 3-1. *Geometry of repeating section.*

As the piston moves, the nonmagnetic barriers of the piston redirect the permanent-magnet flux paths such that the flux linkages of the series-connected coils will be time varying. According to Faraday's Law, the voltage induced in the compound coil is equal to the time rate-of-change of its flux linkage. Hence, the open-circuit or no-load voltage generated will be the product of the spatial rate-of-change of flux linkage and the piston velocity. The first factor in this product is favorably influenced by the repeating occurrences of the fundamental section shown in Figure 3-1. When a load is connected, the resulting flow of current will develop a retarding force on the piston. The retarding force will generally consist of three components: reluctance force, cogging force and alignment force. The finite element models that have been developed predict both the induced voltage and the retarding force, and hence they are useful for design optimization.

As an example, consider the microgenerator described in terms of geometry and materials by Table 3-1. A 2D magnetostatic analysis using the finite element method has been performed. The no-load flux linkage computed by finite element methods is displayed in Figure 3-2. When multiplied by velocity, the spatial rate-of-change of this flux linkage plot yields the no-load induced voltage. The force components (at 1 A coil current or 20 A/mm^2) computed by finite element methods are shown in Figure 3-3. The alignment force has the shape of the no-load induced voltage with respect to piston position, and exhibits a spatial period of 4 mm. The reluctance and cogging forces exhibit a spatial period of 2 mm. For this set of design parameters, the reluctance force has the smallest magnitude and the alignment force has the largest magnitude.

Table 3-1. *Example Microgenerator Parameters.*

Frame	100 × 50 × 10 mm
Piston	61 × 50 × 2 mm
Stroke	32 mm
Poles	1 × 50 × 3 mm
Magnets	1 × 50 × 0.1 mm, SmCo
Slots	1 × 50 × 3 mm
Yokes	16 × 50 × 1 mm
Air gap	0.01 mm
Coils	30 turns/pole, AWG 30 copper

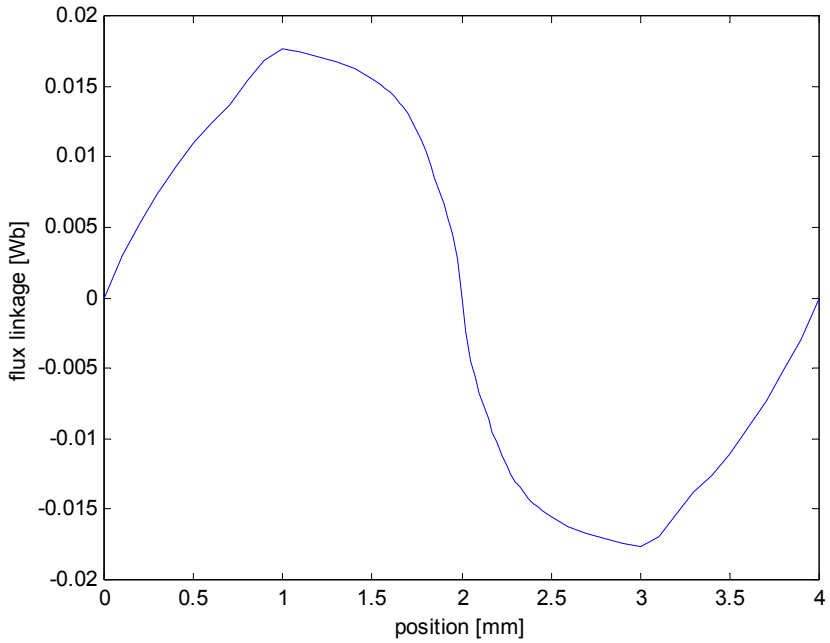

Figure 3-2. *No-load flux linkage.*

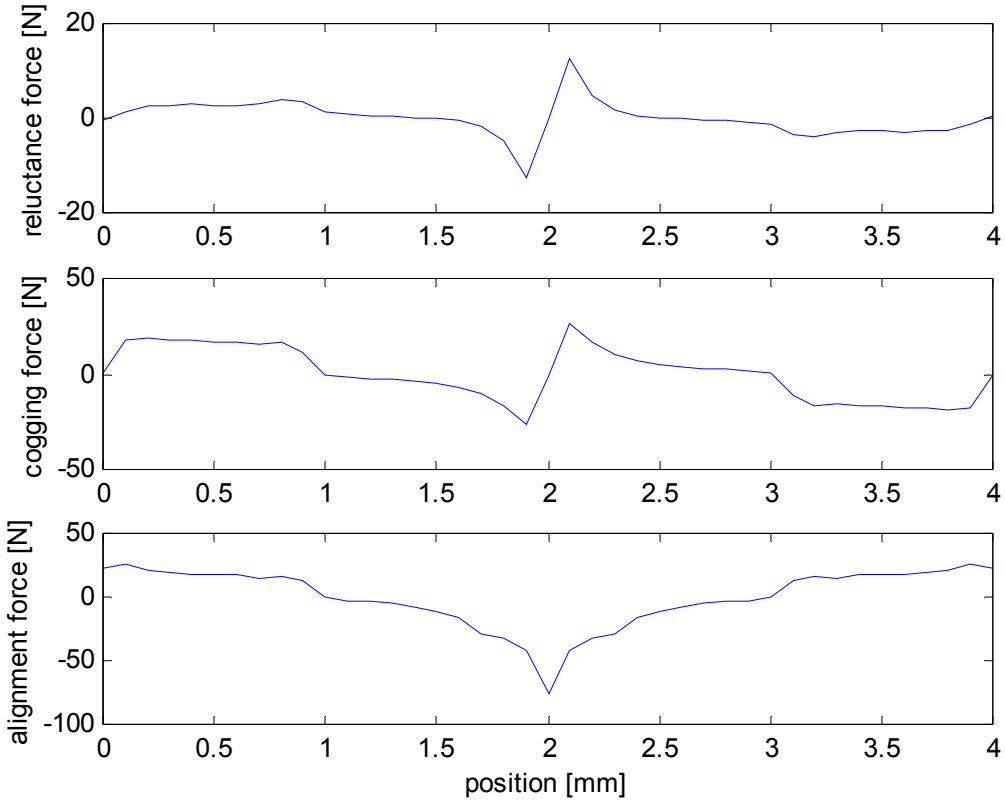

Figure 3-3. *Force components at 1 A coil current.*

The previously described finite element results were obtained by post-processing the magnetic field data presented visually in Figure 3-4. The shaded contour plots display flux density distribution at 1 A coil current for various piston positions throughout one electrical cycle, including the effects of permanent magnets, material nonlinearities, and leakage and fringing. Note that one electrical cycle corresponds to half the length of one fundamental section, which in this case is 4 mm, and hence there are 8 electrical cycles per stroke or 16 electrical cycles per mechanical cycle in this case. Figure 3-4 clearly shows the spatial variation of flux linkage with respect to piston motion.

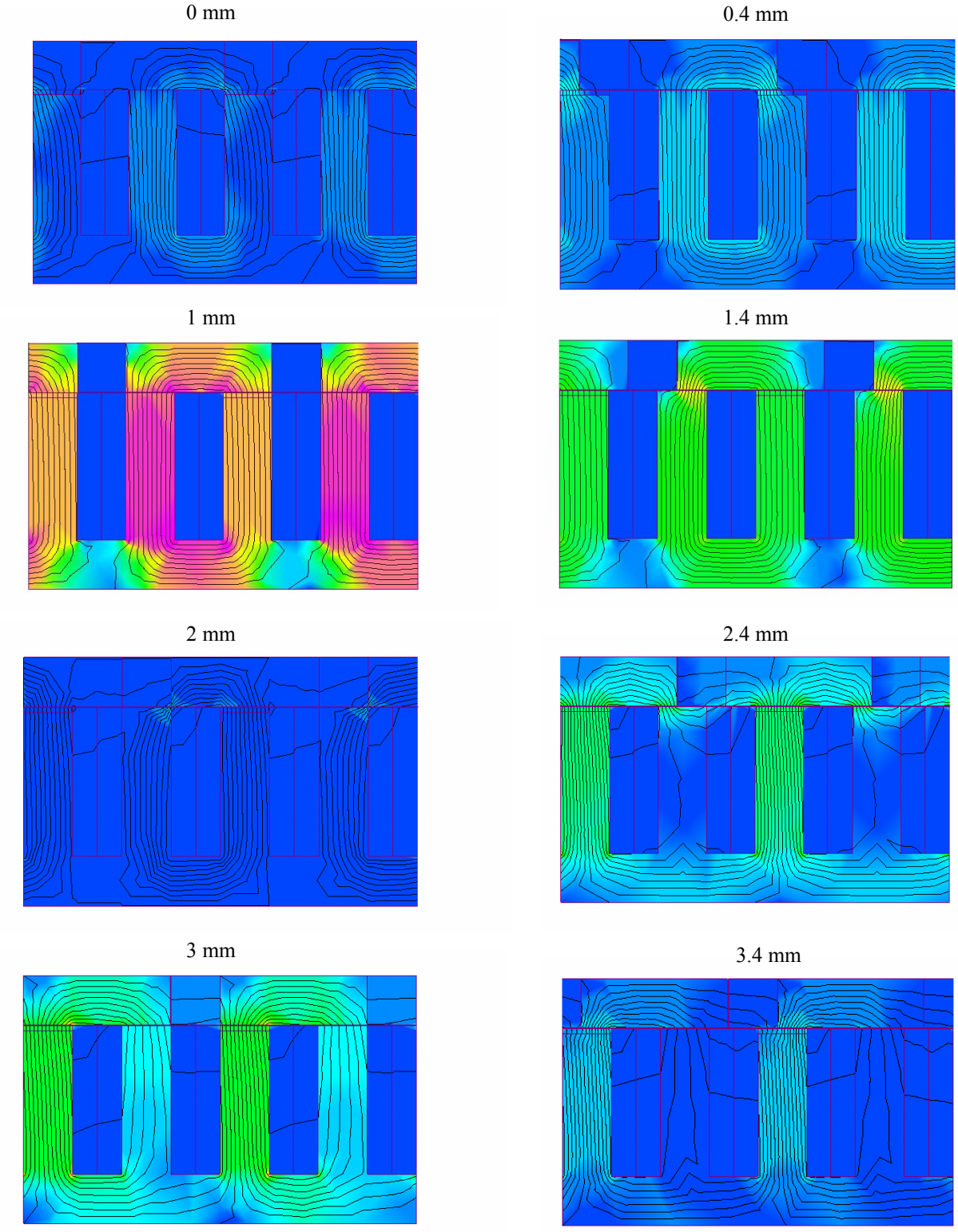

Figure 3-4. *Flux density at 1 A coil current for various piston positions.*

One practical disadvantage of the first-generation topology was the distribution of many small coils throughout the device. In the second-generation topology, many small coils are replaced by only a few larger coils that are centrally located at some convenient distance from the MEMS-scale permanent-magnet arrays and flux-directing fins of magnetic steel. A photograph of an experimental prototype based on the second-generation topology is shown in Figure 3-5.

Figure 3-5. *Second-generation experimental prototype microgenerator.*

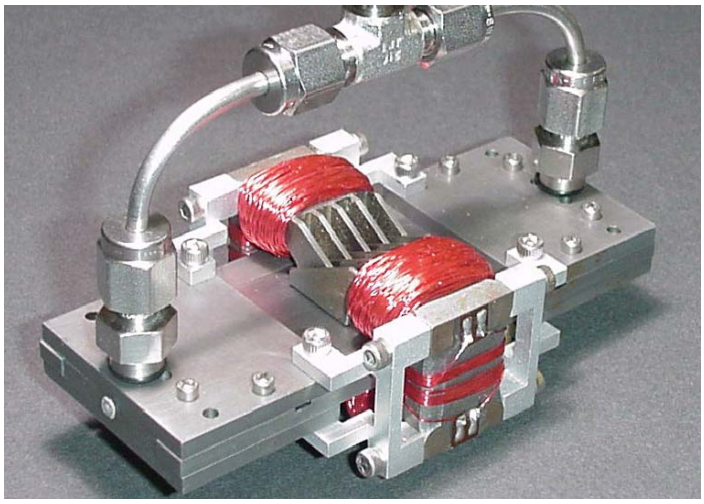

A microgenerator design procedure for the second-generation topology was developed using simplifying assumptions and magnetic circuit analysis concepts. The goal was to clearly expose the most basic design issues without the burden of complexity that comes from more accurate modeling techniques. The assumptions made are: constant piston velocity, sinusoidal air gap reluctance, infinite permeability for soft magnetic material, linear demagnetization for hard magnetic material, no leakage or fringing of flux, and room temperature operation. Future work will concern modifications to the design procedure consistent with relaxed assumptions.

The design procedure may be briefly described as follows. The maximum average power deliverable to a matched load and the piston velocity are first specified. Then the electric parameters (resistance, current, voltage) are selected using the elementary theory of maximum power transfer in (single frequency) sinusoidal steady state. Then the wire parameters are determined based on a specification of maximum allowable current density. Then the magnetic parameters are determined so as to establish a desired magnet operating range and to limit leakage flux, leading to a required product of number of magnets and number of turns. Finally, the coil dimensions are computed to be consistent with previously established parameters and a winding packing factor. The design procedure naturally involves choices of free parameters, and hence it does not uniquely determine a single candidate design for a given required maximum average power and piston velocity. Consequently, future work will consider strategies for making the best use of the design freedoms, in order to optimize some measure of performance.

One important issue that has recently been investigated is how to achieve maximum power transfer in a generating system that operates with reciprocating motion. The reciprocating-motion microgenerator may be modeled as an ideal independent voltage source in series with some impedance. The source voltage will be periodic but not sinusoidal, and the harmonic

content of this voltage will be significant, due to both the spatial harmonics of the permanent-magnet flux linkage and the temporal harmonics of the piston velocity. Moreover, the internal impedance of the microgenerator can exhibit frequency-dependent resistive and inductive components due to core losses (eddy currents and hysteresis). Consequently, the classical theory of maximum power transfer, which considers only sinusoidal operation, is truly inadequate in the present application. A new generalized theory for maximum power transfer is clearly needed, not only to help develop and verify good microgenerator design procedures, but also to enhance the utility of the microgenerator for future applications.

To this end, two network synthesis problems are presently under investigation. Consider the circuit diagrams in Figure 3-6. The circuit model of the microgenerator is connected to a designable load, in the first diagram, and to a specified load through a matching network, in the second diagram. The two synthesis problems of interest are as follows. *Problem 1*: Given the microgenerator with impedance $Z_G(s)$, find a passive load such that the average power received by the load is maximized. *Problem 2*: Given the microgenerator with impedance $Z_G(s)$ and the passive load with impedance $Z_L(s)$, find a passive and lossless matching network such that the average power received by $Z_L(s)$ is maximized. The first problem is relevant in assessment and testing, whereas the second problem is relevant in actual applications. Solutions to these problems require interpolation with positive-real rational functions, with interpolation points on the imaginary axis. Thus the boundary Nevanlinna Pick interpolation theory may be applied, and the actual computations have been programmed using state-space techniques.

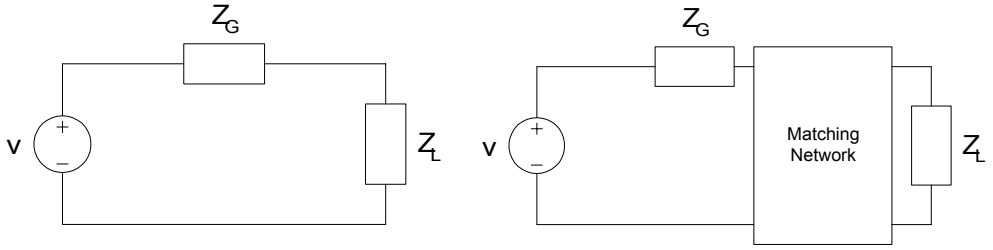

Figure 3-6. *Two problems of maximum power transfer with a multi-frequency source.*

An experimental prototype microgenerator (the one shown in Figure 3-5) was constructed to enable comparison of measurement data to performance predictions. Since the air gap length of the experimental device is quite large in comparison to magnet-to-magnet spacing and fin spacing, any simple application of magnetic circuit analysis will be totally unreliable (and hence the previously mentioned simple design procedure does not apply in this case). The significant level of leakage flux in this first experimental prototype requires the finite element analysis technique for accurate modeling.

A three-dimensional finite element model of the experimental prototype was created using matching dimensions and estimated material properties, as shown in Figure 3-7. Magnetostatic analysis was used to obtain the flux linkage due to the permanent magnets as a function of piston position, as shown in Figure 3-8. As expected, the flux linkage values computed using finite element analysis were much smaller than those computed using simple magnetic circuit analysis, due to high leakage flux levels.

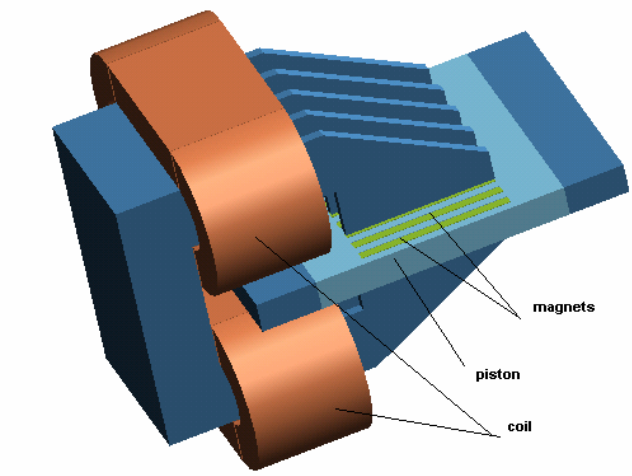

Figure 3-7. *Finite element model of prototype microgenerator.*

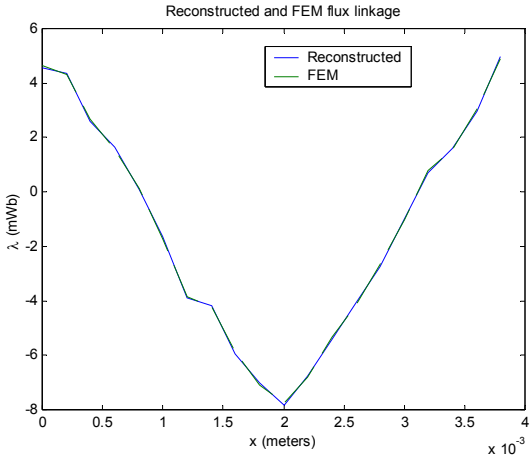

Figure 3-8*. Flux linkage due to PM as a function of piston position.*

The measured open-circuit voltage of the prototype microgenerator for a particular reciprocating piston motion is shown in Figure 3-9. As expected, this voltage waveform is non-sinusoidal, with significant harmonic content. The frequency spectrum of this voltage waveform, shown in Figure 3-10, indicates that the transfer of average power to a load occurs at a number of distinct frequencies. Indeed, Figure 3-11 shows that four frequencies (rather than just one) contribute significantly to the average power that could be received by an ideally matched load impedance. The network synthesis problems mentioned previously are clearly relevant for this type of generating system.

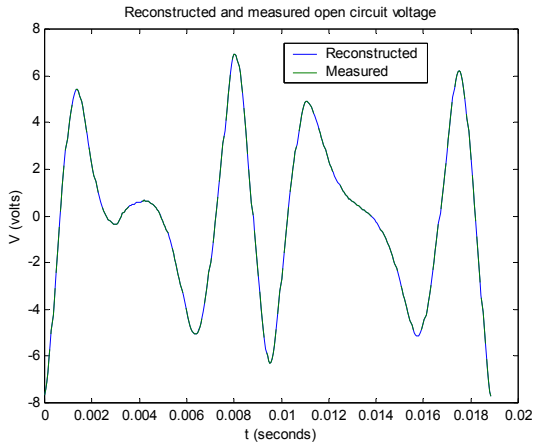

Figure 3-9. *Measured open-circuit voltage.*

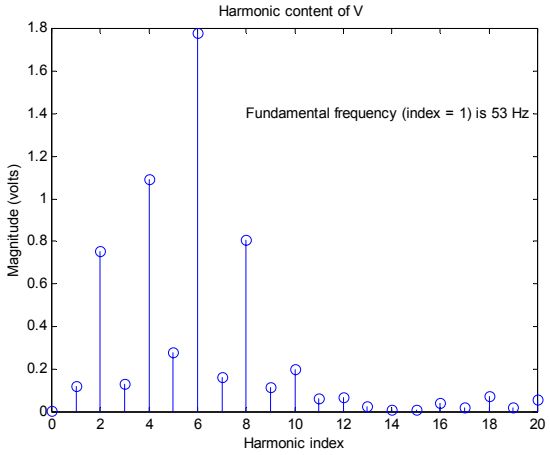

Figure 3-10. *Spectral decomposition of open-circuit voltage.*

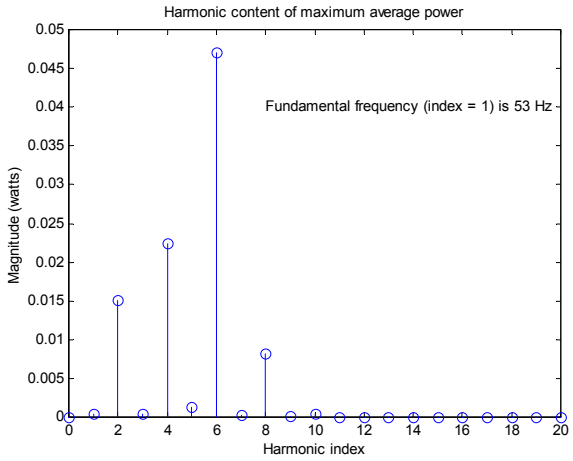

Figure 3-11. *Multi-frequency maximum power transfer.*

In conclusion, the finite element model of the prototype microgenerator yields performance predictions that are in general agreement with the experimental measurements. The

computed flux linkage predicts roughly the same open-circuit voltage as was measured, and the spectral analysis of the open-circuit voltage predicts roughly the same average power under load as was measured. Hence, the basic operating concept for the proposed microgenerator topology has been proven feasible. On the other hand, the multi-frequency maximum power transfer theory predicts that this first prototype microgenerator is only capable of supplying about 0.1 W of average power to an optimally matched load impedance at 1 m/s. This low power level is primarily due to a relatively large air gap length and the corresponding disadvantageous level of leakage flux. Future work will focus on design, fabrication and testing of similar microgenerator topologies but with more appropriate choice of air gap length.

As noted above, the research on linear motion electromechanical energy conversion shifted from permanent-magnet devices to variable-reluctance devices. Linear variable reluctance (LVR) machines are linear machines that exploit magnetic saliency in such a way that the reluctances of the flux paths will vary with displacement. Several different configurations are possible, but the one considered for this initial study is the three-phase configuration sketched in Figure 3-12. Each phase winding is a series connection of two concentrated coils placed on opposing poles of the two E-cores. The phases of this configuration are magnetically coupled, since the flux induced by exciting one phase necessarily links the turns of the other phases as it traverses closed paths through magnetic material. An interesting aspect of this configuration is that it combines features of "switched" and "synchronous" variable reluctance machines, and hence defies straightforward classification. Double saliency and concentrated windings are features normally associated with the "switched" variety, whereas strong magnetic coupling between phases is a feature normally associated with the "synchronous" variety.

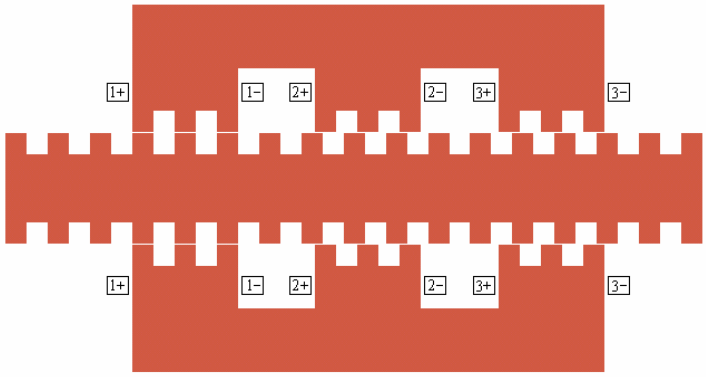

Figure 3-2 *LVR machine with magnetically coupled phases.*

The LVR machine has been characterized by both magnetic circuit analysis (MCA) and finite element analysis (FEA). MCA requires assumptions about flux path geometry but leads to simple and convenient equations that reveal the influence of air gap permeance on critical device characteristics. FEA uses spatial discretization to calculate the magnetic field with high accuracy, but it requires significantly more computation time and provides only numerical data. MCA and FEA are used to investigate the effect of tooth shape on inductance and force. Qualitative agreement between the two analysis methods has been demonstrated for low excitation levels. These comparative analyses should provide useful insights for future work on machine design and control design.

The LVR machine configuration of Figure 3-12 may be modeled using the magnetic circuit diagram of Figure 3-13. This magnetic circuit diagram is based on the following assumptions: the magnetic material is infinitely permeable; there is no leakage flux. Although such assumptions are not necessary, they simplify the analysis and lead to modeling equations that exhibit trends with maximum clarity.

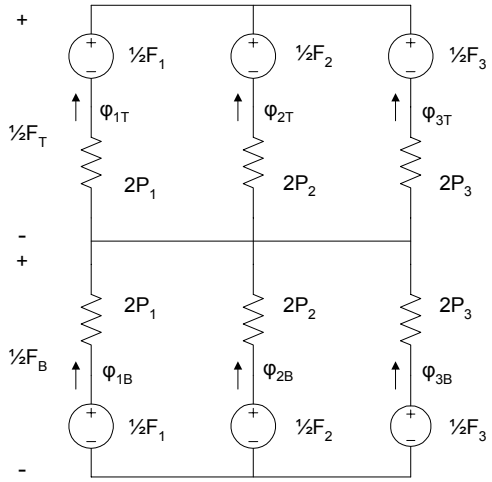

Figure 3-13. *Magnetic circuit model for LVR machine.*

According to Figures 3-12 and 3-13, the permeances of the air gap regions around the poles will determine how fluxes flow in response to phase currents. The permeance of an air gap region may be approximated by assuming that the flux in that region follows paths defined by straight lines and circular arcs. It follows that the permeance of that region is the sum of several flux tube permeances. The air gap permeances vary as a function of relative displacement. In fact, these permeances are periodic functions of displacement, with period equal to one tooth pitch and with pole-to-pole spatial shifts equal to one-third tooth pitch.

Once the air gap permeances are known, it is possible to determine the pole fluxes induced by phase currents. The magnetic model may be conveniently summarized by an inductance matrix. Explicit formulas have been obtained to relate the self and mutual inductances to air gap permeances. According to the theory of electromechanical energy conversion, the reluctance force is a quadratic function of phase current with scaling matrix equal to the spatial derivative of the inductance matrix. The magnetic coupling leads to a non-diagonal inductance matrix, so all possible products of phase currents are involved in the production of force.

The topology of Figure 3-13 assumes that all flux induced by a coil will cross the air gap. In reality, other so-called leakage paths for flux exist. As a first approximation, the topology of the magnetic circuit can be modified to include a constant leakage permeance in parallel with each mmf source. In that case, a leakage component is added to the self inductances but the mutual inductances are unchanged. Since this modification to the inductance matrix does not depend on displacement, force production is not influenced by this leakage effect.

MCA is computationally efficient and yields analytical insight, whereas FEA requires large computational effort and provides only numerical results. For purposes of routine computer simulation and initial design iteration, it is worthwhile to develop an MCA-based model that can

predict critical device characteristics with an accuracy roughly comparable to an FEA-based model. The following analysis is intended to serve as a first step in this direction.

The example three-phase machines are specified to have a feasible arrangement of poles and teeth. Some form of misalignment between opposing teeth is necessary in order to generate force when phase windings are energized. In this study, the pitches of opposing teeth are equal so a pole-to-pole offset is introduced to provide the required misalignment. Once the distribution of poles and teeth is established, an opportunity exists to shape the teeth. In this study, the teeth are rectangular and opposing teeth have equal width. Hence, the choice of tooth shape reduces to the choice of the ratio of tooth width to tooth pitch. This ratio should be between 0.33 and 0.50. In order to restrict the amount of data presented, only the extreme values of this parameter range will be considered.

Table 3-1 lists the parameters that define the geometry of the machines being investigated. MCA requires only the parameters appearing above the dividing line (primarily those defining air gap geometry), whereas FEA requires all of the parameters (including those defining magnetic material geometry). The choice of 200 turns per phase assumes use of AWG 21 wire for coils, and this implies a maximum phase current of about 8 A. The magnetic material is assumed to be M19 steel.

Table 3-1. *Parameters of Example 3-Phase Machines*

Air Gap Length	0.25 mm (each side)
Device Depth	50 mm
Tooth Pitch	10 mm
Tooth Width	3.33 mm – 5 mm
Teeth per Pole	3
Turns per Phase	200
Tooth Length	5 mm
Pole Length	10 mm
Back Iron Length	15 mm
Pole Pitch / Tooth Pitch	4.33

MCA has been implemented in MATLAB. FEA has been implemented in MAGNET, using a 2D magnetostatic solver and adaptive mesh refinement, yielding flux linkage and force values. Due to symmetry, only the top half of the machine and surrounding air box is included in the problem domain.

The machines of Table 3-1 are analyzed, for the cases of minimum tooth width and maximum tooth width. The analyses are restricted to the position interval [0,5] mm, i.e. one-half of the tooth pitch, due to periodicity and symmetry. The reference position x = 0 mm is chosen to represent the aligned position for pole-pair 1; x = 5 mm therefore corresponds to the unaligned position for pole-pair 1. The self inductance $L_{11}(x)$ and mutual inductance $L_{23}(x)$ both possess even symmetry about x = 0 mm. The force F(x) due to constant current in phase 1, being proportional to the spatial derivative of $L_{11}(x)$, exhibits odd symmetry about x = 0 mm.

Visualizations of the two machines in aligned and unaligned positions are shown in Figures 3-14 and 3-4. The upper portion of Figure 3-14 (the aligned case) and the lower portion of Figure 3-15 (the unaligned case) illustrate the logic behind the tooth width feasibility constraints. The minimum feasible tooth width is 3.33 mm since any further decrease in tooth width would eliminate tooth overlap where overlap is desired. The maximum feasible tooth width is 5 mm since any further increase in tooth width would lead to tooth overlap where none is wanted.

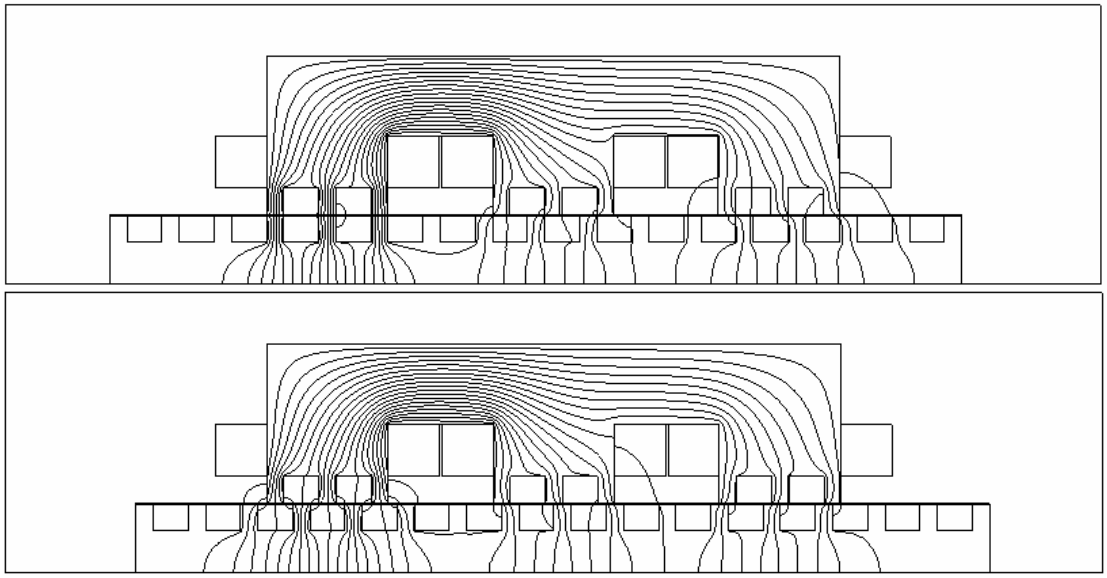

***Figure 3-14**. Flux contours for minimum tooth width design for i_1 = 1 A.*

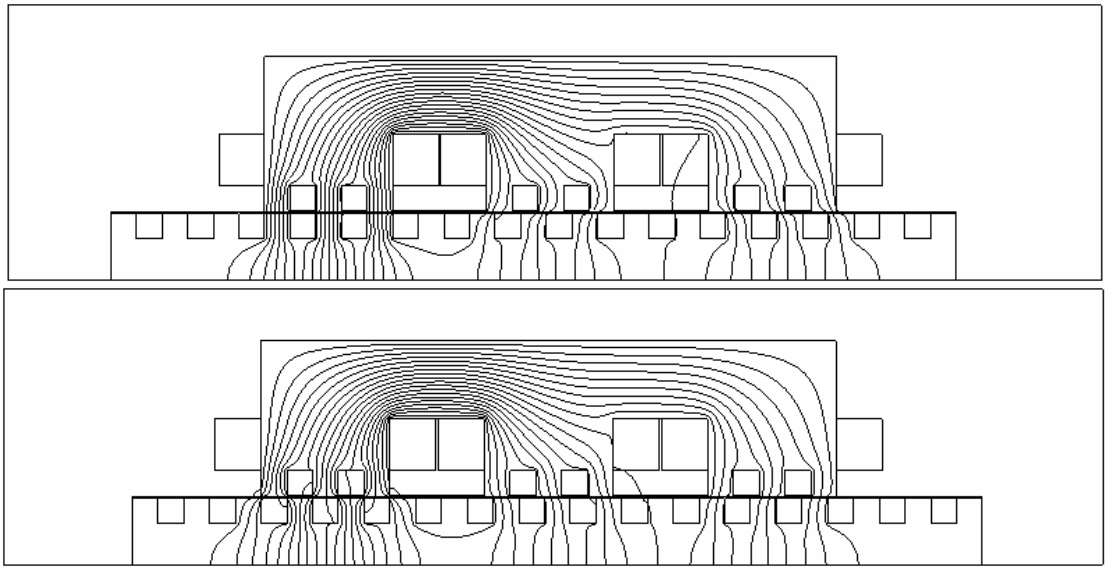

***Figure 3-15**. Flux contours for maximum tooth width design for i_1 = 1 A.*

The flux contours shown in Figures 3-14 and 3-15 are obtained from FEA with 1 A excitation in phase 1. Magnetic coupling between phases is clearly evident. The only difference between the two machines is the width of their teeth, yet this difference has a very significant impact on the

two air gap geometries. The machine with minimum tooth width has relatively high-reluctance flux paths, and hence relatively lower levels of flux. The machine with maximum tooth width has relatively higher flux densities, and hence relatively deeper saturation of magnetic material. In the aligned position, evidence of saturation appears at 5 A for the maximum-tooth-width machine and at 7 A for the minimum-tooth-width machine.
Comparisons between MCA and FEA are shown in Figures 3-16 through 3-18. FEA data for L_{11} and L_{23} are generated by computing λ_1/i_1 and λ_2/i_3, respectively, using single phase excitations of 1 A. FEA data for F are generated using the Maxwell stress method. These comparisons demonstrate a qualitative agreement between the two analysis methods, at low excitation; each method indicates the same trends with respect to x and tooth width. Strong magnetic coupling is revealed by the fact that the mutual inductances are roughly as large as the self inductances. The size of the harmonics in the spectra of the inductance-position profiles is significant; the harmonic content of the force-position profile is further amplified due to spatial differentiation.

As a function of x, self inductance modeling mismatch is in the range of 0.3-10.8 % for the narrow tooth design and 0.6-4.8 % for the wide tooth design; mutual inductance modeling mismatch is in the range of 1.4-33.7 % for the narrow tooth design and 0.9-16.1 % for the wide tooth design; and worst-case force modeling mismatch is 1.0 N for the narrow tooth design and 0.3 N for the wide tooth design. For each design individually, the inductance predictions are in best agreement at positions for which more magnetic material occupies the air gap regions; in these positions, the flux paths are more predictable and hence are more accurately modeled by simple magnetic circuits. Since the narrow tooth design uses less magnetic material in the air gap regions than the wide tooth design, the flux paths of the narrow tooth design are less well modeled by simple magnetic circuits than the flux paths of the wide tooth design; this accounts for the differing levels of modeling mismatch for the two designs. Since force depends on the spatial derivative of inductance, the positions at which force modeling mismatch is large are those positions at which the inductance slopes (rather than magnitudes) exhibit large modeling mismatch.

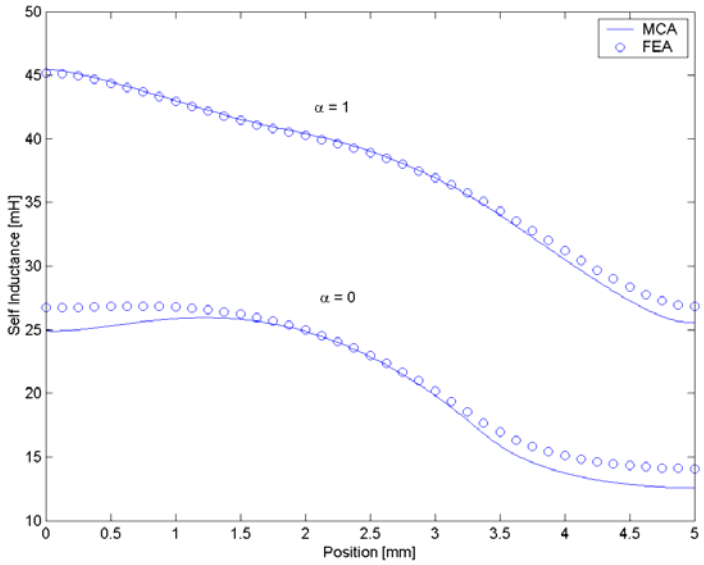

Figure 3-16*. Self inductance $L_{11}(x)$ for min and max tooth width designs.*

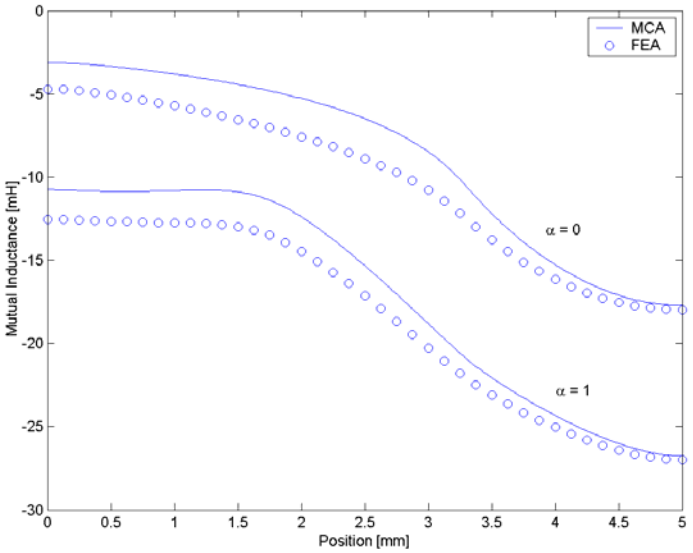

***Figure 3-17**. Mutual inductance $L_{23}(x)$ for min and max tooth width designs.*

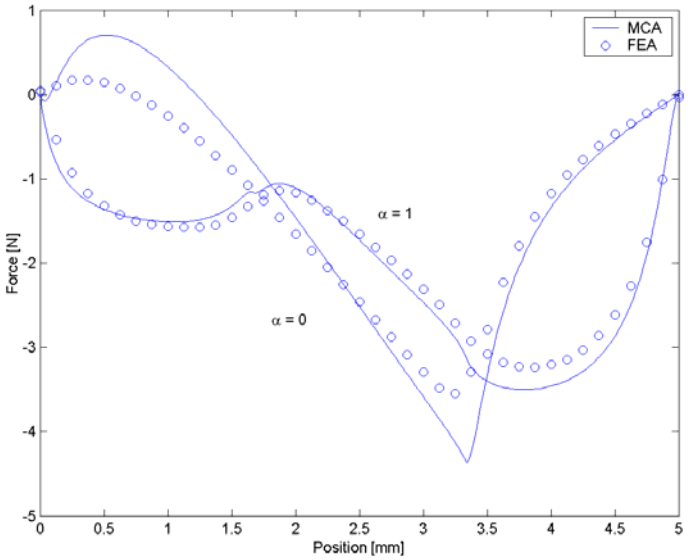

***Figure 3-18**. Force F(x) for min and max tooth width designs for i_1 = 1 A.*

In conclusion, two complementary analysis methods for LVR machines with magnetically coupled phases have been presented. Although qualitative agreement was demonstrated for low levels of excitation, the comparative analysis has revealed the need for more accurate magnetic circuit modeling. The magnetic circuit method could be improved by including flux-density-dependent permeances to model saturable magnetic material, as well as additional air gap permeances to model probable leakage paths. Such improvements could lead to a more complete and reliable characterization of the main performance trends with respect to tooth width and excitation level.

4. Fabrication and Testing of Microgenerator Subcomponents

Mark Allen and Ari Glezer

4.1 FABRICATION PROCESSES

4.1.1 Introduction

The microfabrication component of the program has focused on development of dense arrays of MEMS-fabricated permanent magnets and their use in conjunction with microcombustion to form a permanent magnet electrical generator based on combustion-driven machinery. This project requires both the development of dense arrays of permanent magnet materials, and integral microcombustion-driven thermal-to-mechan-ical energy conversion. The specific goals of the project are:

• Development of fabrication processes which will allow multilayer construction of materials which can withstand high operation temperature;

• Development of fabrication processes which allow the integrated fabrication of arrays of high energy density magnets;

• Development of microcombustion processes and machinery which result in a micromachined free-piston engine, the piston of which can shuttle back and forth between two combustors, and in which the magnetic saliency of the piston in combination with the permanent magnet arrays will be used to generate electrical energy.

Figure 4.1-1 illustrates the overall set of MEMS components which have been finalized for the current version of the demonstration microgenerator. The ceramic laminate housing with integrated microfluidic channels forms the central basis for the device. Each end of the device contains a combustion chamber which houses a spark ignition source. In the central region of the device, a drop-in piston shell with magnetic gaps to allow the conduction of flux from the alternating-magnet piston to external windings is provided. This piston shell also allows for improved sealing over that previously achievable with ceramic pistons. Finally, the bottom and top layers in the ceramic housing are provided with magnetic vias to allow for flux conduction from the inside of the microgenerator to the outside surface. These magnetic vias are then interfaced with an external set of pole pieces and windings to complete the device.

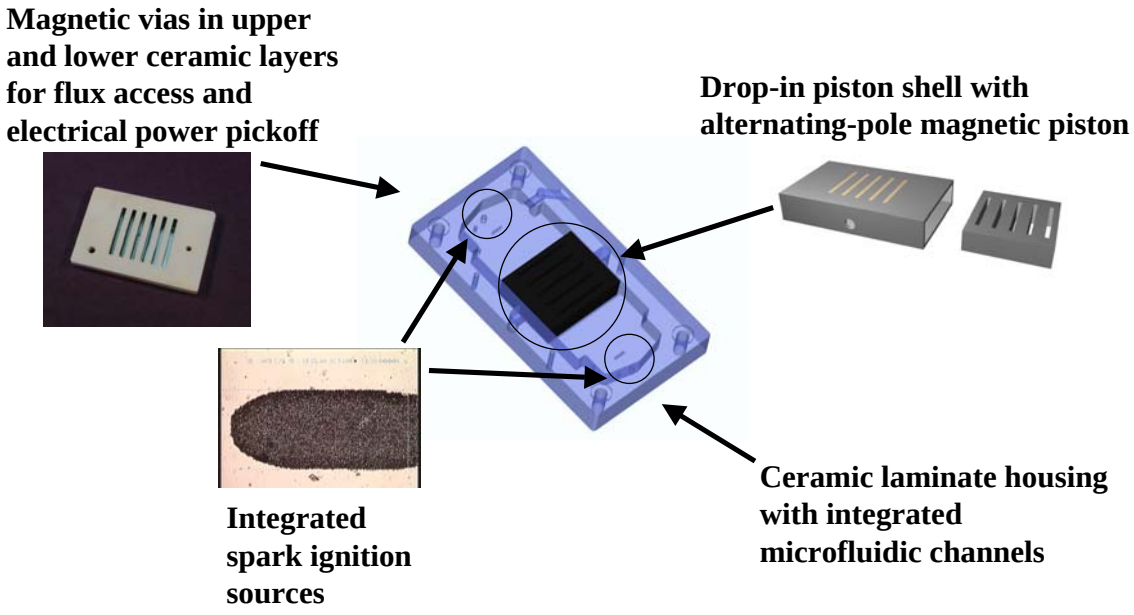

Figure 4.1-1. *Current implementation of mirogenerator.*

4.1.2 Integrated single- and dual-chamber ceramic housing

Figure 4.1-1 illustrates the current development status of the integrated ceramic housings. Figure 4.1-2a shows a single-chamber combustor. The combustion chamber is in the foreground of the picture, and the opening in the rear of the housing is for access to an external pushrod connected to the piston so as to allow for pickoff of generated mechanical power. Note that the device in Figure 4.1-2a has the drop-in piston housing fastened into it for sealing of the moving piston. The drop-in piston housing is made using conventional machining techniques (EDM).

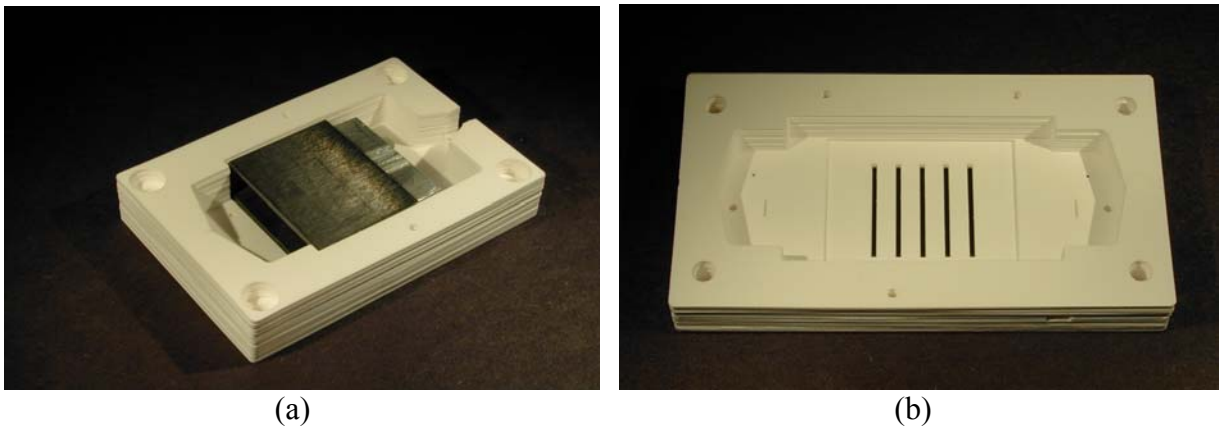

(a) (b)

Figure 4.1-2. *(a) Single-combustor ceramic housing. (b) Dual-combustor housing.*

Since the device of Figure 4.1-2a will have the power taken out by means of a mechanical pushrod, magnetic saliency is not provided in the ceramic housing or the drop-in piston housing. Figure 4.1-2b shows a dual-chamber combustor prior to installation of the drop-in housing. The ports for magnetic vias to be electroplated in the bottom of the housing are shown. A complementary structure, containing ports in the upper plate, is not shown so that the interior of the ceramic housing can be viewed. The combustion performance of these devices will be described in the next section.

4.1.3 Magnetic via plating

The plating of the magnetic vias through ceramic represents a challenge due to the relatively large thicknesses of magnetic material that must be deposited (in some implementations of the device, on the order of 1 mm). However, other than this issue, the basic fabrication procedure is straightforward and is described in Figure 4.1-3. The ceramic layers which will form the upper and lower layers of the device are patterned, stacked, laminated, and fired as described in previous reports (Figure 4.1-3a). After deposition of a suitable seed layer, the via openings are filled with 80% Ni / 20% Fe permalloy using a standard Watts bath and pulse plating so as to achieve the large thicknesses required while simultaneously maintaining uniformity over the device. Some degree of overplating is performed so as to ensure that all void spaces in the vias are completely filled. The devices are then polished (which is relatively easily performed due to the relative hardness difference between the ceramic and the permalloy) to create the completed magnetic-via-bearing layer. Such a completed device is shown in Figure 4.1-4. The vias shown in Figure 4.1-4 are 1 mm in width, 1.5 mm in height, and 15 mm in length.

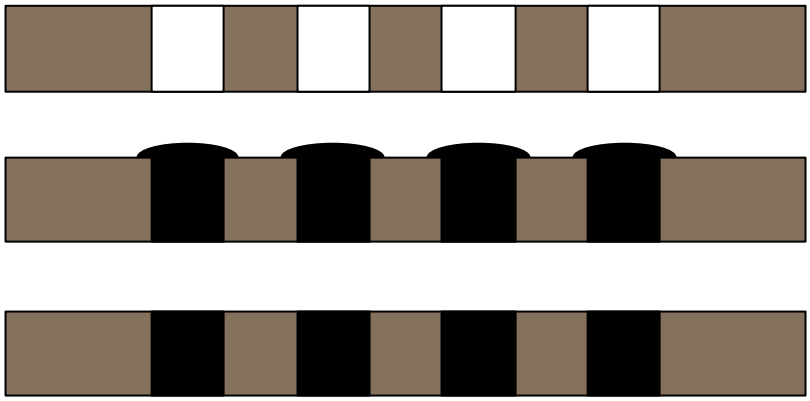

Figure 4.1-3. *Fabrication sequence of magnetic vias in ceramic housing. (Top): Ceramic greentape layers of the appropriate dimensions are stacked, laminated, and fired; (Middle) After deposition of seed layer, pulse-plating is utilized to fill the ceramic vias with 80/20 Ni/Fe permalloy; (Bottom) the surface is planarized by polishing to complete the fabrication.*

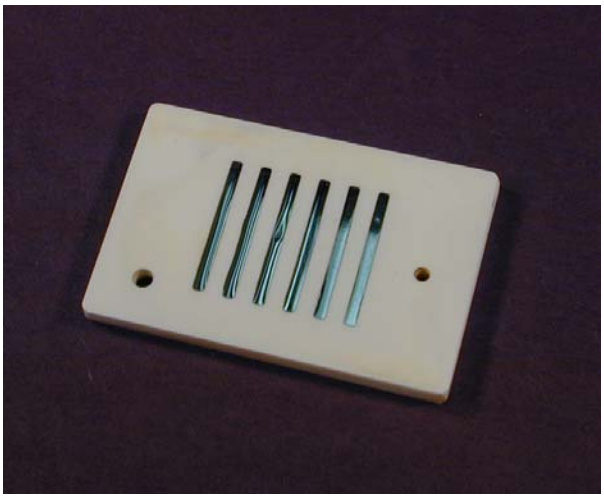

Figure 4.1-4. *Photomicrograph of fabricated ceramic vias. The vias are 1 mm in width, 1.5 mm in thickness, and 15 mm in length.*

4.1.4 Piston Fabrication

The piston fabrication represented a challenge since it was difficult to create the dense, alternately poled array required for the microgenerator application using conventional magnetization techniques. Due to its high coercivity and remanence, as well as its relatively high Curie temperature, samarium-cobalt-based materials were chosen as suitable for the piston application. The high coercivity and remanence leads to a high energy product, which ultimately leads to better electrical performance. However, magnetic fields on the order of three times the coercivity are required to magnetize these materials, therefore requiring fields on the order of 30,000 Oe. A major challenge in creating dense, alternately-poled arrays is therefore the localization of these extremely large fields which results in correspondingly large spatial magnetic field and flux gradients.

Due to limitations on saturation flux density of many materials, it is difficult to localize these fields using a magnetic core approach. Without cores (e.g., by using just the magnetic fields generated by arrays of wires), it was difficult to achieve the required spatial gradients. Therefore, a 'clamshell'-like approach was taken, in which the piston was split lengthwise down the middle, each half of the piston was separately magnetized, and the two halves of the piston were then assembled to form the final device.

Figure 4.1-5 illustrates the fabrication concept. Two piston layers are provided which contain vias of pitch corresponding to that of the magnetic vias described in the previous section, and which have thickness equal to one-half of the final piston thickness. Alternating vias in the piston are filled with samarium-cobalt (a 'hard' magnetic material which has substantial remanence), and magnetized. Note that since all of the magnetization to be performed is in the same direction, the need for large spatial field gradients is eliminated, and the magnetization can proceed simply, e.g., by use of an external coil of diameter sufficient to encircle the entire piston. Following the magnet deposition and magnetization, nickel-iron permalloy (a 'soft' magnetic material with low remanence and coercivity which acts solely as a flux conductor), is deposited

into the remaining alternating open vias using, e.g., electroplating technology (as described previously). Finally, one of the piston layers is flipped and bonded to the other, to produce the alternating array.

Figure 4.1-6 shows a photomicrograph of the fabricated piston. On the left, in the background is a single layer of alternating hard and soft magnetic material corresponding to Figure 4.1-5c. In the foreground is an assembled piston of the final thickness corresponding to Figure 4.1-5d. In order to demonstrate the magnetic functionality of the piston, magnetic viewing paper (which consists of a fine powder of magnetic material suspended between two sheets of transparent material) is placed over the piston. The magnetic powder aligns itself along flux lines and allows for a straightforward way to qualitatively assess magnetic flux lines. As can be seen, an alternating array of flux lines has been produced using this approach. This qualitative measurement of the alternating characteristic of the flux lines has been confirmed using quantitative gaussmeter measurements.

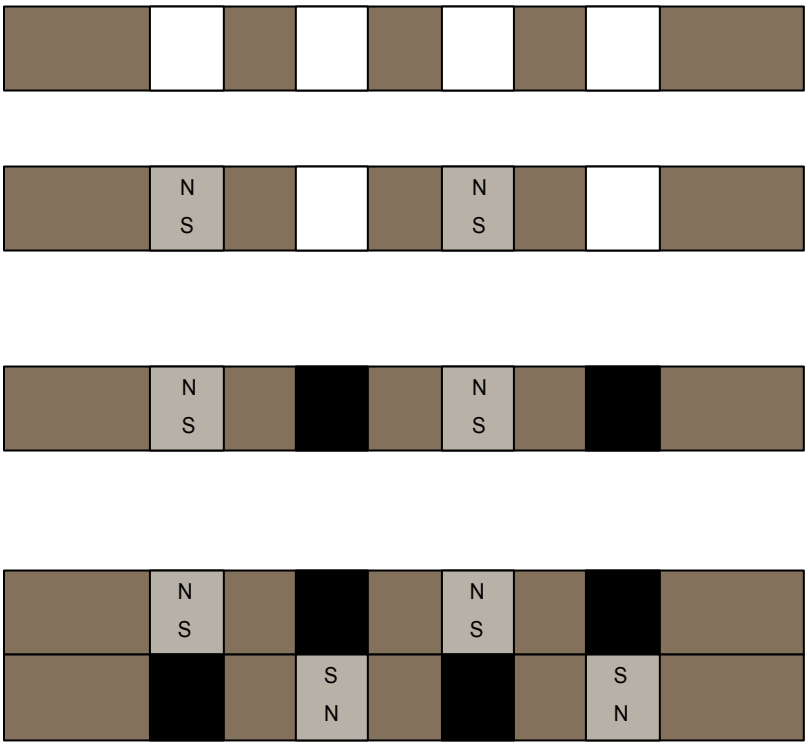

Figure 4.1-5. *Fabrication sequence for alternately-poled magnetic array. From top to bottom: (a) Piston layer with vias and with thickness equal to one-half the final piston thickness; (b) deposition and poling of hard magnetic material; (c) deposition of soft magnetic material; (d) flipping of second layer identical to (c) and bonding so as to produce the alternately-poled array.*

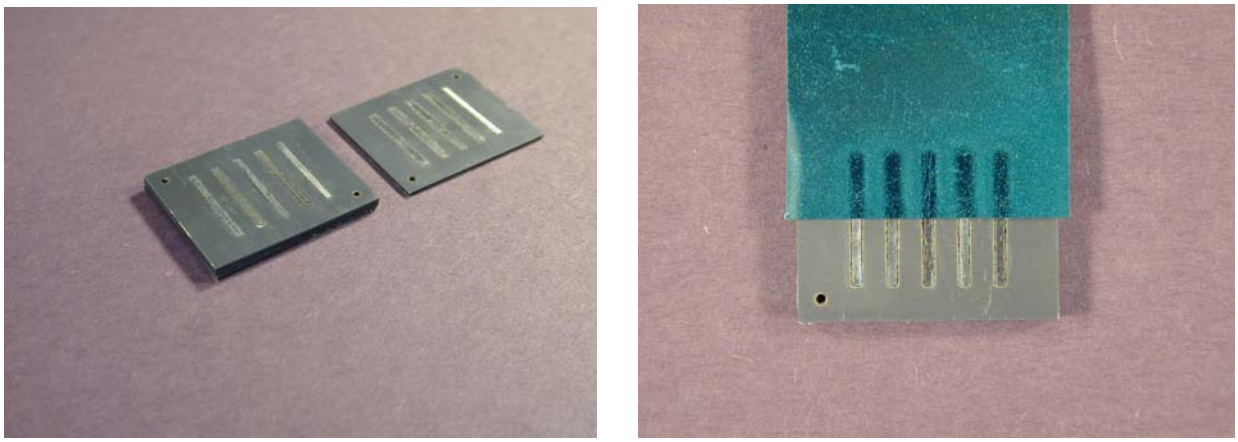

(a) (b)

Figure 4.1-6. *Photomicrograph of alternately-poled array. (a) The assembled piston is in the foreground and a single piston layer is in the background. (b) Magnetic viewing paper is placed over the assembled piston so that the alternating nature of the magnetic field can be seen.*

4.1.5 Combustion Performance of Single-Chamber Combustor

The single-chamber ceramic housing with drop-in piston housing and piston and spring-return, has been assembled and tested using propane fuel. Figure 4.1-7 shows a photomicrograph of the tested system. Note that the magnetic-via-bearing ceramic plates have been replaced with glass so as to visualize the motion of the piston.

The piston operates with a single continuous flow feed of premixed propane/air which is delivered through the microfluidic passages defined within the ceramic housing. A single passive check valve is utilized during operation to maintain pressure within the housing during the piston stroke. The piston is 6mm in thickness. The frequency of operation of the device is 7 Hz and the stroke is approximately 1.5 cm.

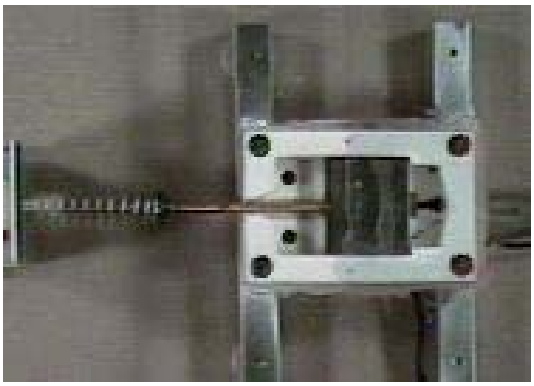

Piston at TDC

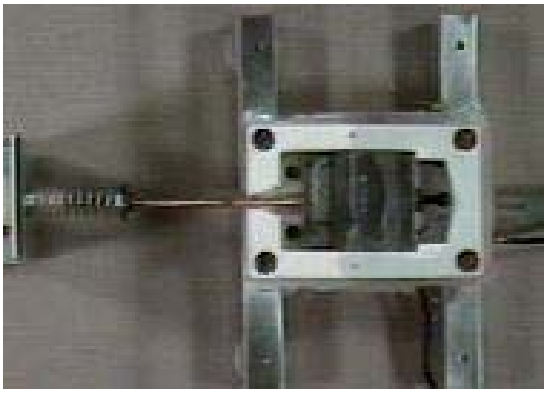

Piston at mid stroke

Figure 4.1-7. *Single-chamber piston device in operation. Note that an external spring-return is utilized to extract mechanical energy. The two photomicrographs are stills from actual operation with the piston at top dead center (top) and at mid-stroke (bottom).*

4.1.6 Combustion Performance of Dual-Chamber Combustor

The dual-chamber ceramic housing with drop-in piston housing and free-floating piston has been assembled and tested using propane fuel. Figure 4.1-8 shows a photomicrograph of the tested system. Note that as in Figure 4.1-7 the magnetic-via-bearing ceramic plates have been replaced with glass so as to visualize the motion of the piston.

The piston operates with a single continuous flow feed of premixed propane/air which is delivered through the microfluidic passages defined within the ceramic housing. Again, the piston is 6mm in thickness. The frequency of operation of the device is 5 Hz and the stroke is approximately 2 cm. Work during the next reporting period will focus on the further integration and testing of both of these devices.

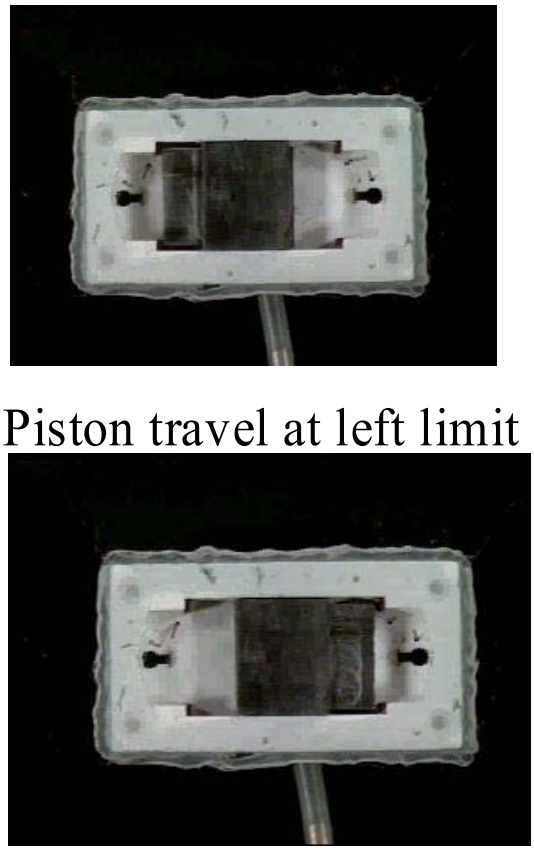

Figure 4.1-8. *Dual-chamber piston device in operation. The two photomicrographs are stills from actual operation with the left travel limit (top) and at the right travel limit (bottom).*

4.2. MAGNETIC LAMINATIONS FOR MICROMACHINED ENERGY ONVERSION DEVICES

4.2.1 Introduction

Operation of magnetic-based mechanical to electrical energy conversion devices will require strategies to reduce generated eddy currents, which introduce inefficiencies into the conversion process. One approach to realizing this task is to utilize laminations in the device. The incorporation of laminations into micromachined magnetic components has the potential to reduce eddy current losses induced in the cores of these components. This section reports on a developed manufacturing technique for the fabrication of highly laminated magnetic cores. The approach is based on an alternating, conformal sequential electroplating of layers of NiFe and Cu, followed by selective sacrificial etching of the Cu. Since the copper sacrificial interlayer is itself conducting, it can act as a plating base for the subsequent deposition of NiFe without the necessity of multiple vacuum steps, multiple coating of insulating layers, or multiple photolithography steps. Highly laminated structures can therefore be achieved merely by alternating plating baths during fabrication, followed by selective removal of the Cu layers to provide electrical insulation between the magnetic layers. The fabrication approach can be

readily adapted to a wide range of core geometries. To illustrate the improvements in magnetic properties achievable using this technique, the magnetic core fabrication technology has been successfully combined with integrated solenoid-like coils in order to fabricate a complete integrated inductor, which has been designed to operate in the low MHz range for power conversion applications. Inductors with highly laminated cores fabricated using the sacrificial layer approach exhibit quality factors exceeding those of unlaminated core devices by a factor of 3-4 at a frequency of 1 MHz.

Conductive, electroplated NiFe alloys such as permalloy have been widely used for the fabrication of electromagnetic MEMS components. One example of their application has been as energy storage elements in switched-mode power converters. As switching frequencies increase, it is possible to reduce the values and overall dimensions of the magnetic components in these converters [1]. However, as frequencies increase (e.g., into the low MHz region and beyond), core losses (e.g., due to eddy currents) in unlaminated conducting cores also increase, driving the use of low conductivity core materials such as ferrites. Since many ferrites have lower saturation flux densities than NiFe alloys the overall dimensions of the device resist further miniaturization. Thererfore, there is a need for processes to fabricate laminations in conducting, micromachined permalloy cores.

It should be noted that core losses can result from both hysteresis effects and eddy current effects. This paper focuses primarily on the reduction of eddy current effects. In macro-scale magnetic devices, low-loss laminated cores are typically achieved by stacking alternating layers of core material and insulating material (which blocks eddy current flow), and laminating the entire stack together. Laminations have also been utilized in micromachined magnetic components. Previous approaches to micromachined laminations include one-step electroplating of vertical high-aspect-ratio structures [2]; repeated deposition of insulator, seed layer, and NiFe films [3]; multiple sputtering of thin magnetic and dielectric layers [4]; and mechanical lamination of polymer-coated NiFe foils [5].

Although these approaches have demonstrated improvement in device performance, processability and scaling remain as unaddressed issues. As permeabilities and desired operation frequencies increase, lamination thicknesses should be reduced to the micron range (i.e., on the order of the magnetic skin depth) while simultaneously maintaining total core thicknesses of tens to hundreds of microns to prevent saturation. These requirements dictate large numbers of thin, high-aspect-ratio laminations, which are difficult to achieve using the previously-described approaches. For example, in the case of vertically-laminated structures, the required aspect ratio of the mold laminations increases, making mold fabrication difficult. Horizontal lamination using repeated deposition of magnetic thin films and insulators, e.g., by sequential sputtering, overcomes this difficulty but may not be able to achieve the required overall stack thicknesses due to stress issues. Electroplating of horizontal laminations offers the possibility of fabricating structures of sufficient overall thickness, but the repeated switching of substrates between plating bath and vacuum system as detailed in [3] becomes unmanageable as the number of layers increases. Finally, conventional foil lamination becomes difficult as the foil thickness approaches the micron range, especially since mechanical strain of magnetic foils has been demonstrated to degrade magnetic properties.

In this section, a manufacturable approach allowing micron-scale (or smaller) laminations and large total core thickness without the need for interposing vacuum steps or sub-micron lithography is presented. The approach is based on *sequential electroplating* to form densely alternating stacks of magnetic and nonmagnetic material. Previous work in sequential electroplating has produced compositionally-modulated stacks, which have been proposed as fabrication aids [6] or nanostructured materials with improved wear characteristics [7]. In this work, the focus is on the exploitation of this technique to create laminations. The approach is based on an alternating, conformal sequential electroplating of layers of NiFe and Cu, followed by selective sacrificial etching of the Cu. Since the copper sacrificial interlayer is itself conducting, it can act as a plating base for the subsequent deposition of NiFe without the necessity of multiple vacuum steps, multiple coating of insulating layers, or multiple photolithography steps. Highly laminated structures can therefore be achieved merely by alternating plating baths during fabrication, followed by selective removal of the Cu layers to provide electrical insulation between the magnetic layers. Additional features are also incorporated in the fabrication sequence to ensure mechanical integrity of the lamination stack after removal of the sacrificial layer.

4.2.2 Core Design Considerations

Lamination of the core of an inductor is particularly effective when the thickness of an individual lamination layer is on the order of (or smaller than) the skin depth of the given material at a given frequency of operation. The magnetic material used in this work is electroplated NiFe. Its reported relative permeability and conductivity are 800 and $5x10^6(\Omega.m)^{-1}$, respectively [2]. In the hundreds of kHz to MHz range of frequencies, the skin depth of NiFe is on the order of tens of microns. Therefore, each individual NiFe lamination will be fabricated in this thickness range in order to determine the utility of this approach.

Figure 4.2-1 illustrates examples of cores fabricated in this work. Figure 4.2-1 is a schematic cross section of a solid core inductor that suffers from eddy currents, and which will be used as a comparison benchmark to assess the laminated cores. Figure 4.2-2 is a 'perfectly' laminated core (i.e., complete electrical and, ideally, physical separation between laminations). Figures 4.2-3 and 4.2-4 represent the cross section of two laminated cores, fabricated using the sequential lamination process, which include supporting structures to hold each lamination in place. These supporting structures are utilized in order to maintain structural integrity of the core. Since the supporting structures will also be fabricated from NiFe for process convenience, the central V-shaped structure of (Figure 4.2-4) has been chosen, since it does not provide a closed electrical path for eddy currents to flow.

Initially, laminated cores were fabricated as described below and hand-wound with coils for testing purposes. Once the utility of the core was demonstrated, the core fabrication sequence was combined with fabrication of integrated coils to form fully integrated inductors.

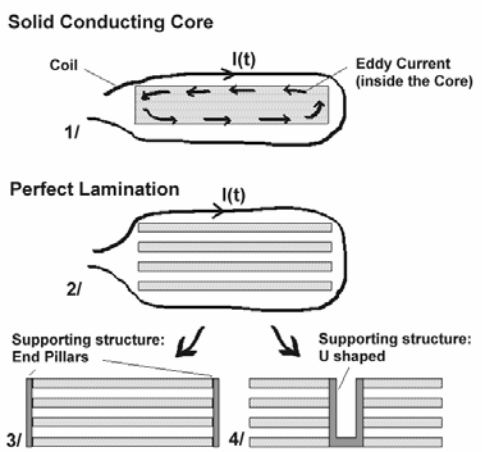

Figure 4.2.1 *Configurations for laminated and unlaminated magnetic cores*

4.2.3 Fabrication of Laminated Core

Using standard techniques, a seed layer is deposited on a substrate and a thick photoresist layer is processed in order to create a core mold. The mold is filled with sequential electrodeposition of NiFe (80%-20%) and Cu layers (Figure 4.2-2). Three 4 μm thick layers of NiFe are deposited. Each layer of NiFe is separated from the next NiFe layer by a 6 μm layer of Cu. Note that during the formation of the stack, each layer provides a good electrical base for the electrodeposition of the subsequent layer. Two adjacent Cu/NiFe multi-layered structures A and B separated by a central trench are hence created. The mold is removed and a new layer of photo-resist is patterned, opening a central trench between structures A and B. A final NiFe layer is then electrodeposited. This 4 μm thick layer coats the sidewalls

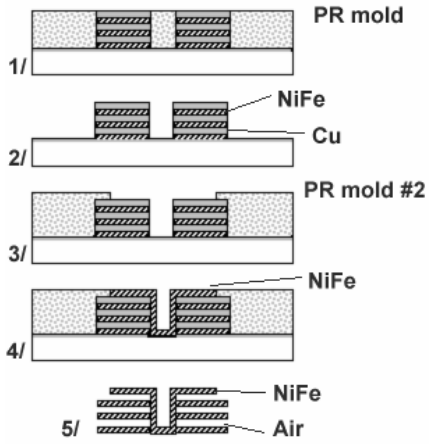

Figure 4.2-2: *Fabrication sequence of laminated core*

inside the trench as well as the upper surface of structure A and B. After removing the photo-resist mold, the fabrication of the core ends with the selective etching of the copper between the

NiFe layers. As described earlier, the V-shaped central NiFe layer is supporting each individual NiFe lamination once the Cu is removed.

Successful freestanding core structures were fabricated using the above process. Figure 4.2-3 shows a detail of the NiFe laminated core after Cu removal. The layers of NiFe are separated from each other by 6 μm of air.

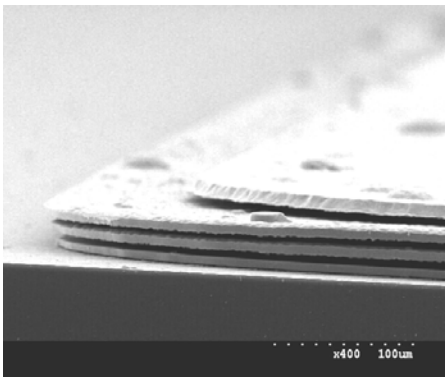

Figure 4.2-3 *Scanning Electron Micrograph of a laminated NiFe structure after Cu removal (detail)*

One potential limitation of this process is that as the horizontal aspect ratio of the laminations increases, the compliance of each lamination layer may also increase. For example, in some structures fabricated using the above process, visual inspection of some cores showed that some NiFe layers were touching at the periphery of the structure. If significant layer-to-layer electrical conductivity occurs at these contact points, the efficacy of the lamination structure is reduced. To assess the effects of unwanted mechanical contact between adjacent NiFe layers, three different cores were fabricated. Test core 'A' was fabricated using the technique described in the previous section, with four 4-μm-thick NiFe laminations. Test core 'B' was fabricated using multiple individual NiFe rings of the same thickness, fabricated separately, and stacked together with thin insulating films between them to most closely approach the 'perfect lamination' case of Figure 4.2.2. Test core 'C' was a solid NiFe ring fabricated using a single-step electroplating, with a total thickness equal to the sum of the lamination thicknesses in either core 'A' or core 'B'.

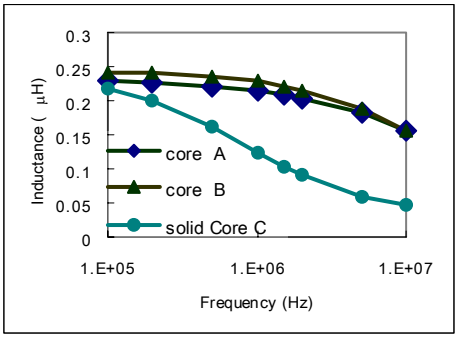

Figure 4.2-4 *Inductance vs frequency for 3 different test cores.*

Each core was hand-wound with insulated magnet wire in order to create a test inductor. The frequency response of these cores was then tested (Figure 4.2-4), using an HP4194A impedance analyzer. The results show that core 'A' (the micromachined laminations) favorably compares to core 'B' (the 'perfect' laminations). It should be noted that this result was obtained in spite of the fact that during the hand-winding process, core 'A' was subjected to significant mechanical compression. Both laminated cores exhibited significantly superior performance over that of solid core 'C', which showed a rapid decrease in inductance with frequency, characteristic of the limiting effects of eddy currents [8].

4.1.4 Fabrication of Integrated Inductors with Laminated Cores

Since lamination using this approach was demonstrated to produce magnetically-superior cores, the process of Figure 4.2-2 was combined with a standard integrated coil process to achieve fully-integrated, laminated inductors. This combined process is described below.

The bottom conductor lines of the coil are fabricated first using conventional micro-molding and electroplating of Cu. The lines are passivated under a layer of photosensitive epoxy, which is patterned in order to create electrical vias (Figure 4.2-5.1). A single Ti-Cu-Ti seed layer is deposited and the fabrication of the laminated core is performed as described earlier (Figure 4.2-5.2). Before removing the sacrificial Cu, a thin photoresist is spin-cast and patterned in order to clog the electrical via and protect the underlying Cu lines during the sacrificial Cu etch step (Figure 4.2-5.3). Once the laminated core is fabricated (Figure I.5.4), a thick layer of epoxy resist (SU-8) is then deposited, in order to further structurally reinforce the core as well as to allow completion of the coil (Figure 4.2-5.5). The layer of epoxy is patterned using photolithography. The core is now embedded under a structure of cross-linked epoxy and is surrounded by vertical vias. The vertical vias will later allow the fabrication of the vertical sections of the 3D conductor.

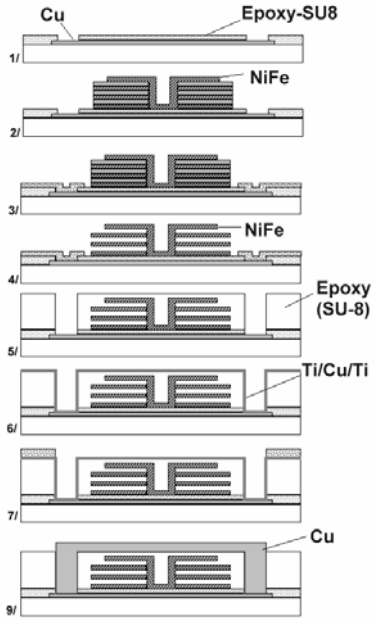

Figure 4.2-5 *Fabrication sequence for a complete integrated inductor.*

The entire structure is coated with a conformal layer of Ti/Cu/Ti using DC sputtering. (Figure 4.2-5.6). A thick layer of conventional photoresist is patterned to create horizontal openings connecting each vertical via at the upper surface of the epoxy structure (Figure 4.2-5.8). A final Cu electrodeposition yields the simultaneous fabrication of the vertical as well as the upper horizontal parts of the Cu conductor. The photoresist and seed layer is removed (Figure 4.2-5.9). A photomicrograph of the fabricated device is given in Figure 4.2-6.

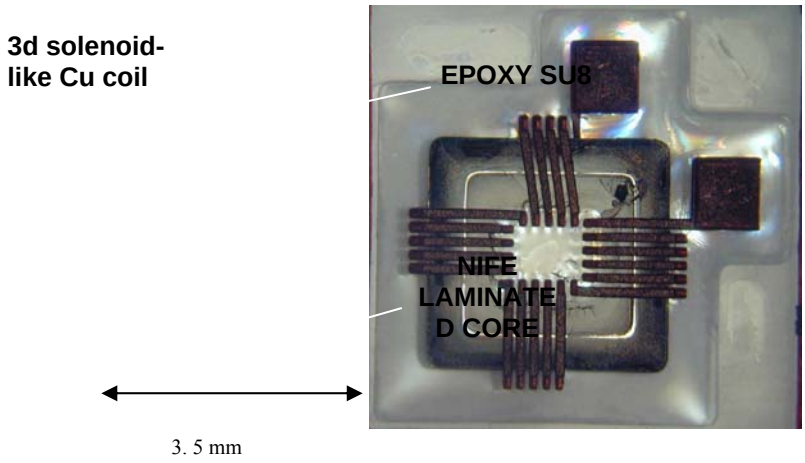

Figure 4.2-6 *Photomicrograph (top view) of a complete integrated inductor with laminated NiFe core.*

4.2.5 Integrated Inductor Characterization

To illustrate the improved characteristics of a laminated core, a solid core integrated inductor with the same cross-sectional core area as the device of Figure I.6 was fabricated, and both devices were tested using an HP4194A impedance analyzer. Their respective inductances and Q-factors are shown in Figures I.7 and I.8.

Figure 4.2-7 shows that the inductance of both devices decreases with increasing frequency. However, the inductance of the solid core inductor decreases faster than its counterpart, suggesting that eddy current effects are significantly reduced in the case of the laminated core inductor. This is confirmed by Figure I.8 that displays the respective Q-factors of both inductors: the Q-factor of the laminated core inductor is approximately 3-4 times larger than that of the solid core inductor at 1MHz.

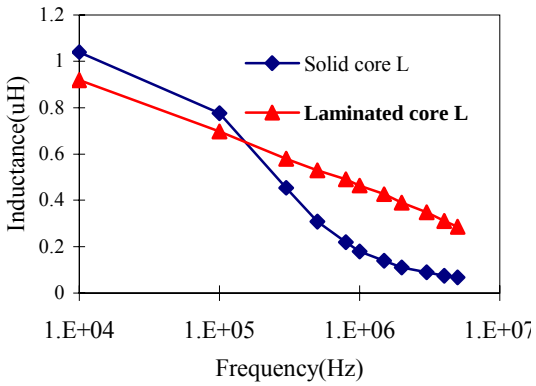

Figure 4.2-7 *Inductance of solid and laminated core integrated inductors as a function of frequency.*

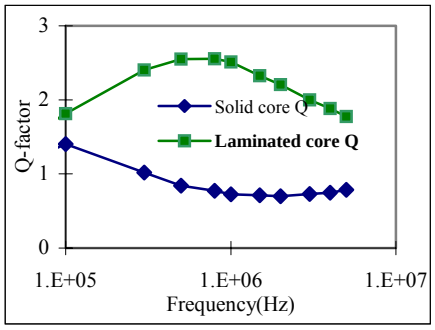

Figure 4.2-8 *Quality factor (Q) of solid and laminated core integrated inductors as a function of frequency.*

References

[1] C. R. Sullivan and S. R. Sanders, "Microfabrication of transformers and inductors for high frequency power conversion," in *24th Annu. Power Electronics Specialists Conf.,* June 1993, pp. 33–40.

[2] M. Xu, T. M. Liakopoulos, C. H. Ahn, S. H. Han, and H. J. Kim, "A microfabricated transformer for high-frequency power or signal conversion," *IEEE Trans. Magn*., vol. 34, pp. 1369-1371, July 1998.

[3] J. Park, S. H. Han, and M.G. Allen, "Batch-fabricated microinductors with electroplated magnetically anisotropic and laminated alloy cores," *IEEE Trans. Magn.,* vol. 35, no. 5, pp.4291-4300, 1999.

[4] C. R. Sullivan and S. R. Sanders, "Microfabrication process for high-frequency power-conversion transformers," in *26th Annu. Power Electronics Specialists Conf.,* June 1995, pp. 658-664.

[5] J. Park, J. Y. Park, Y. Joung, and M. G. Allen, "Fabrication of high current and low profile micromachined inductor with laminated Ni/Fe core," *IEEE Trans. Component and packaging Technology,* submitted.

[6] S. Leith and D. T. Schwartz, "In situ fabrication of sacrificial layer in electrodeposited NiFe micro-structures," J. Micromech. Microeng. , 9 1999, p 97-104

[7]C. Yang and H. Y. Cheh, "Pulsed Electrodeposition of Copper/Nickel multilayers on rotation disk electrodes," J. Electrochem. Soc., Vol. 142, no.9, sep. 1995 3034-3039

[8] J. Lammeraner, and M. Stafl, *Eddy current*. London: Iliffe Books Ltd., 1966, Chapter 2

4.3 CONTROLLED ENGINE PEFORMANCE

4.3.1 System Description

A critical component of the microgenerator work is the development of a real-time feedback controller for the piston motion. The overall concept is to enable controlled interaction between the piston and the generator to achieve improved thermodynamic performance and power generation. This approach can be adapted to both single and dual combustor systems. To this end, we have constructed a real-time close loop control system that is coupled with a piton-combustor via a voice coil actuator. In the first generation system, the controller was a Motorola HC12 microprocessor while in the later more advanced system, the controller is based on a PC-based QNX operating system. The cycle parameters that are monitored by the control system include the instantaneous combustion chamber pressure, and the piston position, velocity and force. The schematic of a system is shown in Figure 4.3-1 and photographs of the components are shown in Figure 4.3-2.

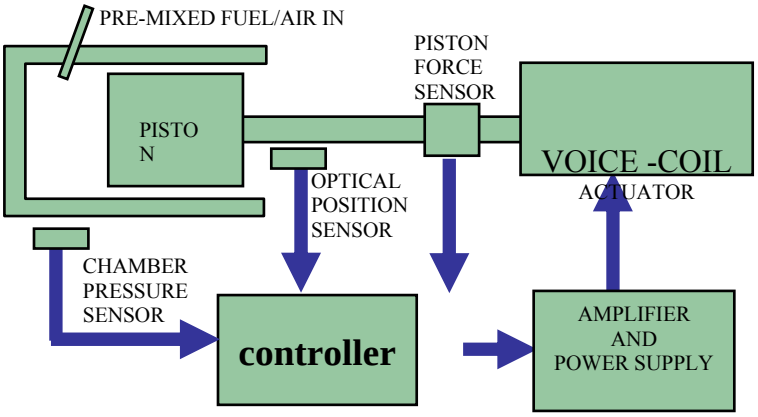

Figure 4.3-1 *A schematic diagram of the generator with the control circuitry*

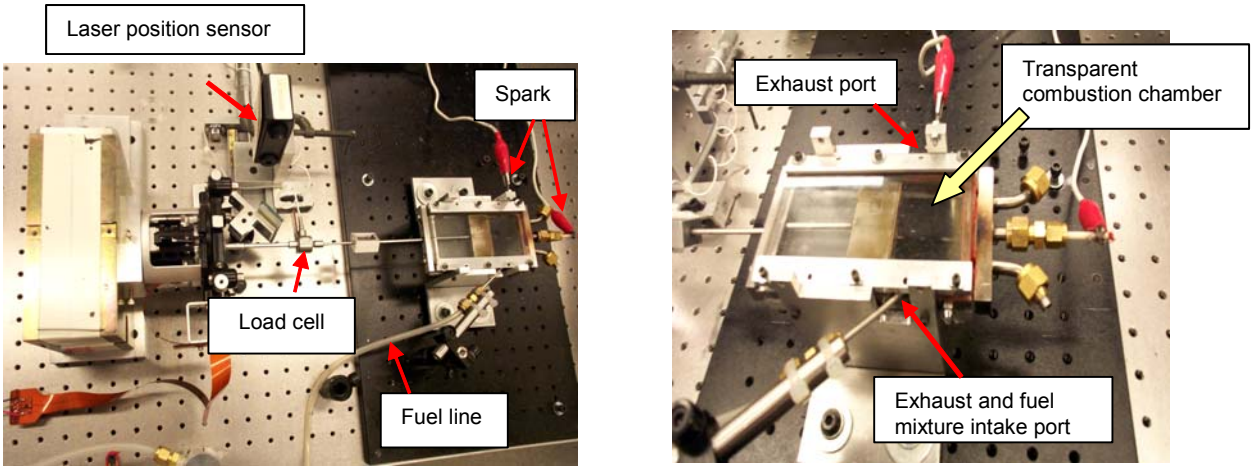

Figure 4.3-2 *The free piston engine and the voice coil actuator (left) and a close up view of the engine (right)*

An example of the controller's capability is demonstrated by counteracting the inertial forces that are associated with the mass of the mechanical moving parts. Figure 4.3-3 shows time traces of the

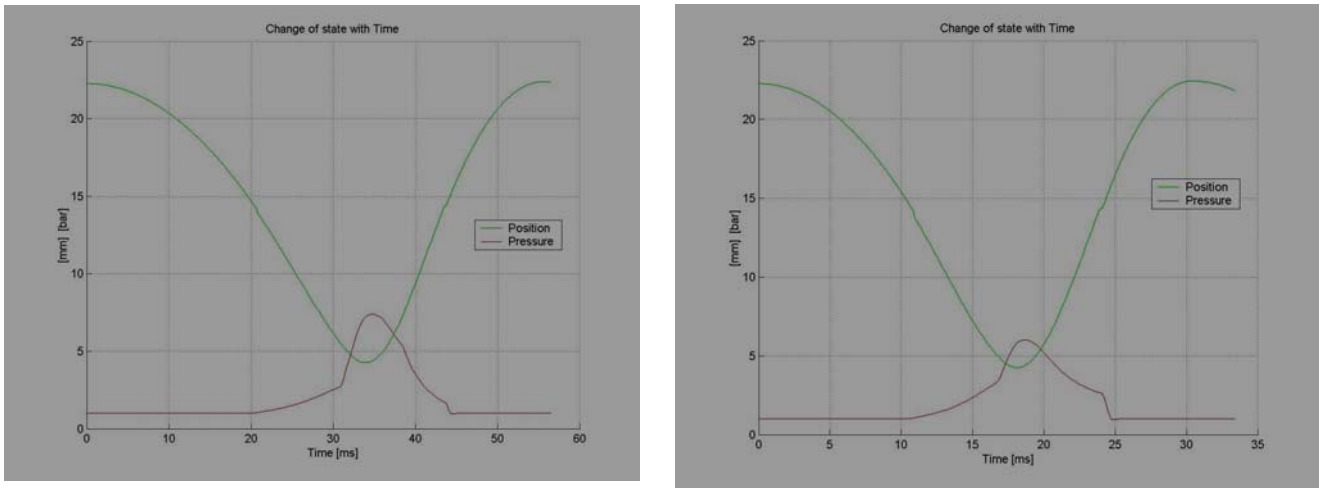

Figure 4.3-3 *Position and pressure traces without (left) and with (right) mass compensation*

combustion chamber pressure and piston position. The plot on the left is for the uncompensated piston motion while in the plot on the right the controller compensates for the mass of the moving parts and allows in effect to "prescribe" a lighter piston system which completes the cycle faster and therfore can opertae at higher frequency and power. Figure 4.3-4 shows the P-V diagrams that correspond to the data in Figure 4.3-3 for the "free" piston engine (right) and the engine with an uncompensated mass (left). These data clearly demonstrate that the power production using the controlled, "free" piston is greater.

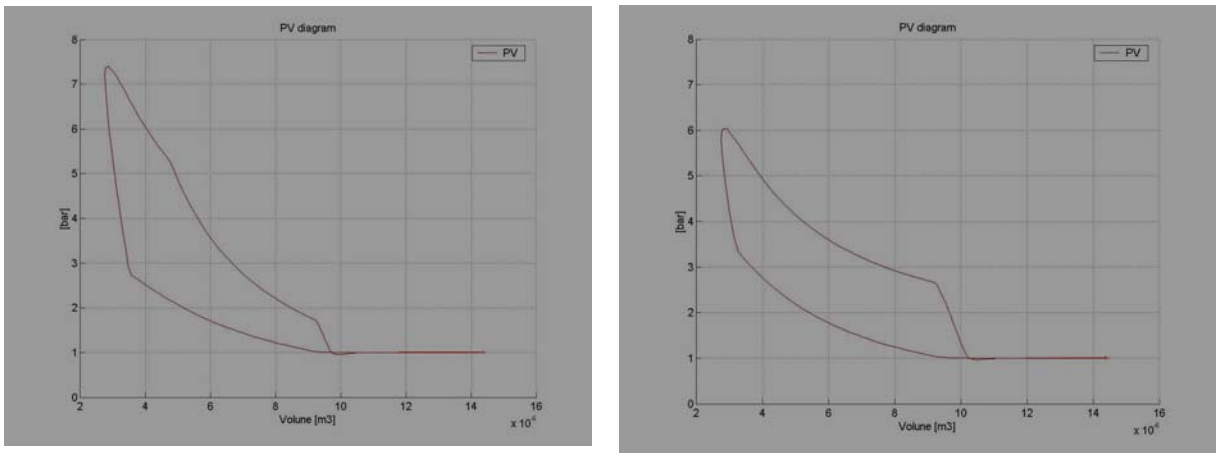

Figure 4.3-4 *PV diagrams corresponding to Figure 1-10.*

Using these operating approach it was possible to achieve the following performance

	Uncompensated:	"Free" piston :
Thermodynamic Power	23.1 W	40.8 W
Shaft Power	17.5 W	1.5 W
Frequency	17.9 Hz	32.9 Hz
Maximum Pressure	7.4 bar	6.0 bar

As noted above, the controller was later implemented in a PC-based QNX operating system that can be easily modified to achieve different control modes (e.g., constant force, controlled displacement, etc.). The ultimate objective is to optimize the power generation by influencing the thermodynamic cycle using controlled compression and expansion and scavenging.

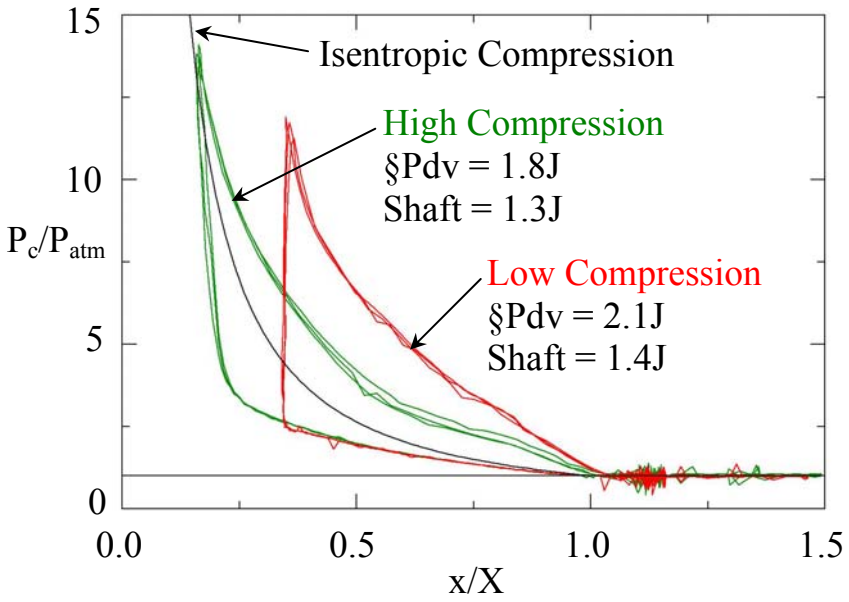

An example of the effect of controlled thermodynamic cycle is shown in Figure 4.3-4. Two cases are shown for low- and high-compression, respectively that are obtained by altering the time history of the piston motion. These data show that higher compression ratio yields higher peak chamber pressure but lower pressure work per cycle owing to increased leaks. High compression yields 1.3J/cycle (39W @30Hz), while low compression yields 1.4J/cycle (42W @30Hz).

Optimal performance can be obtained by using a controller that maximizes thermodynamic efficiency and minimizes the electrical losses in the coil. However, the present work focuses on primarily on the mechanical power where compared to the conventional (i.e., uncontrolled)

cycle, the mechanical power of the controlled cycle can altered and therefore increased by varying the compression and expansion rates, the scavenging time, and the compression ratio.

4.3.2 The programmable cycle concept

The primary focus of the present experiments is to investigate the effects of closed-loop feedback control of the piston motion on the thermodynamic cycle and hence on the power output. To this end, the piston speed (and therefore its trajectory) is controlled during the compression and expansion processes and during scavenging (at BDC). The concept is shown schematically in Figure II.3. As illustrated in this figure, it is possible to achieve longer scavenging period by lowering the compression ratio and having faster expansion at the same operating frequency. As will be shown below, this cycle configuration yields higher power output (it is also noteworthy that a programmable cycle may be used to reduce or eliminate potential overshoot of the piston motion at BDC which reduces friction losses).

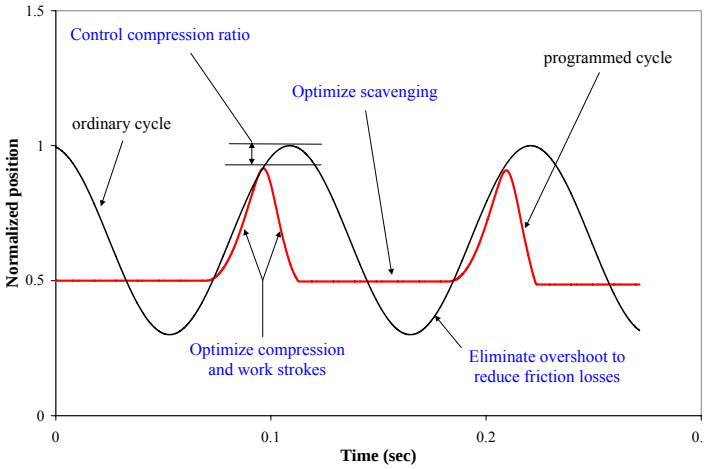

Figure 4.3-5 *Programmable stroke dynamics and scavenging.*

To demonstrate the performance of a QNX-based controller, consider an example which compares the desired and measured time-dependent piston positions in a controlled cycle experiment (Figure 4.3-6). In this cycle, the piston is driven by the voice coil during compression ("A") and combustion takes place at TDC. Following combustion, the load on the piston is simulated by forcing it to remain briefly near TDC ("C") and during the following trajectory "B" until piston reaches BDC. At that point, the simulated reaction force is removed but the residual combustion pressure forces the piston to overshoot and continue to move for a short period of time beyond BDC along "D". Of course, this overshoot can be reduced by modifying the controller code. Finally, the piston may be held briefly at BDC ("E") to achieve optimal scavenging (which is not possible in traditional two-stroke engines).

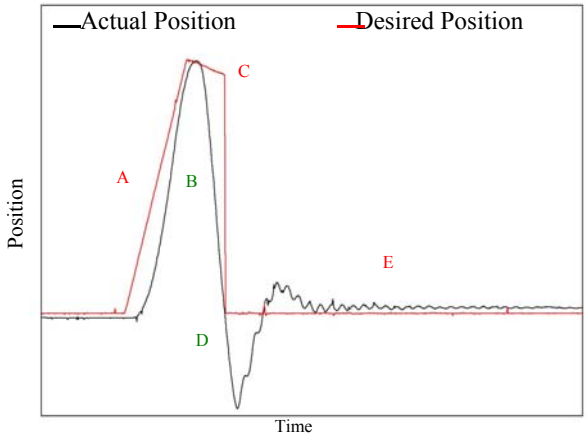

Figure 4.3-6 *Time-history of the desired and actual piston position in a controlled cycle*

4.3.3 Programmable compression ratio

The variation of cavity pressure with piston position for two different compression ratios is illustrated in Figure 4.3-7 which effectively the p-v diagrams for these cycles (isentropic compression is shown for comparison using a solid curve). In this example, the maximum normalized cycle pressures (relative to p_{atm}) are nominally 14 and 12. Perhaps the most striking feature of these cycles is that while the higher compression ratio yields a higher peak pressure, the energy per cycle (1.8 J) is actually *lower* than what is achieved at the lower pressure ratio (2.1 J). The reason for that is that just as in any practical implementation of such power generators it is expected to have a certain level of leakage around the piston (particularly with extended operation that results in wear owing to environmental effects such as dust and

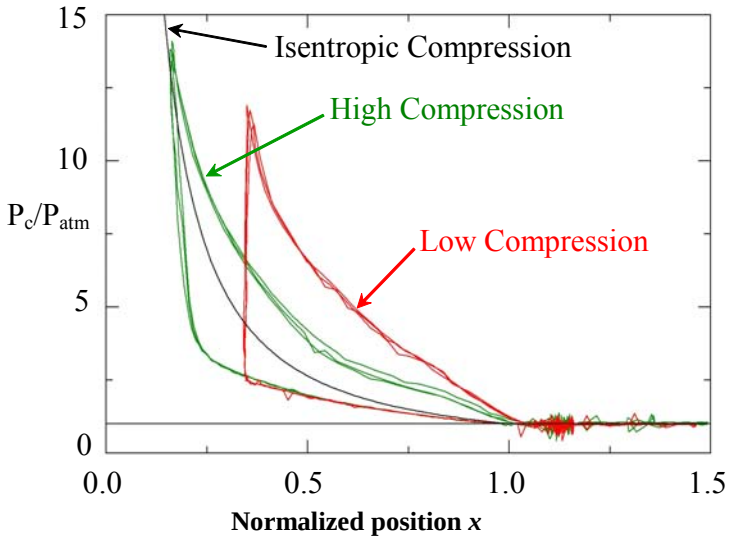

Figure 4.3-7 *Programmable compression ratio: energy per cycle at high and low compression (piston position is normalized relative to the exhaust port).*

therefore these leaks become more serious at higher combustion pressure. The programmable cycle affords the opportunity to tune the generator to higher power output by altering the

compression ratio during operation. It is noteworthy that the shaft work at the high and low compression ratios is 1.3J/cycle and 1.4J/cycle, respectively. These levels of shaft work would correspond to 39W and 42W at a nominal operating frequency of 30Hz.

4.3.4 Programmable scavenging

An important feature of the programmable cycle approach is that it enables alteration of the duration of scavenging at BDC. To demonstrate the effect of the scavenging time, the operating frequency of the piston is altered between a "fast" cycle (having a period of 50 msec) and a "slow" cycle (having a period of 1 sec. The resulting p-v diagram is shown in Figure 4.3-8. These data show that when scavenging is improved the peak pressure during the cycle increases substantially as does the energy output per cycle (1.1 J and 1.3J at 50 msec and 1 sec cycle periods, respectively). Again, this approach may be very useful when the performance of the generator degrades or is altered during its lifetime. The effect of the scavenging time on the shaft work is remarkable: the "fast" cycle (0.6 J/cycle) corresponds to 18W at 30 Hz while the "slow" cycle (1.3 J/cycle) corresponds to 39W at 30Hz.

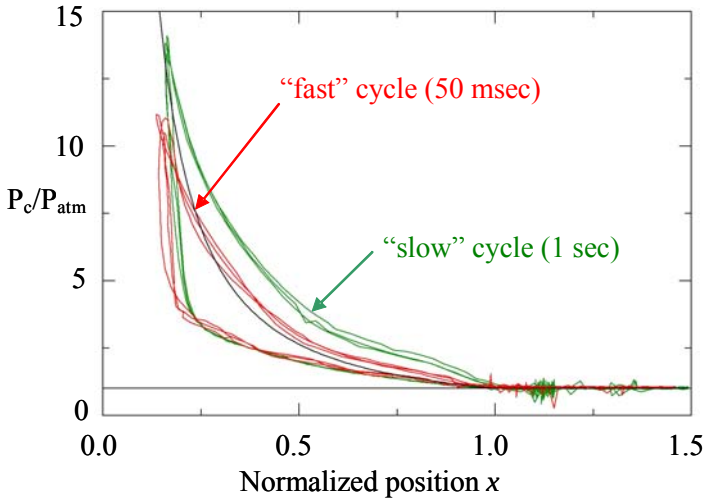

Figure 4.3-8 *Programmable scavenging effects.*

The programmable cycle was used to provide specific scavenging delays in piston motion at BDC (Figure 4.3-9a and b). These data compare delays of 30 and 70 msec (for the same stroke) and show that the increase in the delay corresponds to higher cycle pressure and higher output power. Figure 4.3-9b is the time history of the energy output and shows an improvement by factor of 2 in shaft work per cycle.

While these data show that it is possible to increase the mechanical power using the programmable cycle approach, in practice it is desirable to optimize electrical power generation. This is investigated using numerical simulations and will be reported in the next reporting period.

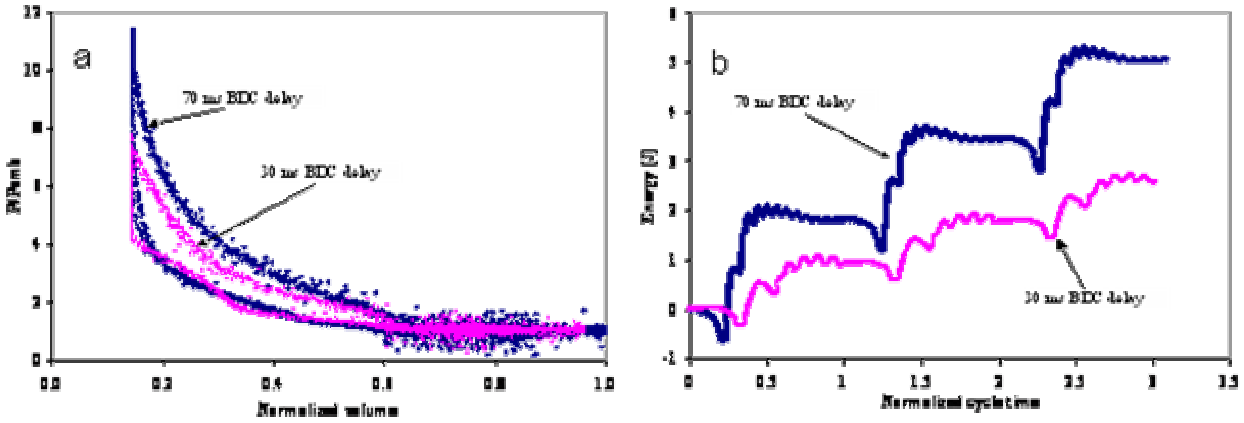

Figure 4.3-9 *(a) p-v diagram for programmable scavenging and (b) Time history of energy production.*

4.3.5. Numerical Simulations

The dynamics of the power generator was simulated to deduce useful information about the coupling between the electric and mechanical segments of the system. The simulation takes into account thermodynamic cycle, heat transfer through the walls, and scavenging process (which is modeled as well-stirred reactor model with compressible flow through the exhaust ports. In this context the combustion process was treated as nominally "steady" and leaks about the free piston were modeled using simple Couette flow with pressure gradient. The piston is coupled to a voice coil generator which was modeled separately to allow for its optimization. In these simulations, the pressure, temperature, density, position, velocity, acceleration and force were calculated using the conservation equations for a deformable control volume. The simulation assumes that the piston motion is driven by a constant force which is provided by a voice coil actuator.

Three cases were simulated: I. Optimal compression speed (max compression velocity 2 m/s and compression ratio of 2.2) for which the thermodynamic power is 27.9 W, the shaft Power is 21.5 W, the operating frequency 20.6 Hz, and the maximum pressure is 7.08 bar; II. Optimal compression speed (max compression Velocity 2 m/s, and compression ratio of 3) for which the thermodynamic power is 22.3 W, the shaft power is 16.2 W, the operating frequency is 19.4 Hz, and the maximum pressure is 6.00 bar; III. Fast compression (max compression velocity is 2.7 m/s and the compression ratio is 2.2) for which the thermodynamic power is 13.5W, shaft Power

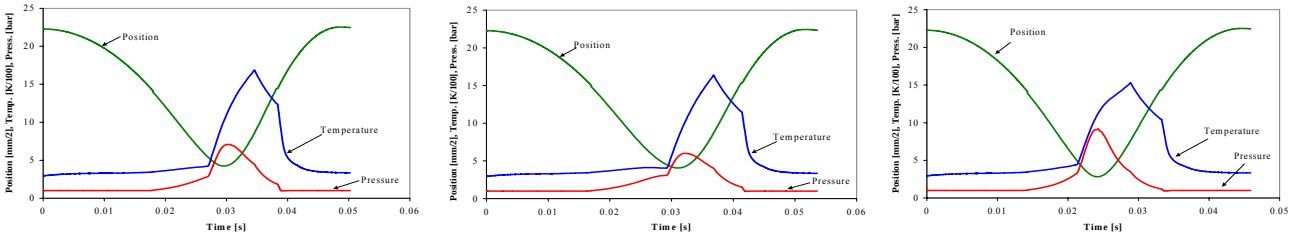

Figure 4.3-10 *Variation of pressure, temperature, and piston position during the cycle for Cases I (left), II (center) and III (right).*

is 6.2W, the operating frequency is 22.4 Hz, and the maximum pressure is 9.08 bar.

The data in Figure 4.3-10 show that the rate of expansion (as may be judged by the variation of piston position with time) is largest for Case I. This is, of course, desirable in order to reduce leakage of combustion products from combustion chamber just after the combustion when potential for leak is the highest due to the high pressure. Therefore, the cycle in which leakage following the combustion is minimal is more efficient. Furthermore, faster expansion is typically associated with larger power production. In Case III, the rate of expansion is about the same as that of the compression which is undesirable and consequently the power is the lowest.

The corresponding p-v diagrams (Figure 4.3-11) show that the maximum power is obtained for Case I. In fact, even though the frequency for Case III is the highest, the power is still smallest due to a large leak at top dead center (TDC) which is associated with the sharp edge of the curve at the peak pressure. The leak that is associated with loss of power performance is related to the time that is needed to slow down the piston and reverse its direction near TDC. It is also interesting to note that that the lowest power is produced by the cycle that has the highest peak pressure. This peak is associated with the lowest combustion volume as a result of the high piston speed at TDC. This issue must be taken into account when designing and optimizing the controlled cycle engine because the price for fast compression is increased leak at TDC. On the other hand if the compression is slow, the cumulative leak can still be significant even before combustion so that lower chemical potential and pre-ignition pressure are available at the beginning of combustion. This is the reason why it is desirable to operate the engine why with optimal compression speed.

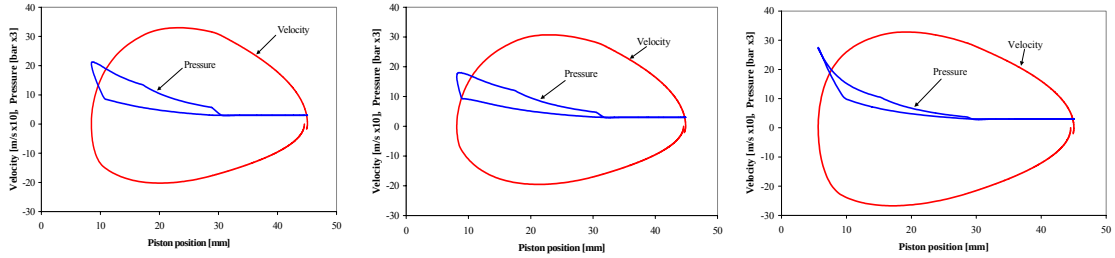

Figure 6 *Pressure and velocity for Cases I (left), II (center), and III (right).*

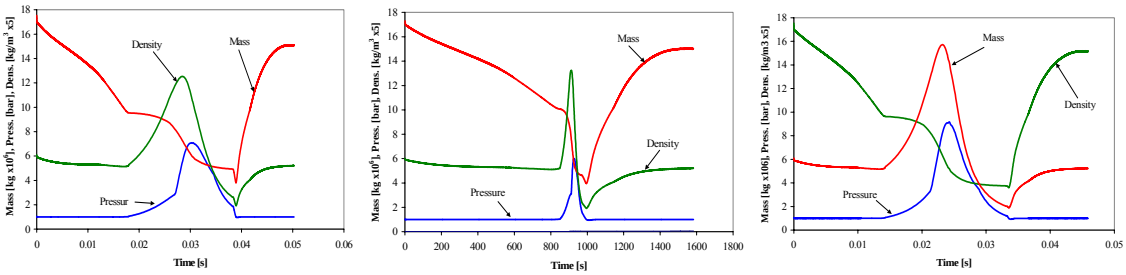

Figure 4.3-11 *Variation of mass, density, and pressure for Cases I (left), II (center), and III (right).*

Next, consider the variations of power performance with compression ratio. While for better thermodynamic efficiency it is clearly desirable to have higher compression, as noted above, this does not take leakage into consideration and therefore the question is what is the optimal compression for a given leakage. For example, Case II above (Figure 4), has optimal compression speed but a compression ratio that is higher then optimal and therefore the leakage

nullifies the compression. Therefore the loss of unburned fuel results in poorer power performance compared to Case I. At the same time, the variation in the temperate profile is consistent with the pressure variation, smaller leaks result in an increase in the available chemical potential and in the peak temperature of the combustion flame which yields stronger combustion and higher power. This is the reason for the highest temperature in Case I.

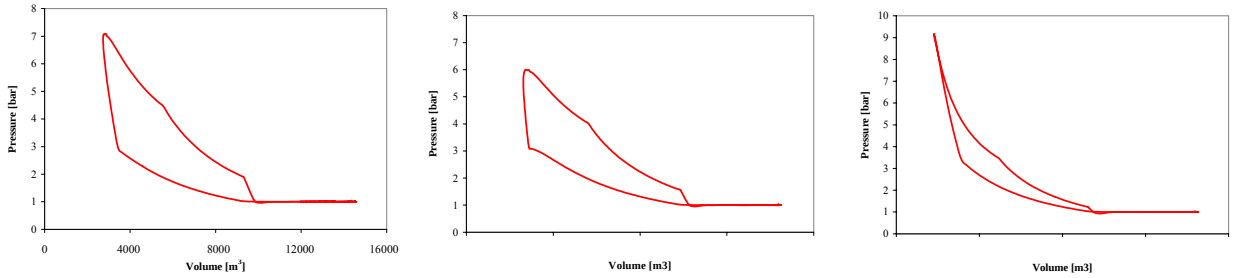

Figure 4.3-12 *p-v diagrams for Cases I (left), II (center), and III (right)*

As alluded above, the faster the expansion the better the power performance. The variation of the mass within the control volume shows which part of the cycle has the largest leak and consequently poorer power performance. Again, these data show that Case I has indeed the lowest leak owing to the fast change of direction at TDC and sub-optimal pre-ignition pressure.

The last set of figures shows the variation of the shaft work during the cycle for Cases I and III (Figure 4.3-13). For Case I, the shaft work per cycle is about three times the work in case III indicating that in Case III the engine has to operate at three times the frequency to deliver the same power. However, as the frequency is increased, the energy per cycle decreases and therefore the frequency needs to increase further to obtain the same power output.

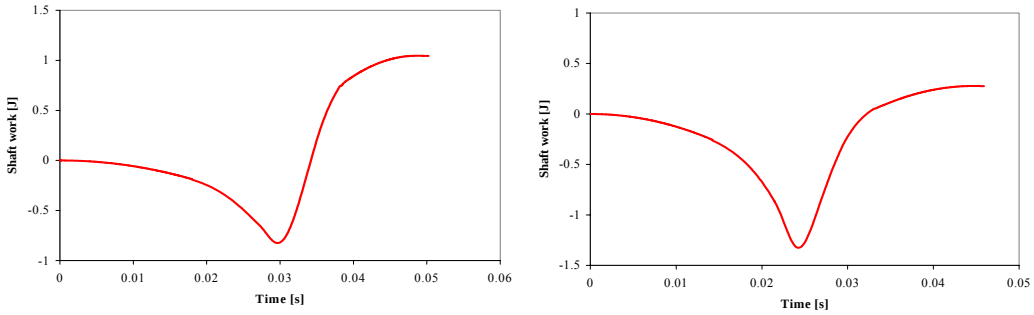

Figure 4.3-13 *Shaft work history over cycle cycle, Cases I (left) and III (right)*

The power output can be optimized with respect to the compression ratio. As noted above, high compression ratio is not necessarily better for flat piston engines due to challenging seal of the piston. This is shown in Figure 4.3-14 where the compression ratio was varied and shows a clear optimum for the shaft power. The maximum shaft power for the present configuration occurs at compression ratio of 1.53, which is the optimal compression ratio.

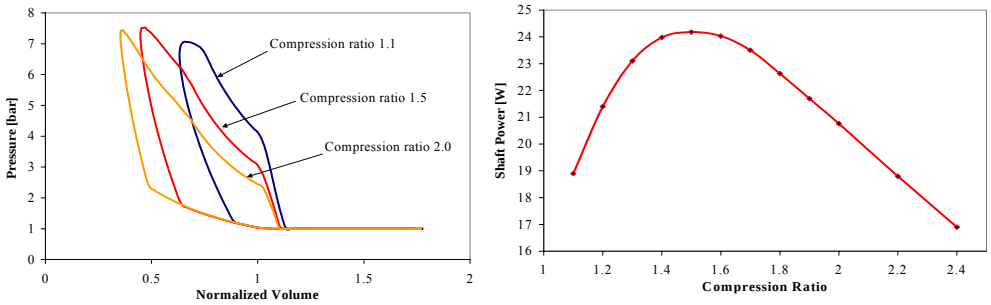

Figure 4.3-14 *Variation of shaft power with compression ratio*

Next, the effect of the compression speed (or compression rate) on the shaft power is considered (Figure 4.3-15). It would have been expected that better performance would be attained at higher compression rates due by shortening the cycle period because of the concurrent minimization of heat losses. However, again, it becomes clear that leakage is more dominant and both experiments and simulations show that shaft power attains a peak at an intermediate speed at TDC when the optimal velocity is 2 m/s.

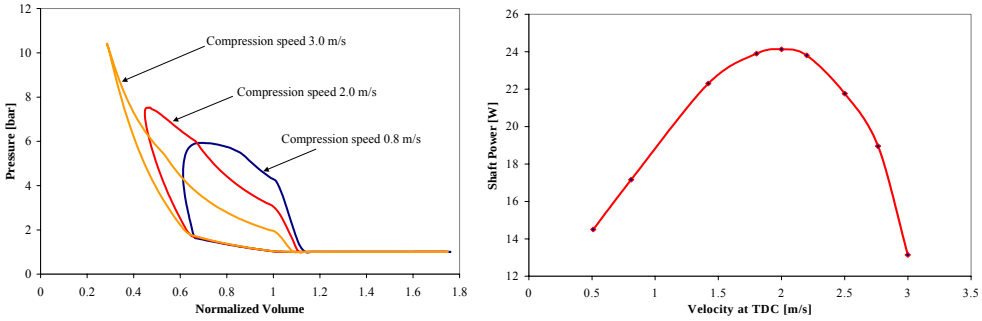

Figure 4.3-15 *The effect of compression rate shaft power.*

Finally, the effect of scavenging delay at Bottom Dead Center (BDC) is considered (Figure 4.3-16). These data demonstrate the importance of the scavenging process in two-stroke engines. Because the present engine is a linear free piston engine, it is possible to vary the performance substantially simply by varying the scavenging time. Of course, it is necessary to take into account the power output since energy per cycle can be larger with longer delays at BDC due to better scavenging. Figure 4.3-16 shows some of the features that are associated with the variation of the scavenging time. A delay of 70 ms BDC results in a substantial change in the p-v diagram (faster rise in pressure, shorter time and distance for the change in piston direction and faster combustion rate). The plot on the right shows the variation in shaft power, shaft energy per cycle, and frequency. As shown, for the present configuration there is a local maximum in power which is obtained with a delay of 30 ms at BDC. While the increase in power at small delays is relatively strong, the diminution at larger delays is far more gradual.

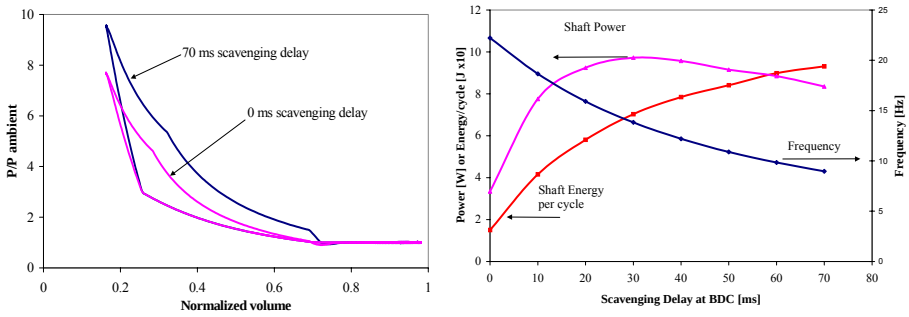

Figure 4.3-16 *Variations of shaft power, shaft energy per cycle, and of frequency with scavenging delay.*